Université de Nice Sophia Antipolis - Faculté des Sciences
Institut Non Linéaire de Nice
Ecole Doctorale des Sciences Fondamentales et Appliquées

THÈSE

présentée pour obtenir le titre de

Docteur en Sciences de l'Université de Nice Sophia Antipolis
Spécialité : Physique

par

Francesco Pedaci

Control of Cavity Solitons and modal dynamics in semiconductor lasers: experimental investigation

Contrôle des Solitons de Cavité et dynamique modale dans les lasers à semiconducteur: étude expérimentale

Dirigée par Jorge R. TREDICCE et Massimo GIUDICI
et soutenue le 20 Novembre 2006 à 14h30

Jury

M. Jorge R. Tredicce	Directeur de Thèse
M. Massimo Giudici	co-Directeur de Thèse
M. Luigi Lugiato	Président du Jury
M.me Carmen Menoni	Rapporteur
M. Pierre Glorieux	Rapporteur
M. Robert Kuszelewicz	Examinateur

à l'Institut Non Linéaire de Nice

Resumé

Le travail présenté dans cette thèse consiste de l'étude expérimentale de deux systèmes de lasers à semiconducteurs.

Dans la première partie, nous étudions la dynamique modale des lasers à émission latérale, dits bulk. L'émission de ces lasers présente en général un seul mode de cavité interne. Dans certaines régions des paramètres, toutefois, on observe bistabilité et "mode-hopping" induit par le bruit entre deux modes de cavité principaux. Nous analysons expérimentalement cette dynamique modale qui peut être décrite en une dimension en termes d'un (quasi-)potentiel bistable et bruit, par une équation de Langevin. On observe que une modulation symétrique du courant de pompage du laser modifie la symétrie d'émission entre les deux modes. Une hypothèse dynamique est donc formulée, faisant intervenir, dans l'équation décrivant le comportement temporel modal, les fluctuations du courant comme un terme de bruit multiplicatif. Dans un tel système il est possible observer le phénomène de résonance stochastique. Enfin, a partir des équations d'évolution des variables du laser, en considérant les échelles temporelles relatives, il a été possible dériver une équation de Langevin mono dimensionnelle, avec bruit multiplicative, qui bien reproduit la caractérisation expérimentale.

La deuxième partie est consacrée au contrôle expérimental des "solitons de cavité". Dans ce travail, ces structures localisées non linéaires sont crées dans le plan transverse des lasers à cavité verticale (VCSELs) avec injection externe. Nous étudions leur déplacement sous l'influence de forces externes, montrons les effets des gradients de phase et intensité dans le champs d'injection et démontrons la possibilité de construire un registre à décalage optique en utilisant leurs propriétés. Enfin, en utilisant une masque de phase reconfigurable pour l'injection, on montre que, grâce leur plasticité, les solitons peuvent être fixés dans des différentes configurations dans le plan transverse, comme prévu par les résultats théoriques. Ces résultats sont encourageants en vue de possibles applications où le solitons de cavité peuvent constituer les bits (1-0) d'un dispositif de stockage et/ou routage optique reconfigurable.

Acknowledgments

It's a pleasure to finally write my own acknowledgment page. There are many persons that deserve a place in this page. I start from people I worked with, and I have learnt so much from, about physics but not only. Our equipe is a very interesting dynamical entity, and the flow of individuals that cross it in time has an unforgettable experience, always extremely positive.
This is mainly because of Jorge Tredicce, my advisor. He gives the direction, the course of the mothership which is incredibly always correct, far-seeing and pleasurable. Wisely, he indicates the way and when a problem comes, his optimism is the real solution, he is our compass in the storm!
Then Massimo Giudici, my second advisor, who helped me really a lot. He taught me tons of practical solutions in the lab, starting from the very beginning, when I did not know almost anything about experimental physics. Discussions with him are always fruitful, with his very old notebooks from our university! He deserves a big place in this page. Thank you very much.
So, what can I say about dr.Stephane Barland? I think an entire book would not be enough. Since he arrived, everything changed. A sort of revolution: I mean, I'm writing now on a small ugly black terminal, with VIM, and I'm happy, isn't it a big revolution? I owe it, as many many other things, to Stephane, I don't want to make a list here, but I know he knows. If discussions with Massimo and Jorge are always pleasant and peaceful, trying to convince Stephane is always a very hard challenge, especially because, unfortunately for me, he is very often right. His sincerity and outspokenness, in life as in science, is one of his qualities that we all should have more (even if World War III will start immediately after.$_{741242:)}$)
Then I thank Xavier Hachair, from whom I inherited the perfectly working Solitons experiment, and Luca Furfaro who always was there to help. They have directly given strong contributions to the work presented here (also for la méthode qu'est ce qu'on fait on essay?).
I thank Salvador Balle for everything, because a big part of this work is due to him. And Stefano Lepri for the help he gave me during the very good collaboration on bulks. Then Gianni Giacomelli (echee', miha mi dimentico!) deserves a big place here, for physics surely, but also for all he made me eat there in Florence! (lo Spera, la trattoria sui colli, la degustazione d'olio extra vergine, la pappa al pomodoro, meglio se smetto..)
I thank Gabriel Mindlin, who helped me a lot, also giving the right suggestion for the work on bulk, and I hope to meet him again.
Then I give thanks to Gattobigio brothers Gianluca e Mario (goodbye to Italy? il negozio di bici?), Frédéric Hebert, Stefania Residori, René Rojas, Gianluca Lippi,

Julien Javaloyes, Lionel Gil, David Wilkowski, Valentin Krinski and surely Giovanna Tissoni for their help, and to Emilie Caboche et Patrice Genevet (merci de tout et tres bonne continuation) who have contributed importantly to the work on solitons.
I thank all the group working in Bruxelles, Jan Danckaert, Guy Van Der Sande, Miguel Soriano and Guy Verschaffelt for their invitation and discussions.
A special muchas gracias to Alejandro Yacomotti and Victor Planas, things have changed but for me everything started with you, and I hope it will continue!
I thank a lot all the nice people working at ERC of Colorado State University, Jorge Rocca, Carmen Menoni, Brad Luther, Jorgito Filevich, Betty Shoemaker, Mario Marconi, Yong Wang, Ovidio and Laura, for my extremely nice stay there few years ago, and for the future one...!
I am grateful to Carmen Menoni, Pierre Glorieux, Luigi Lugiato and Robert Kuszelewicz to have accepted to be part of the jury for this thesis.
The strong support of my family made everything much easier, and I am happy to share with them this moment. And finally I thank you, Barbara, while you're reading your book, practicing in English (as I would need..) on the sofa, thinking how crazy I'm, typing strange things until 23.56 at night. This work is dedicated to you.

Typeset with LaTeX
on DEBIAN stable

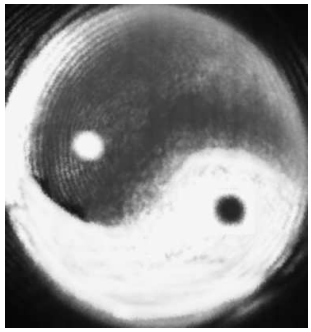

Contents

I. Introduction

I.1. Origins of Laser

Tracing back to the origins of the laser history, one inevitably arrives to the beginning of the twentieth century when quantum mechanics was changing the perspectives of older physics and in general the look of the modern society to the microscopic world. Einstein was one of the most important actors at that time. In 1905 his work on the photoelectric effect overcame the problems of the classical theory on the interaction light-matter, introducing the fundamental hypothesis that was the base of the modern physics, the quantization of the electromagnetic field. In 1916 he proposed a more detailed understanding of how photons interact with atoms and their electronic energy levels [1]. The three fundamental mechanisms of interaction were described: spontaneous emission, stimulated emission and absorption. The energy difference between two atomic levels was assumed to be discrete so an atom can absorb a photon only if its energy gap results equal to the energy $h\nu$ of the photon. An atom can also emit a photon with energy equal to the energy gap, falling from its excited state to the lower one. This can occur spontaneously (so the rate of the emission would depend on the upper level lifetime), or stimulated by another photon which will generate an identical photon (both will have the same momentum vector and phase).

The work of Einstein was almost forgot until after World War II, when the interest of researchers focused again on stimulated emission. This is the working mechanism at the base of modern laser devices. A clear experimental observation of such interaction between light and atoms was a hard task up to 1958. In fact in order to have a measurable stimulated event, one has to find the way to keep many atoms in the medium in their excited state. Then in principle using just one photon like a seed would produce a cascade of coherent light coming from stimulated emission. As all natural systems and materials tend to populate their ground state at expense of higher energy levels because of thermalization, an external mechanism should be able to achieve the so called *population inversion*. From the theory developed by Einstein it results that the net power generated by the atoms interacting with the radiation is

$$P = (N_2 - N_1)\frac{A_{21}h\nu}{e^{h\nu/K_BT} - 1} \tag{I.1}$$

where A_{21} is the rate of spontaneous emission, N_1 (N_2) the population of the lower (upper) state of the atom and T the temperature. Not surprisingly the output power is proportional to the difference in the population of the two levels ($N_2 - N_1$). Stimulated emitted light can grow up inside the material only if $N_2 > N_1$.

In 1953, Charles H. Townes and graduate students James P. Gordon and Herbert J. Zeiger produced the first maser, a device operating on similar principles to the laser, but producing microwave rather than optical radiation. This early system, whose development was connected with military researches for radar systems, could amplify a 24 GHz radiation in a resonant cavity filled with ammonia but was incapable of continuous output [2]. Nikolay Basov and Aleksandr Prokhorov in the Soviet Union worked independently on the quantum oscillator and solved the problem of continuous output by using more than two energy levels. This system could release stimulated emission without falling to the ground state, thus maintaining a population inversion. Townes, Basov and Prokhorov shared the Nobel Prize in Physics in 1964 "for fundamental work in the field of quantum electronics, which has led to the construction of oscillators and amplifiers based on the maser-laser principle".

The way to optical frequencies was paved, and the first (pulsed) LASER (Light Amplification by Stimulated Emission of Radiation) was made by Theodore H. Maiman in 1960 [3] at Hughes Research Laboratories in Malibu, California, beating several research teams including those of Townes at Columbia University, and Arthur L. Schawlow at Bell Labs. Maiman used a solid-state flashlamp-pumped synthetic ruby crystal to produce red laser light at 694 nanometers wavelength. Maiman's laser, however, was only capable of pulsed operation. Later in the same year the Iranian physicist Ali Javan, together with William Bennet and Donald Herriot [4], made the first gas laser using helium and neon. This type of laser (He-Ne) had been the dominant laser for the next 20 years until cheap semiconductors have appeared.

However excitement about lasers began to fade, they were called "solution looking for a problem". But as it often happens the military interests helped in progress of science development. For Vietnam war the laser-based radar, targeting, and reconnaissance system was created [5]. Environmental and later energy concerns led to increased funding for laser research investigating fields such as air-pollution monitoring and energy applications. The other important reason for researching of laser technology was its attractiveness for use in communication since the amount of coherent information that an electromagnetic wave can carry is proportional to its frequency, and optical light has frequencies much higher than radio and microwaves.

I.2. Semiconductor lasers

I.2.1. Principles of operation

The possibility of using semiconductors in order to achieve stimulated emission was first considered by Von Neumann in 1953[1] [10]. Then the transition between conduction and valence bands in semiconductors was considered by Bernard and Douraffourg [11] in 1961. In the Soviet Union, N. Basov and D. N. Nasledov were also considering how to achieve population inversion in a semiconductor [12].

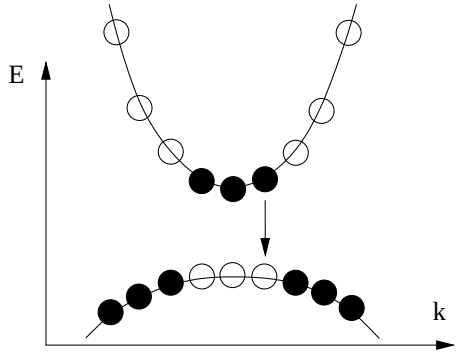

Figure I.1.: Schematic representation of the band structure of a direct semiconductor laser at room temperature. Filled (empty) circles correspond to electrons (holes). An electron recombining with a hole can give rise to a photon.

The knowledge developed for atomic lasers had to be translated to semiconductors. These are too different from atoms and a simple description in terms of two energy levels could not be possible. Unlike the atom, the energy states of the electrons in semiconductors occur as energy bands instead of discrete levels. These bands arise due to the ordered structure of atoms in the atomic lattice of the semiconductor crystal. The bands of interest are the valence and conduction bands, and the forbidden energy interval between them is referred as energy gap. They can be modeled with parabolic shape as a function of the momentum k of the electron and in direct semiconductors the maximum of the valence band corresponds to the minimum of the conduction band, as in fig.I.1. The description of the electronic state is given by the Fermi-Dirac distribution. In thermal equilibrium at $0\,^oK$, all the allowed energies below the so called Fermi energy E_f are occupied and above it they are empty. For higher temperatures this distribution is smoother and some states above E_f are occupied and some states under E_f are empty. In pure semiconductors E_f is close to the center of the bandgap, therefore at $0\,^oK$ the conduction band is empty and the valence

[1]For a review of the history of semiconductor lasers see also [6][7][8][9]

band is completely filled. Anyway the bandgap (of the order of 1 eV) allows at room temperatures the passage of electrons to the conduction band and holes to the valence band (holes are vacancies of electrons, and are treated as quasi-particles).

The idea at the base of semiconductor lasers is then to use the recombination of electrons falling from the conduction to the valence band (electron-hole recombination, which has characteristic time of 10^{-9} s) as it was for the two energy levels in atoms, in order to produce a photon. Here the difference with a simple two levels medium comes from the dependency of the transition energy over the momentum of the electron. So in first approximation the laser has an inhomogeneous gain profile, as a gas laser where Doppler effect is taken into account for the medium. Not every electron-hole recombination gives rise to a photon (phonons can also be produced, giving an increase of the temperature), but the quantum efficiency of semiconductor lasers can be incredibly high (>90%).

The main ingredients that were proposed (and are now basilar for semiconductor lasers) are the use of a *p-n* junction and the need for a flow of electric current across it. A *p-n* junction is a structure made by two semiconductors placed in contact. One of them is treated (*n-doped*) in order to enlarge the number of electrons in the conduction band, the other is *p-doped* to present more holes in the valence band. This is done by inserting some impurities in the crystal (electronic donors for the $n-$type, acceptors for the $p-$type). This changes the electronic distribution, and the level E_f changes accordingly (closer to the conduction band in the $n-$type, closer to the valence band for the $p-$type).

When the two n and p semiconductors are put together in order to create the $p-n$ junction, the thermal equilibrium is achieved bending considerably the energy bands as in fig.I.2 (a). At equilibrium the Fermi energy level is the same over the entire junction, and no motion of electrons or holes is possible along the junction because of the potential barriers created. If a positive voltage is applied and the junction is forward biased, as in fig.I.2 (b) the material is no longer in thermal equilibrium. However it can be assumed in a good approximation that electrons and holes are in thermal equilibrium inside their conduction and valence band respectively. This is due to the fact that the thermalization time of electrons and holes is extremely short (10^{-13} s). As long as this quasi-equilibrium condition is satisfied, electrons and holes with different momentum are all coupled and the laser saturates homogeneously, in spite of the inhomogeneous gain profile. This feature makes the semiconductor laser be at the border between the two classes of homogeneous and inhomogeneous lasers [14].

The Fermi level then splits, for a biased device, into two quasi-levels, corresponding to the distribution of electrons in the conduction band (F_c) and holes in the valence

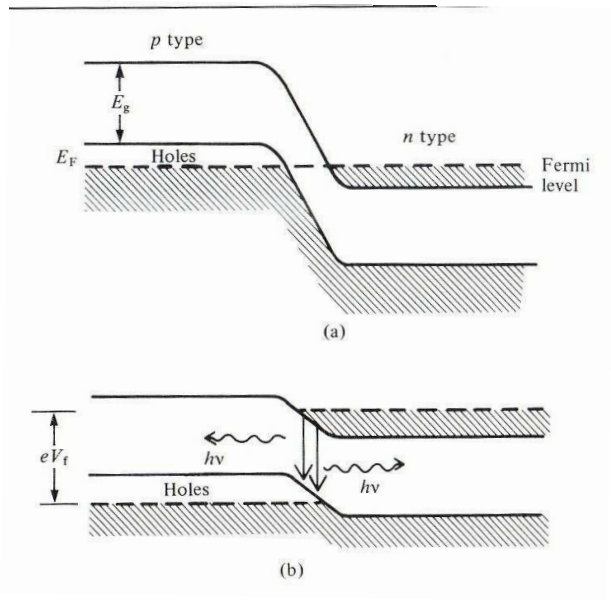

Figure I.2.: Band edge structure for a $p-n$ junction in absence (a) and in presence (b) of the external voltage [13].

band (F_v). In a biased junction then the amount of electrons and holes in the depletion region is greatly increased creating a small region of population inversion, where radiative recombination can occur.

I.2.2. Edge emitting lasers

The first experimental studies date to 1962, when the group of G. Fenner in New York operated the first semiconductor diode laser (September 16, Sunday![15]). Within less than one month three other groups succeeded in laser operation in semiconductor devices. The first semiconductor laser with visible emission was demonstrated later the same year by N.Holonyak [7]. As with the first gas lasers, these early semiconductor lasers could be used only in pulsed operation, and only when cooled to liquid nitrogen temperatures (77 K). They were pumped with high current pulses lasting only few microseconds. The efficiency of these first *homojunctions* was not able to carry the lasers to the interest of industry, as it happened after the creation of the first *heterojunctions*. In these lasers (called bulk edge emitters) the light propagates then in the plane of the junction, across a rectangular waveguide. The mirrors of the cavity are formed by cleaving the semiconductor wafer and polishing the facets. Then the reflectivity is due to the change in index from the material to the air, and is of the order of 30%.

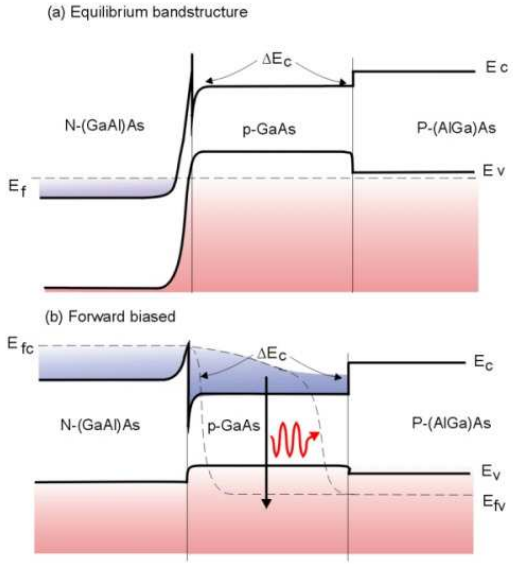

Figure I.3.: Energy band structure for a double heterostructure in absence (a) and in presence (b) of the applied voltage.

In 1963 H. Kroemer [16], and independently in URSS Z. Alferov, suggested (and in 2000 they received the Nobel prize for their idea) to sandwich a semiconductor with the desired band gap between materials with larger band gaps. This is called a double heterostructure and it is shown in fig.I.3. In this way a more effective confinement of carriers is possible, increasing the carrier density and lowering the threshold current. The emitted photons are then also confined in the active central region which has lower band gap and higher index of refraction. The junction acts at the same time as a waveguide for the photons and a potential well for the inverted carriers, so stimulated emission is greatly increased. In this way the first semiconductor laser with low threshold could appear in 1969 [17], and this was the beginning for their widespread use that contributes to development in many fields nowadays. From bar code readers (since early '80), to fast telecommunications (so Internet) or CDs readers and writers, semiconductor lasers have slowly but effectively entered in everyday life of many millions of people.

Many improvement have been done in bulk edge emitting lasers since the first realizations. Additional confinement mechanisms are present nowadays in order to increase the carrier density in the active area. The early gain guided lasers (i.e. where the confinement of carriers in the plane of the junction is determined simply by the current profile) have been substituted by more complex index guided laser, where a suitable lateral guiding profile is tailored inside the active region. Then quantum

well and multi-quantum well lasers appeared, where the thickness of the active region (the quantum well) reaches and become smaller than the emitted wavelength. These are the devices most used today, and it becomes difficult to find in the market old structures like bulk edge emitters.

I.2.3. Vertical Cavity Surface Emitting Lasers (VCSELs)

Edge emitting lasers have some property that can become a problem for specific applications. The length of the cavity of the order of hundreds of microns allows in general for longitudinal multi-mode operation. In fact the typical distance between two adjacent longitudinal modes is in these cavities of the order of hundreds of GHz, while the width of the gain curve is of the order of thousands of GHz. Then tens of modes can experience very similar gain and due to non linear coupling, multi-mode operation or instabilities are often found in experiments. Another problem making difficult the coupling with fibers for example, arises from the strong elliptical profile of the emitted beam, due to the difference between the two transverse confinements (i.e. diffraction) of the optical mode propagating in the plane of the active region. Finally because cleaving is a step of the fabrication, they cannot be tested before having been packaged.

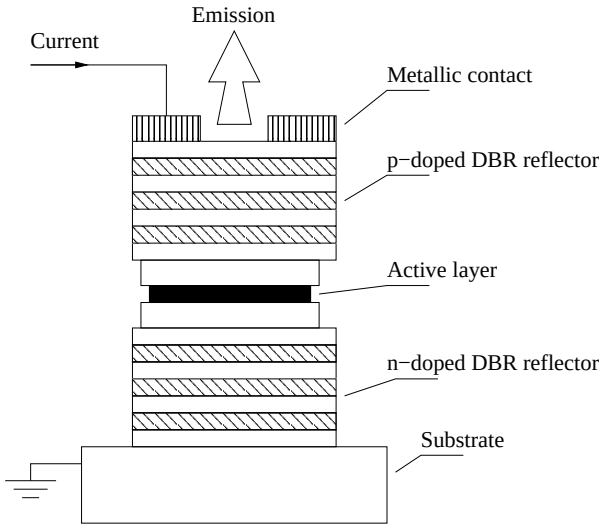

Figure I.4.: Schematic structure of a VCSEL.

VCSELs give a solution to these problems. They are semiconductor lasers with the cavity oriented perpendicular to the active layer, as in fig.I.4. So, the beam is emitted and guided vertically. The cavity (tens of microns) is much smaller than the

one of bulk lasers, and its free spectral range is larger than the gain curve width, so just one longitudinal mode is intrinsically possible. The very thin active layer (sub-wavelength single or multiple quantum well) gives low value of the single passage gain, so a very good cavity is necessary. The mirrors then cannot be formed by just the interface between material and air (this gives 30% of reflectivity), so the interferometric structure of distributed Bragg reflectors is used and reflectivities of the order of 99.9% are achieved. The placement of the thin active layer along the cavity is an important parameter, and it is placed usually on one antinode of the standing wave created into the cavity in order to increase the gain.

Once the wafer is grown, a circular ring electric contact is placed at the top of the cavity, in order to inject the bias current. In some cases a circular dielectric ring is placed into the cavity to better confine the current and light. In this way many lasers can be found over the matrix and tested independently. The result is a perfect circular emitted beam, with high degree of coherence and low values for the threshold current. The problem related to the cylindrical aperture of these kinds of lasers is that no mechanism for fixing the polarization exists (while for edge emitters the polarization is fixed by the active layer), so polarization instabilities occur above threshold between the two possible orthogonal states imposed by the crystal. Other geometries are possible, as for bottom emitting VCSELs, where the emission of light is done trough the substrate layer.

I.3. Dynamical classification of lasers

The usual approach to model the interaction between material and optical field in a laser is based on the so called semi-classical approximation. It consists in the quantum-mechanical description of the gain medium, while the field is treated classically. This approximation is valid for all the experiments where an high number of photons is involved, as in our case.

The *Maxwell-Bloch* equations describe the interaction of a set of homogeneously broadened two-level atoms with a single mode field in the slowly varying amplitude approximation. The dynamics of the relevant variables is then driven by the following coupled differential equations

$$\dot{E} = -i\omega_c E - gP - kE \tag{I.2}$$

$$\dot{P} = -i\omega_a P - gEN - \gamma_\perp P \tag{I.3}$$

$$\dot{N} = -2g(EP^* - E^*P) - \gamma_\parallel (N - N_o) \tag{I.4}$$

where E is the complex field amplitude, P the complex polarization, N the population inversion, and k, $\gamma_\perp$ and $\gamma_\parallel$ are the respective loss rates. N_o is the population inversion which would be established in absence of coupling, g is the coupling constant in terms of the transition dipole moment, while ω_a and ω_c are the atomic and cavity frequencies respectively[18][19].

In order to limit the number of dynamical variables, it is common to limit the description to single-mode lasers in homogeneously broadened media, so that the entire dynamics is characterized by the three variable: field amplitude, polarization and population inversion. In this case, depending on the relative decay rates k, $\gamma_\perp$ and $\gamma_\parallel$, an useful dynamical classification of lasers has been introduced in [20][21].

For *class A lasers* (mainly dye lasers) both the polarization and the population inversion decay on much shorter time scales than the electric field ($\gamma_\perp \simeq \gamma_\parallel \gg k$). In this case it is possible to adiabatically eliminate the dynamics of P and N, as they immediately follow the slow variations of the field. The system dimension is then reduced to one, with just one differential equation for E, and a fixed point is rapidly reached.

In *class B lasers* (for example solid-state lasers as Ruby, Nd:Yag, Ti:sapphire, CO_2 and semiconductor lasers) only the polarization decays on fast time scales, while the decay rates of field and population inversion are comparable ($\gamma_\perp \gg \gamma_\parallel \simeq k$). The polarization is then an adiabatic follower of the other two variables, and the dynamical behavior is described by two coupled non-linear equations for the field and population inversion. In this case a single fixed point or periodic oscillations are possible solutions for the steady state, as a bidimensional manifold hosts the dynamics of the system.

Deterministic chaos is not possible unless increasing the number of degrees of freedom for example modulating a parameter, injecting an external field, introducing feedback or increasing the number of active modes.

Finally, for *class C lasers* (some optically pumped gas lasers, Argon and Krypton ion lasers) the three decay rates k, $\gamma_\perp$ and $\gamma_\parallel$ are of the same order of magnitude. The dynamics of such lasers needs the full set of the Maxwell-Bloch equations to be described, and the dimension of the system is high enough to display single-mode instabilities and chaotic dynamics. In fact it was recognized by Haken [22] that the Maxwell-Bloch equations can be transformed in the famous model of Lorentz, one of the first system where sensitive dependence from initial conditions, a fingerprint of deterministic chaos, has been discovered.

II. Dynamics of longitudinal modes in bulk semiconductor lasers

Abstract:
This part of the thesis concerns the analysis of the dynamics displayed by the longitudinal modes of bulk edge emitting semiconductor lasers. The modal dynamics, that in the past was called mode hopping *[23][24], is experimentally studied by means of statistical tools. A dynamical interpretation in terms of a one-dimensional potential and noise is possible in the region of parameters where two coexisting cavity modes are involved. A single stochastic differential equation is then supposed to drive the temporal modal behavior. We observe that the symmetry of the modal emission is affected by current fluctuations. From these measurements we formulate the hypothesis that current fluctuations act as a multiplicative noise term in the stochastic equation of the system. We show that* stochastic resonance *[25] can be demonstrated in this system. Finally the rate equations of the laser are reduced, under some assumptions in the region of mode-hopping, to a single stochastic differential equation, and good qualitative agreement is found with the experimental characterization. The theoretical treatment makes possible to relate the experimental dynamical observables to the internal parameters of the laser.*

In general a big effort is done by constructors in order to grow semiconductor diodes that lase in only one longitudinal mode, i.e. with high degree of temporal coherence. Applications often need this characteristic. Bulk semiconductor lasers generally do operate in a single longitudinal mode, but some regions of instabilities always exist, with a detrimental effect over the spectral purity of the emission. So, from the point of view of applications, it is useful to explore these regions in order to understand the underlying mechanisms and possibly to avoid them. From a dynamical point of view, on the other hand, these regions of instabilities are much more interesting than a perfectly stable behavior.

In bulk semiconductor lasers a dynamical scenario for instabilities is bistability between two longitudinal modes. This means that, in given regions of the parameters (current and temperature of the laser), two cavity modes may coexist, but their strong

mutual coupling prevents the emission of both modes at the same time. Therefore the temporal behavior of the two modes consists of random switchings in antiphase one with respect to the other (i.e. with cross correlation close to -1), the active mode carrying almost the total emitted power. The internal and external sources of noise drive these jumps, so, in the regions of instabilities, each mode can be active for intervals of time randomly distributed, ranging from few μs to ms before being replaced by the other. On the contrary, the total emitted intensity (which is the sum of the intensities of these two main modes) is always constant, and no (or very small) signature of the underlying frequency dynamics is visible unless a diffractive element is used in the monitoring apparatus.

Since the total intensity output remains constant, the two modes can be described as just a one-dimensional system. A simple and useful analogy with this system is the motion of a particle in a bistable (or double well) potential where noise is present. The particle remains in one potential well fluctuating under the effect of noise. This lasts until the strength of the stochastic force is high enough to win the potential barrier between the wells and to bring the particle to the other side. Each stable point (each minimum of the potential) corresponds to the switched-on solution for one mode together with the switched-off solution for the other, while the position of the particle at every time gives the instantaneous ratio between their powers. This analogy can be formalized writing the rate equations for the laser and reducing them to a one-dimensional problem, using the previous argument and time scales considerations. Defining the same variable in the experiment and in the model, the double well potential driving the dynamics of the two modes appears in the reduced equation, reproducing the experimental observations.

We analyze experimentally the changes in the modal dynamics due to a time dependent pumping current (i.e. when a modulation or noise is injected into the current), and we observe some unexpected effects over the symmetry of the potential. These experimental observations indicate that current fluctuations enters in the one-dimensional characterization as a multiplicative term. This is in agreement with the results of the reduced model. Indeed multiplicative noise can be responsible for a change in the symmetry of the solutions of stochastic differential equations.

It is worth noting that *mode hopping* has been observed also for the two possible states of polarization in vertical cavity surface-emitting lasers (VCSELs) [26][27]. A very similar phenomenology is found in these different devices. The rate equations described in sec.II.6 are in fact very similar to that used in the description of polarization modes in VCSELs [6][28].

This chapter is organized as follows. In sec.II.1 we describe the experimental set-up

used for the measurements, then in sec.II.2 we present the general characterization of the bistability of the system by means of time-integrated measurements. In sec.II.3 we resolve the temporal behavior, and we give a statistical characterization of the mode-hopping. The condition of constant bias current will be removed in sec.II.4, where we show the effects of a symmetric modulation of the bias current over the symmetry of the experimental potential. These are interpreted in terms of the multiplicative parameter in the one dimensional description. In sec.II.5 we show that stochastic resonance is possible in this system both avoiding and using the multiplicative nature of the pumping current. Finally in sec.II.6 we describe the rate equations of the laser and their reduction to a one dimensional problem, that qualitatively well reproduces the experimental findings, in terms of a bistable potential with a multiplicative term due to current fluctuations.

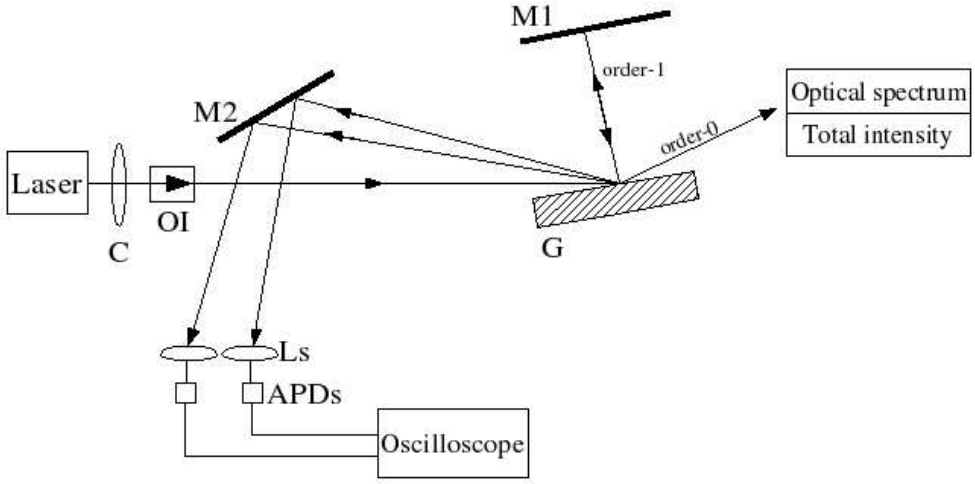

Figure II.1.: Experimental set-up. C: collimator, OI: optical isolator, Ls: lenses, G: diffraction grating, M: mirror

II.1. Experimental set-up

In our experiment we have analyzed two kinds of bulk lasers, three Hitachi HLP1400 and two Sharp LT021MD. Both edge emitting, they have a GaAlAs double-hetero-structure with a bulk active region and cleaved, uncoated facets. The wavelength separation between consecutive longitudinal-modes is around 0.3 nm for both lasers, and the laser emission is in a single-transverse mode with a wavelength around 840 nm for the Hitachi Hlp 1400 and 780 nm for the Sharp LT021MD. All the tested lasers have qualitatively the same dynamical properties, and in the following we will provide a description for the general features they all have in common. Anyway some quantitative detail can be different, as for example the absolute value of the critical parameters where instabilities occur, as it will be defined in the following (sec.II.2).

Even if our aim is a general understanding of the dynamical properties more than an accurate device-dependent understanding of each system, the majority of the experimental observations discussed and showed in this work will be focused on one of the Hitachi HLP1400 devices. This choice is due just to the fact this particular device is widely studied in the literature and some details of the parameters space result to be useful to particular applications that we have tested, as for stochastic resonance (see II.5). This GaAlAs bulk laser has a cavity length of approximately 300 μm and the frequency spacing between internal cavity modes is 125 GHz. The reflectivity of the cavity mirrors is given by the interface and index difference between semiconductor and air, and it is estimated $R \simeq 35\%$.

We need to separate in space the different frequency components in the laser beam. This is possible sending the collimated beam onto a diffraction grating with 1200 lines/mm in grazing incidence in order to illuminate the highest number of lines. The actual experimental set-up is shown in fig.II.1. The laser output needs to be coupled with an AR-coated collimator (C) to compensate the diffraction from the small laser output facet (width $\simeq 10\mu$m, height $\simeq 2\mu$m). In order to increase the resolution of the diffraction element (G), we use it in a double passage scheme. The first order is sent again onto the grating (by the mirror M1) and the first order coming from this last reflection (and going back to the laser) is sent by mirror M2 to the detection system. The resolution at this step is sufficient to separate spatially two consecutive modes of the internal cavity of the laser. An optical isolator prevents the feedback from the dispersion and detection system. The optical signals of the two longitudinal modes are detected by two avalanche photo diodes (APDs) with a bandwidth of 1.5 GHz and the time traces are recorded simultaneously in a Lecroy 7200 oscilloscope (500 MHz analogue bandwidth, 1 GS/s). The zero order (the simple reflection) of the grating can be used to monitor the total intensity, which can be sent to an APD detector (same as before) or to an Optical Spectrum Analyzer, with resolution of 0.06 nm. The laser package temperature is stabilized up to 0.01^oC and the laser current is controlled with a stable (up to 1 μA) power supply.

II.2. Parameters space

We give in this section a general description of the phenomenological properties of the laser. We will describe the behavior of the system in its free running regime by means of time averaged measurements. We will find then in the parameters space the region of bistability where hopping between two longitudinal modes occurs.

The two experimental parameters are the bias current J of the diode and the temperature of its substrate T_{sub}, which is controlled by a Peltier element. Dealing experimentally with the substrate temperature is more difficult than with the bias current, because of the high thermal capacity of the laser package that makes long (seconds) the time needed to reach the thermal equilibrium once the Peltier driver settings are changed. All the following measurements have been taken at steady temperature of the whole laser package.

Regarding the role of the bias current J, in principle it involves many different and contrasting effects. It affects the carrier density inside the active region as the active region temperature T, which is changed by Joule heating. In fact, the resistance of the diode is few Ohm so the power dissipated in heat is of the order of few tens of mW at a typical current of 100 mA. Even subtracting the emitted power, which is only few mW, it is clear that the heating inside the active region becomes important, so T becomes coupled to J. From a microscopic point of view, the electron distribution in the conduction band is affected by the temperature T according to the Fermi-Dirac probability distribution dN, which has a term proportional to $dE\sqrt{E}/(1 + exp[(E - E_{fc})/K_BT])$ in bulk lasers [14]. Therefore an increase of the temperature makes the distribution larger towards higher energies, while its peak decreases towards lower energies as shown qualitatively in fig.II.2. The increase of the pumping current, generating an increase of the active region temperature, then has the effect of a red shift of the gain peak.

On the other hand the index of refraction of the host material is also affected by the active region temperature T. For GaAs the temperature dependence of the refractive index has the typical value of $2\ 10^{-4}\,K^{-1}$[29]. Then the index increases with increasing temperature, and both the mode wavelength λ and the mode spacing $\Delta\lambda$ are affected. Therefore the entire comb of cavity modes red shifts increasing the current. Other effects are taken into account in the theory of semiconductors and are present inside the active medium, such as band filling and band-gap renormalization [14]. The former induces a blue-shift and an increase of the gain peak, together with a broadening of the gain curve towards high energies. The latter is due to the screening effect of the Coulomb interaction between electrons and holes and determines a red-shift of the gain peak. In order to find which are the dominant effects in our devices as the current is increased, it is necessary to observe the experimental optical

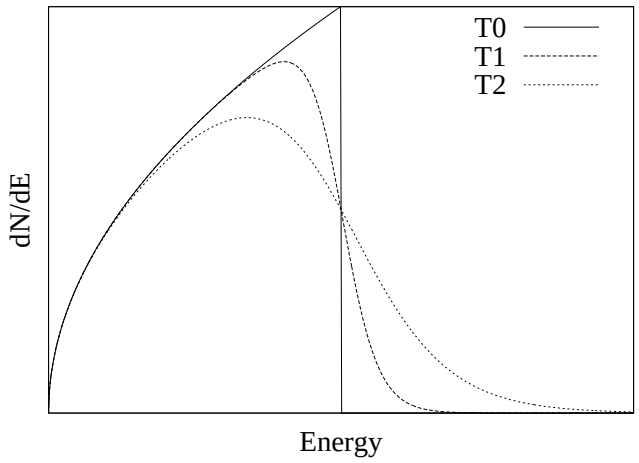

Figure II.2.: Carrier distribution shape as a function of the energy for a bulk laser for three increasing temperatures $0 = T_0 < T_1 < T_2$.

spectrum.

In fig.II.3 we show the optical spectrum (integrated over a time interval of the order of 2 s) as a function of the bias current J, keeping fixed the temperature of the substrate T_{sub} at 19.7^{o}C. For low current the emission is not yet coherent but the spontaneous emission is already filtered by the Fabry-Perot transmission function. For this temperature the laser threshold is reached around 81 mA, where the emission becomes single-mode. We will refer to the mode active at threshold as "mode $(-)$". For higher levels of current the identity of the active mode changes. Even though the emission is almost always mono-mode, mode $(-)$ loses its stability in a small region around 87 mA, where the next mode towards higher wavelengths ("mode $(+)$") switches on. We call this region of parameters *transition* or *switching region*. This is the evidence of the red-shift of the gain curve with increasing current.

The global identity red-shift of the active mode, as the current is increased, can be explained in first approximation with a lower red-shift rate of the resonant comb of modes (which is visible as a slight slope of each horizontal line in fig.II.3) with respect of that of the gain curve [30][31]. However this general physical mechanism alone cannot explain the particular behavior of each device, as for example transitions between two modes separated by many free spectral ranges, as around 118 mA in fig.II.3. More complex microscopic effects should be taken into account, and a detailed description would necessarily become device-dependent. In our work we have tried to find a general dynamical description of such transitions involving two modes, studying the properties they all have in common. This means that even if we focus the following

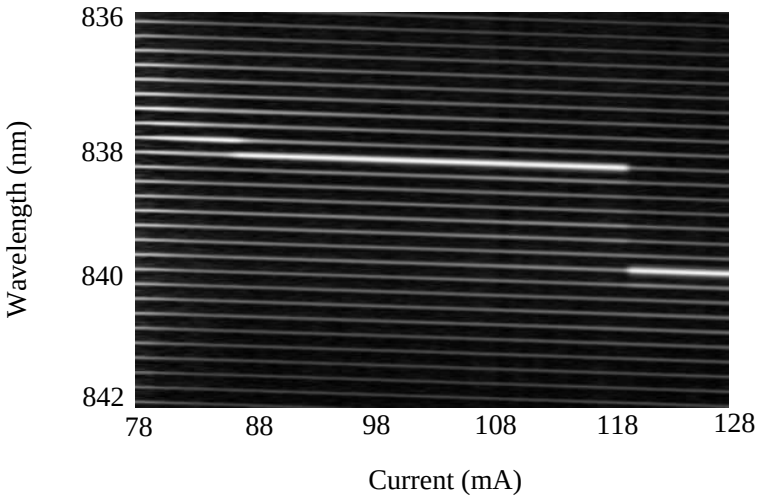

Figure II.3.: Integrated optical spectrum as a function of the bias current J. Each measured optical spectrum has been normalized to the total intensity output in order to show the mode suppression ratio at each current value. The normalized modal intensity has been represented in a logarithmic scale using a grey scale from black (-34 dB) to white (-8 dB). $T_{sub} = 19.7^{o}$C

characterization on the first transition where two close modes are involved, the same behavior is qualitatively found in all the tested devices also for transitions at higher current for modes which are not neighboring in the spectrum.

The average emitted modal intensity as a function of current for both dominant modes is shown in fig.II.4. It appears that, keeping fixed the temperature T_{sub}, in the small transition region of pumping current between $J = 87$ and $J = 88$ mA, both modes are (in average) lasing. In this region the ratio of the modal powers depends on the current, and there exists a value of J for which both have the same average intensity.

The range of current where the laser switches its active mode depends on the value of the substrate temperature T_{sub}. In fig.II.5 we show the value of the mode suppression ratio δ in the parameters space, calculated as the difference of power between the two main modes of the optical spectrum. Following a path at constant temperature, i.e. moving along a vertical line, at low current (around 80 mA) a black region (A), which indicates $\delta < 5$ dB, is found, corresponding to the colored spontaneous emission. In fact, close to threshold many modes have similar intensities. For higher current (83-84 mA) the threshold is reached and mode $(-)$ starts to lase. The gray region (corresponding to 5 dB $< \delta <$ 10dB) indicates that mode $(-)$ increases

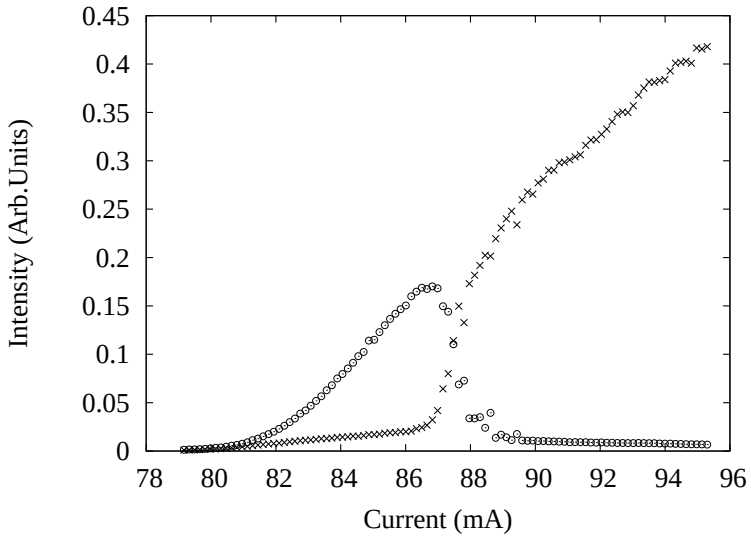

Figure II.4.: LI curve resolved for the two dominant modes. Circles: mode (−), crosses: mode (+). The temperature is 19.7^{o}C as in fig.II.3

its power over the other modes. The transition to mode (+) happens crossing the black region (B) around 90 mA ($\delta < 5$ dB) towards higher currents, where mode (+) grows up and reaches the same power (in average) as mode (−). Then for higher currents (95 mA) mode (+) takes all the emitted power.

The central black region (B) is the transition region of parameters where we will focus our attention. It is worth noting that for different devices we have found different shapes for the mode suppression ratio map as shown in fig.II.5. We will see in sec.II.5 how the characteristics of the transition region shown by the HLP1400 device will be useful in the treatment of stochastic resonance.

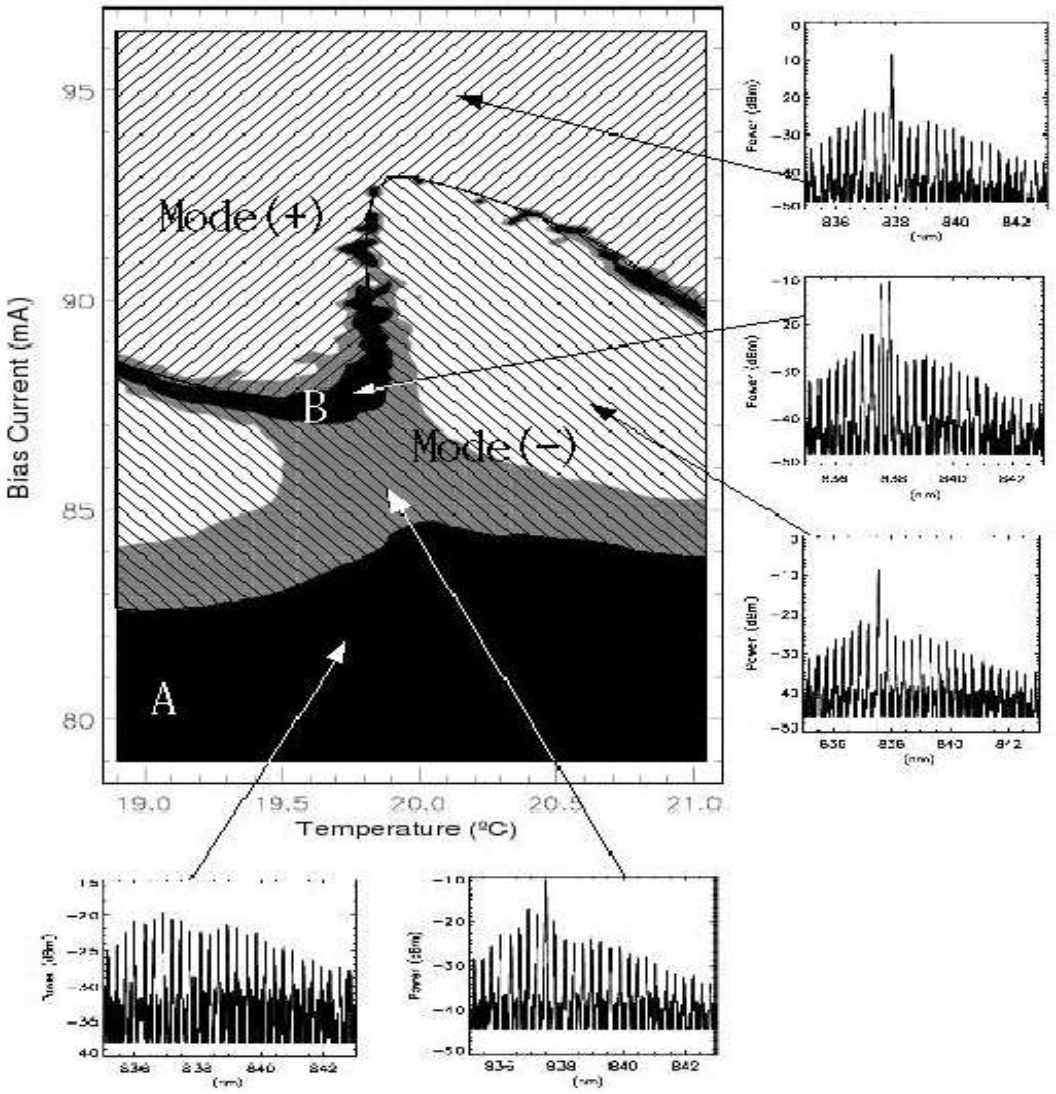

Figure II.5.: Map of the mode suppression ratio in the parameters space of the HLP1400 device. The black regions correspond to $\delta < 5dB$, the gray regions to $5dB < \delta < 10dB$, the white regions to $\delta > 10dB$, where δ indicates the difference in power between the two main modes present in the optical spectrum. Above threshold the identity of the active mode can be stated, and it is represented by the dashed regions. The *transition region* is the central black line (B) where both modes (−) and (+) are active. The black region (A) corresponds to the spontaneous emission filtered by the cavity below threshold. The relative optical spectra are shown.

II.3. Modal dynamics: mode hopping analysis

II.3.1. Phenomenology

We are now interested in time resolving the behavior of each mode in the bistability region of parameters where both modes (+) and (−) coexist in average in their active solution, and give a characterization of the transition as a function of the current parameter J.

The typical time traces of the two modes in the mode hopping regime are shown in fig.II.6 (left). Here the current is increased while the temperature is fixed at 20.8^oC in order to cross the switching region. For a given current J, each mode is active for a time interval that depends on J: mode (−) stays active an infinite interval of time for J close to 88 mA, i.e. in its stability region. Approaching the transition region, this time decreases and mode (+) starts to become active for very short intervals of time (few μs), as in fig.II.6 up. There exists a value of current for which the intervals of activation are the same for both modes, as in fig.II.6 (middle). Increasing further the current (see fig.II.6 bottom), mode (−) becomes active less frequently than mode (+) and the optical power is in average shifted to the latter, as can be seen also in the probability distribution for the intensity of each mode which is plotted in logarithmic scale in the right panels. As can be seen from these probability distributions, the switching time, or the amount of time spent by the system in passing from one solution to the other, is 3 order of magnitude lower than the time spent in each solution. This switching time is about 9 ns, and it is found that it does not depend critically on the values of the parameters.

The degree of anti-correlation of this modal dynamics is very high. The activation of one mode necessarily happens together with the switching-off of the other, and this is true at high frequencies, i.e. when just one spike of few μs appears in both traces but with different sign, as for low frequencies, i.e. for a complete switching of solution. Keeping fixed the temperature, we extract from the two time series ($I_1(t)$, $I_2(t)$) the value of the cross-correlation function $\langle I_1(t_0)I_2(t_0+t_1)\rangle$ as a function of t_1. This correlation shows a minimum, close to -1, always in the first experimentally accessible point, i.e. for $t_1 \leq 1$ ns, while for $t_1 \to \infty$ it tends to zero. Varying the bias current around the transition region, the value of the cross-correlation minimum is affected. The value of this minimum is shown in fig.II.7 as a function of the bias current (and of the symmetry indicator η that will be defined in eq.II.4). It results that the anti-correlation between the modal signals is always very good along the transition region, the minimum of the cross-correlation being always close to -1. The maximum degree of anti-correlation (-0.99) is reached for $J = 91.6$ mA (the center of the transition region), and even at the borders of the bistability region the cross-correlation keeps

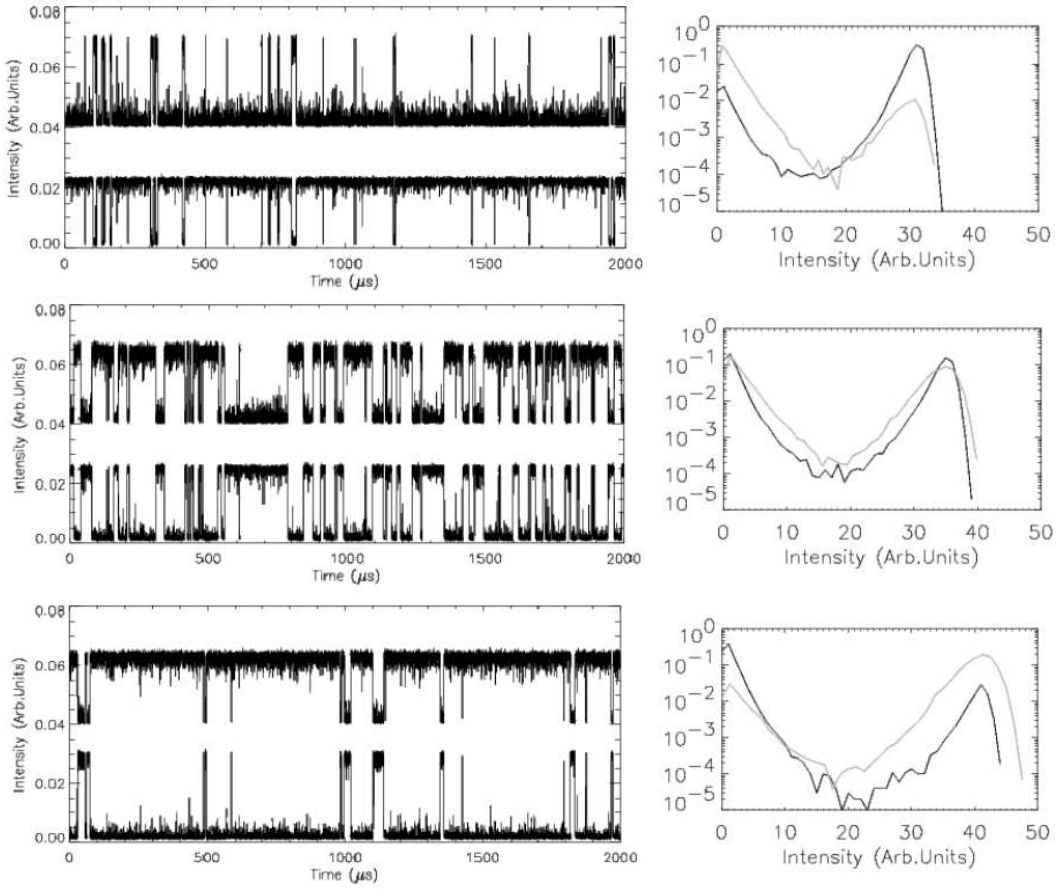

Figure II.6.: *Left panel*: time traces of the two modes at $T_{sub} = 20.9^{o}$C. The trace of mode (+) is shifted up vertically by a fixed offset (0.04 a.u.) for clarity. *Right panel*: corresponding normalized probability distribution of the modal intensity. Black line: mode (-), grey line: mode(+). From top to bottom: $J = 91.3$ mA, $J = 91.6$ mA, $J = 91.9$ mA.

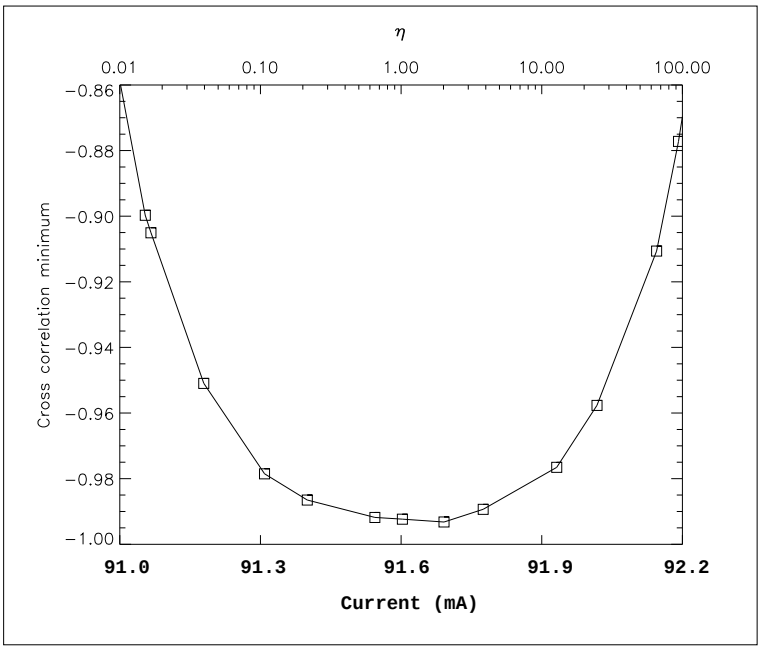

Figure II.7.: Value of the cross correlation minimum (which is always found for $t \leq 1$ ns) as a function of the bias current J and of the symmetry indicator $\eta(J)$ (defined in eq.II.4). The temperature is 20.9^{o}C, as in fig.II.6.

its value around -0.9 . The increasing value of the cross-correlation minimum at the limits of this current region, where fast spikes are present in the modal signals due to the strong asymmetric modal emission, could be explained, at least partially, by a lack of temporal resolution.

This antiphase dynamics implies that the sum of the two intensities keeps a constant value (with the small amount of noise from spontaneous emission). In fact the total intensity time trace, recorded in the transition region where mode hopping occurs, shows an AC variation due to the underlying modal dynamics of less than 1% of its DC component. Therefore the dynamics of the two modal intensities can be described by only one quantity, as their sum (the total intensity) remains constant during their evolution.

II.3.2. Statistics

It is important to understand the origin of the switching between modes, and find out if determinism and/or noise rules such dynamics. If there exists some law driving the evolution, it should be possible in principle to extract some informations from statistics of the temporal traces. The natural observable is the residence time of each mode, defined as the time interval between the switching on and the switching off

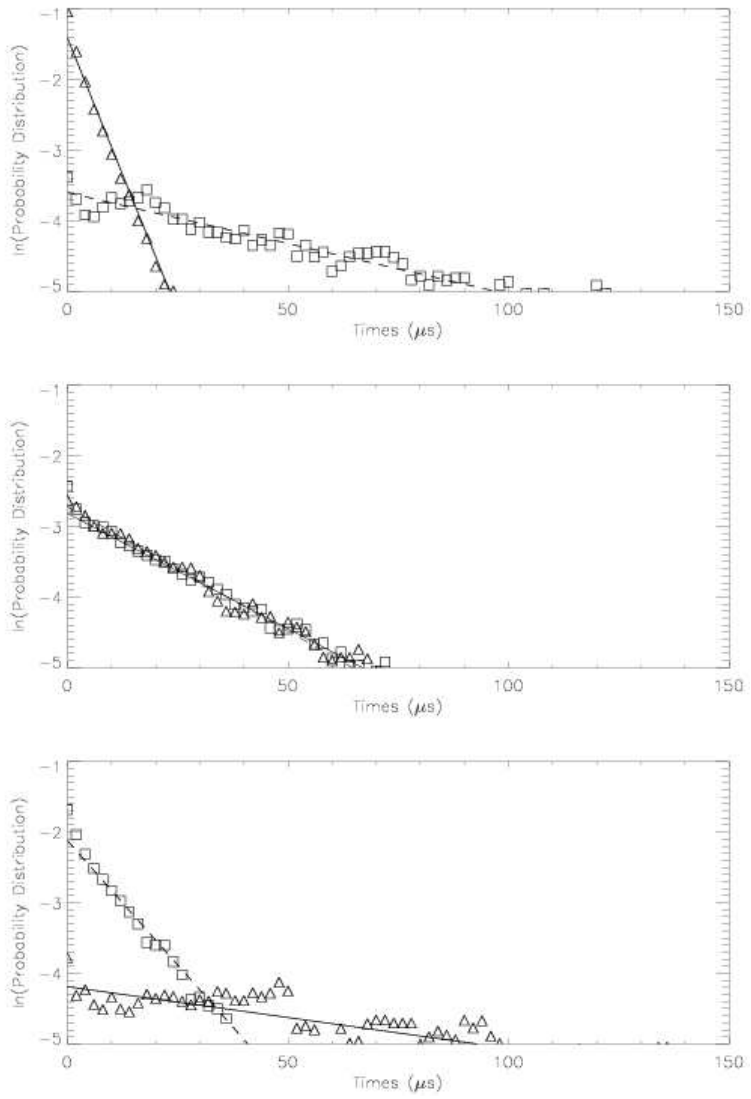

Figure II.8.: Logarithm of the probability distribution function for the residence times. Mode (−): squares, mode (+): triangles. J is increased from top to bottom: 91.3, 91.6, 91.9 mA. $T_{sub} = 20.9^{o}$C.

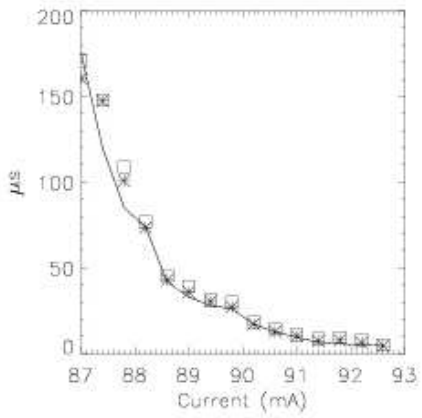

Figure II.9.: Residence times analysis: the mean value $\langle\tau\rangle$ calculated directly from the time series is drawn as a continuous line. The value of $1/\lambda$ from the exponential distribution is plotted as squares. The standard deviation σ is plotted as stars. $T_{sub} = 20.9^oC$

event of a given mode.

We extract from a time series the intervals of time $\{\tau_i\}$ during which each mode is active [32]. In fig.II.8 we plot the probability distributions of the observable τ, extracted from long time series (1M points, more than 10^3 events). As it appears, the experimental probability distribution $P(\tau)$ has an exponential shape, $P(\tau) = A_0\, exp(-B_0\tau)$, with coefficient $-B_0$ depending on the level of injection current. For a current $J = 91.6$ mA the distributions of the two modes are equal, this defines the symmetric point of the transition region.

The exponential, or van't Hoff-Arrhenious [33][34], distribution is also called the "memoryless" distribution, because it describes observables that show a dynamics where no deterministic link is possible between an event and the following (as radioactive decay for example). In other words, the probability of observing an event at time $t + s$ after the occurrence of an event at time t, is independent from t and depends only on s. The first event at t is "forgotten". In these cases the dynamics is referred as noise driven, in order to underline that a source of noise (which is a memoryless process) is necessary to explain the behavior of the variable [35].

For a normalized exponential distribution $P(\tau) = \lambda\, e^{-\lambda\tau}$ is easy to show that the mean value of the variable τ is related to λ, together with the standard deviation $\sigma = \sqrt{\langle\tau^2\rangle - \langle\tau\rangle^2}$, by

$$\langle\tau\rangle \;=\; \frac{1}{\lambda} \;=\; \sigma \tag{II.1}$$

We have then calculated the experimental values of $\langle\tau\rangle$, $\frac{1}{\lambda}$ and σ from long time series,

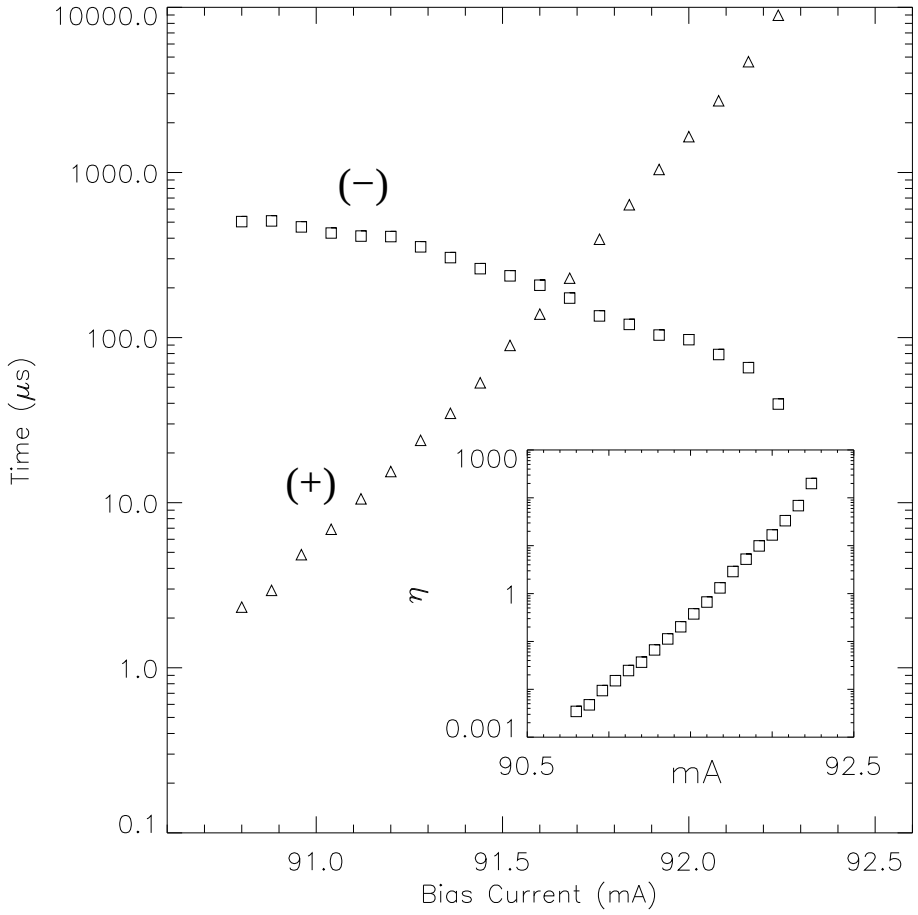

Figure II.10.: Average residence time τ_- and τ_+ as a function of pumping current for mode $(-)$ and mode $(+)$. Inset: the symmetry indicator $\eta = \langle\tau_+\rangle/\langle\tau_-\rangle$ as a function of the pumping current. $T_{sub} = 20.8^oC$.

and the difference between them is very low, being more important where the statistics are calculated over less events, as shown in fig.II.9 for mode $(-)$. A similar result holds for mode $(+)$. Therefore we can conclude that the exponential distribution describes well the distribution of the variable τ, so we will consider the jumps between modes as triggered by noise. The most known source of noise in semiconductor lasers is spontaneous emission, but noise is also inevitably present in the bias current.

II.3.3. Modal emission symmetry

In order to better characterize the bistable transition, we measure simultaneously the average residence time $\langle\tau_\pm\rangle$ for both modes as a function of the bias current J, keeping fixed the temperature, and the result is plotted in fig.II.10.

The dependence of the average residence times as a function of J is found to be close to exponential:

$$\langle \tau_- \rangle \simeq A_- \, exp(-B_- J) \tag{II.2}$$

$$\langle \tau_+ \rangle \simeq A_+ \, exp(B_+ J) \tag{II.3}$$

with $B_\pm > 0$. Increasing the current, while the average residence time of mode $(-)$ decreases, it increases for mode $(+)$. The symmetry of the emission is found at the intersection of the two curves, at 91.65 mA for the temperature used (20.8^oC), where both modes are in average the same amount of time in their on-solution. It is worth noting that the slope of the two curves (in logarithmic scale) is not just one the opposite of the other, i.e $B_- \neq B_+$, but $B_+ > B_-$. This leads to an increase of the mean quantity $(\langle \tau_- \rangle + \langle \tau_+ \rangle)/2$ with the pumping current, which means that the system, in addition to a change of the symmetry between modes, tends to globally jump less often between the two modes as the current is increased.

The symmetry between the modal emissions can be quantified by means of a single number, given by the ratio between the average residence times of the two modes. We call this symmetry indicator η and we plot it in the inset of fig.II.10 as a function of the current:

$$\eta = \frac{\langle \tau_+ \rangle}{\langle \tau_- \rangle} \tag{II.4}$$

As it can be seen, the logarithm of η is almost linear with the pumping current. For low steady current levels, if mode $(-)$ is n times more probable than mode $(+)$, then $\eta = 1/n$. For the current where both modes have the same probability to be found in their on-solution, $\eta = 1$ is measured, indicating the symmetric emission. Finally for higher currents, where mode $(+)$ becomes n times more probable than mode $(-)$, one finds $\eta = n$.

Summarizing the presented results, we have seen that mode hopping is a stochastic process driven by internal and external sources of noise. Because of the action of noise, the system visits randomly in time the two possible stable states, which correspond to the emission of each mode, with probability that depends on the value of the current parameter, and that can be measured by means of the quantity η. Moreover, in the hopping regime, one quantity (the total intensity) is conserved while the two variables (the two modal intensities) evolve in time, as indicated by the cross-correlation. Due to this fact, it is possible in principle to describe the evolution of the two modal intensities by means of just one variable. Its dynamics is very similar to that displayed by a particle in a bistable potential under the effect of noise, as it will be discussed in the next sections after a brief overview of the theoretical background.

II.3.4. Noise, potential barriers and probability: overview

II.3.4.1. Langevin approach

The action of noise over the motion of particles is a problem that somehow was born with the first observations of brownian motion in 1827 [36]. L.Boltzmann in 1896 already had the intuition that this motion depended on the fluctuations of atmospheric pressure. In 1905 Einstein first gave a good explanation in probabilistic terms of such a behavior, followed by Langevin in 1908 who concentrated his view in the microscopic scale, in a way complementary to Einstein. Einstein's description was based on a coarse-grain time τ and no attempt was made to describe the trajectories of brownian particles for times below τ. The trajectories were not followed continuously in time. Langevin instead described the single particle, writing the corresponding Newton's law. The force $\xi(t)$ needed to explain the motion had to be fluctuating randomly in time and it is today called *noise* from the electric circuits analogy. The characteristic of the Langevin description is the fact that the force explicitly enters in the equation of the single particle, so one can obtain directly the trajectory integrating the equation for a given realization of the stochastic force.

The general Langevin equation is a particular stochastic differential equation [37] where the fluctuating term $\xi(t)$ appears linearly, and takes the following form:

$$\frac{dx}{dt} = f(x,t) + g(x,t)\xi(t) \tag{II.5}$$

where $g(x,t)$ is called the *diffusion* term, $f(x,t)$ the *drift* term and $\xi(t)$ is the noise. If $g(x,t)$ is a constant the noise is called *additive*, otherwise it is called *multiplicative*. The noise term is characterized by the expression of its mean value, which is usually zero $\langle\xi(t)\rangle = 0$, and its temporal auto-correlation function. The latter defines the amplitude of the fluctuating force by means of the variance D_o^2 and its spectrum, by means of a characteristic time τ:

$$\langle\xi(t)\xi(t')\rangle = D_o^2\, h_\tau(t) \tag{II.6}$$

With the choice $h_\tau(t) = \delta(t-t')$ the noise is called *white*, in the sense that the spectrum is formed by all the frequencies, and the correlation time τ is zero. A filtered spectrum for the noise is obtained by some dependence on t of $h_\tau(t)$. The Ornstein-Uhlenbeck process is the most frequently used, and it is defined by $h_\tau(t) = exp(-|t|/\tau)$. This is a realistic way to model a real source of noise, as a function generator, which has always a low-pass filtered spectrum. The maximum frequency is proportional to $1/\tau$, so the white noise limit is recovered if $\tau \to 0$.

Focusing on our system, we said that there exists a strong analogy between the laser in the mode hopping regime and a particle moving in a double well potential.

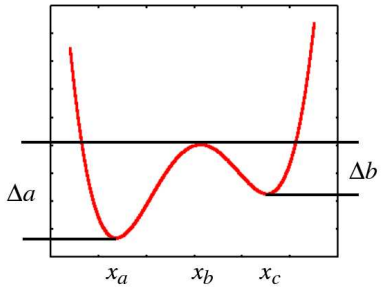

Figure II.11.: A generic asymmetric double well potential

Therefore we are interested in the equation of motion along x of a particle of mass M in a deterministic potential $U_o(x)$, with noise $\xi_o(t)$ and friction γ. The corresponding equation of motion is

$$M\ddot{x} = -U_o'(x) - \gamma M\dot{x} + \xi_o(t) \tag{II.7}$$

In the case of overdamped motion, i.e. $\gamma \gg 1$, the velocity $v = \dot{x}$ can be adiabatically eliminated imposing $\dot{v} = 0$, then finding the stationary value. In this limit the Langevin equation becomes a widely used rate equation with a rescaled potential and noise $U(x) = U_0/(M\gamma)$, $\xi(t) = \xi_0/(M\gamma)$.

$$\dot{x} = -U'(x) + \xi(t) \tag{II.8}$$

The problem of finding the escape time over a potential barrier of a particle subjected to a Langevin force is a subject of study since Kramer [38] in 1940, and the interest of researchers goes from chemistry to nuclear physics [39]. Given a bistable potential $U(x)$, like the one in fig.II.11, the theory developed by Kramer gives the escape rate probability r from one well to the other in terms of the ratio between amplitude of noise D_o and potential barriers Δa, Δb. In the overdamped limit it takes the form:

$$r_{a\to c} = \frac{\sqrt{U''(x_a)|U''(x_b)|}}{2\pi\gamma}\, e^{-\Delta a/D_o} \tag{II.9}$$

$$r_{c\to a} = \frac{\sqrt{U''(x_c)|U''(x_b)|}}{2\pi\gamma}\, e^{-\Delta b/D_o} \tag{II.10}$$

where $U''(x_i)$ $(i = a, b, c)$ is the second derivative of the potential calculated at the extrema x_a, x_b, x_c . In the original paper [38] the term D_o was replaced by the Boltzmann coefficient $1/K_BT$, because the source of noise was modeled as an external thermal bath.

II.3.4.2. Fokker-Plank approach

The Fokker-Plank formalism is a powerful tool that allows one to find the stationary solution for the probability distribution function $\mathcal{P}(x,t)$ of the system. A general stochastic equation can be written as

$$\dot{x} = C(x) + F(x,t) \tag{II.11}$$

with $C(x) = -dV(x)/dx$ derivative of the deterministic potential and $F(x,t)$ fluctuating term with zero mean and auto-correlation given by

$$\langle F(x,t)F(x,t')\rangle = 2D(x)\delta(t-t') \tag{II.12}$$

The *diffusion coefficient* $D(x)$ is constant if the stochastic term does not depend on x, i.e. if the noise is not multiplicative. The Fokker-Plank equation gives the temporal evolution of the probability distribution $\mathcal{P}(x,t)$

$$\frac{\partial \mathcal{P}(x,t)}{\partial t} = -\frac{\partial}{\partial x}[A(x)\mathcal{P}(x,t)] + \frac{\partial^2}{\partial x^2}[D(x)\mathcal{P}(x,t)] \tag{II.13}$$

The term $A(x) = C(x) + \frac{1}{2}\frac{dD(x)}{dx}$ is the *drift* coefficient. The general stationary solution of eq.II.13, which does not depend on t, is quite simple to write in terms of a new quasi-potential $U(x)$ and reads

$$\mathcal{P}(x) = Q\, e^{-U(x)} \tag{II.14}$$

where Q is the normalization constant, and the quasi-potential is

$$U(x) = -\int \frac{C(x)}{D(x)}\, dx + \frac{1}{2}\ln(D(x)) \tag{II.15}$$

In the case where $D(x)$ is a constant not dependent on x, i.e. the noise is simply additive, it is immediate to see that the quasi potential reduces to the original potential $V(x)$ rescaled with the noise strength D

$$\mathcal{P}(x) = Q\, e^{-V(x)/D} \tag{II.16}$$

The result of eq.II.14 is useful from the experimental side because it is possible to use it backwards. In fact, we can measure experimentally the stationary probability distribution $\mathcal{P}_{exp}$ of the variables of our system, simply recording long time series with stationary parameters and extracting the desired statistical distributions. Therefore the experimental (quasi-)potential of the chosen variable x is found inverting eq.II.14, i.e. displaying the function

$$U_{exp}(x) = -\ln(\mathcal{P}_{exp}(x)) + cst \tag{II.17}$$

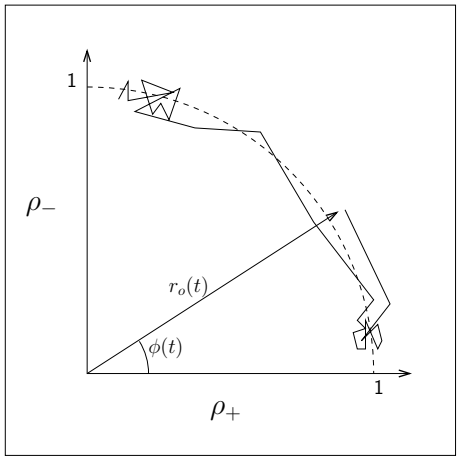

Figure II.12.: Sketch of a trajectory of the system in the (ρ_+, ρ_-) plane.

II.3.5. Experimental one-dimensional description

As discussed previously, due to the fact that the two experimental variables are strongly anti-correlated, only one quantity is sufficient to describe the modal intensities in the mode-hopping regime. Therefore we discuss here the chosen one-dimensional description of the two experimental modal intensities. This is done defining a new variable, function of the two experimental modal intensities. Let ρ_+^2 and ρ_-^2 be the intensity of mode (+) and (−) respectively, normalized to the average total intensity i_{tot}:

$$\rho_\pm^2 = I_{(\pm)}/i_{tot} \tag{II.18}$$

The amplitudes $|E_\pm|$ of the electric field of each mode are then proportional to $\rho_\pm$.

The hopping between the two modes can be visualized by means of the phase space (ρ_+, ρ_-), as it is schematically shown in fig.II.12. In this plane the position of the system at each time t can be indicated, in cylindrical coordinates, by the vector $r(t) = r_o(t)e^{i\phi(t)}$ whose modulus is the instantaneous total intensity normalized to the average value, while its angle ϕ with the horizontal axis carries the information of the ratio between the two emitted modal intensities.

The probability distribution of the points visited by the system in the experimental phase space is shown in the first row of fig.II.13 for three increasing levels of pumping current keeping the temperature fixed, the most visited regions being marked in black. The phase space shows the presence of two fixed points (close to the two axis at $\phi \simeq 0$ and $\phi \simeq \pi/2$) corresponding to the emission of each mode. The distance of these stable points from the relative axis is due to spontaneous emission which prevents one mode to have zero intensity when the other is active. The condition of almost constant total intensity imposes the dynamics to remain close to the arc of circle with

unitary radius. The radial width of the distribution is then proportional to the noise present in the total intensity. It is clear how the symmetry of the emission changes across the transition region, passing with increasing current from $\eta < 1$ (left) where mode $(-)$ is the most probable, trough $\eta = 1$ (center) where both modes have the same probability, to $\eta > 1$ (right) where mode $(+)$ becomes predominant.

The noise acting on the system can be separated in two components by means of the definition of $r_o(t)$ and $\phi(t)$. The radial component (that can be called "in phase" component) of the noise affects the total intensity with a change in r_o , by a variation with the same sign in the two modal intensities. The $\phi-$component instead (or "anti-phase"component) changes the energy balance between the modes, with a change of ϕ due to a variation with opposite sign of the two modal intensities.

In order to describe the system by means of only one variable, we decide to disregard the "in phase" component of the noise, which is related to the noise in the total intensity, and describe the evolution of the system by the dynamics of the variable $\phi(t)$ alone. This variable describes the hopping between the two modes showing random jumps in time (triggered by the $\phi-$component of the noise) between two stable points close to $\phi \simeq 0$ (corresponding to mode $(+)$) and $\phi \simeq \pi/2$ (corresponding to mode $(-)$). This simplification, equivalent to neglect fluctuations in the total intensity (which are of the order of 20% of the DC value), is justified by the fact that dynamically the interesting switching mechanism between the two modal energies is in antiphase in the modal signals.

Therefore we extract from the probability distributions in the phase space (first row of fig.II.13) the distribution $\mathcal{P}_{exp}(\phi)$ of the variable ϕ. The potential $U(\phi)$ is then given by $U(\phi) = -\ln(\mathcal{P}_{exp}) + \text{const}$ (see eq.II.17), and it is plotted in the second row of fig.II.13. In other words, projecting the dynamics on the unitary arc of circle, which corresponds to flat total intensity, we can find the probability distribution and the corresponding potential U of the angle ϕ, which is given from the measurement of $\rho_\pm$ by

$$\phi(t) = \text{atan}\left(\frac{\rho_-(t)}{\rho_+(t)}\right) \tag{II.19}$$

II.3.6. Dynamical hypothesis

We can now better formalize, by means of the variable ϕ, the analogy between the laser in the mode-hopping regime and the motion of a particle in a bistable potential under the effect of noise that we discussed above. All the presented results indicate that the same stochastic differential equation can describe the two systems. The experimentally observed laser dynamics, in terms of the variable ϕ, is in agreement

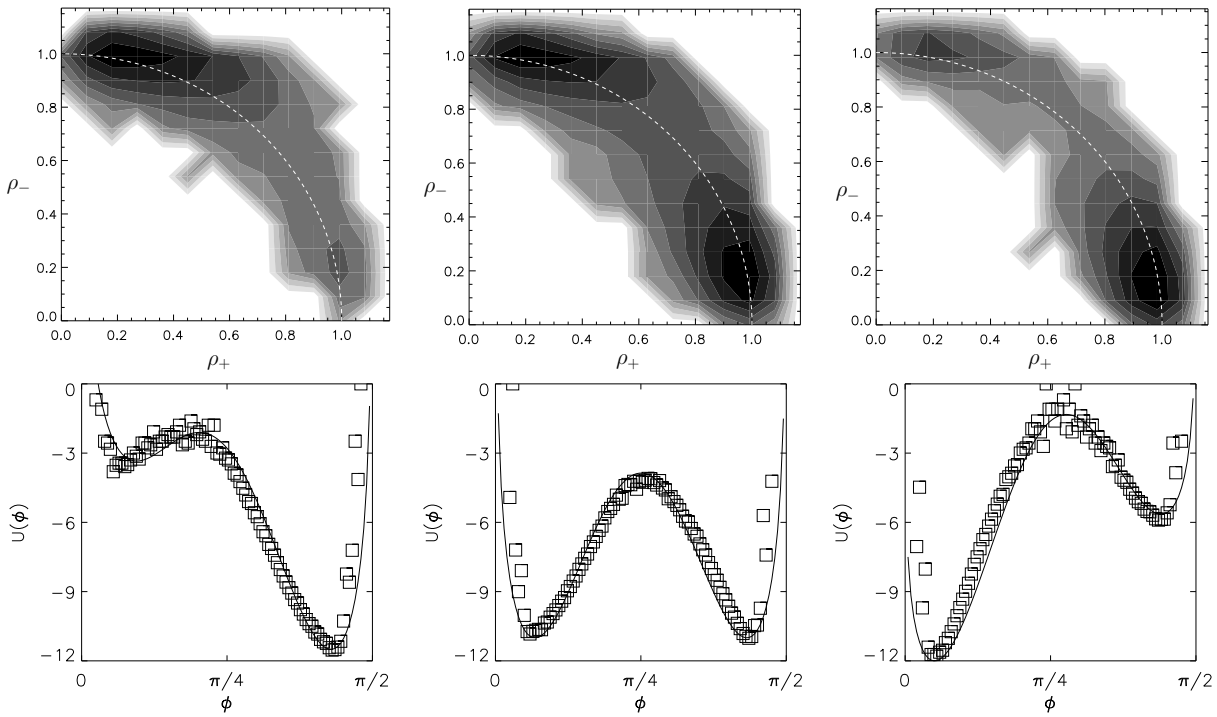

Figure II.13.: *First row:* normalized probability distribution of the experimental system in the phase space defined in the text. The colorscale goes from black (high probability) to white (low probability) in logarithmic scale. The bias current increases from left to right, crossing the transition region. *Second row:* the experimental quasi-potential of the variable ϕ is indicated by the points for the corresponding situations in the first row. The line is the the fitting of the experimental points using the expression derived in the reduced model that will be described in sec.II.6 [with parameters: $a = 85$, $b = -18.7$, $D_\phi = 4.9$, $c = -8.1$ (left); $a = 108.5$, $b = 0$, $D_\phi = 4.6$, $c = -10.6$ (center); $a = 90$, $b = 13.5$, $D_\phi = 2.5$, $c = -7.2$ (right)].

with the one-dimensional description given by

$$\dot{\phi} = -U'(\phi, J) + \xi_\phi(t) \tag{II.20}$$

Here the bistable potential $U(\phi, J)$, extracted from the data (as in the second row of fig.II.13), is the deterministic part giving the two stable solutions, corresponding to the stable emission of each mode. Its symmetry, in terms of potential barriers, depends on the DC current J and can be quantified by the value of $\eta(J)$. The term $\xi_\phi(t)$ corresponds to the noise, assumed additive, projected along the ϕ-direction. This stochastic force is responsible for the random jumps of ϕ between the two stable points defined by the potential U.

In conclusion, the above assumption is valid when the bias current is constant in time. In the following section we will show how eq.II.20 should be changed in order to take into account the observed effect of current modulations.

II.4. Pumping current modulation and multiplicative stochastic effects

We present here the experimental study of the effects of a modulation of the pumping current parameter on the modal dynamics of the bulk laser. The interest comes from the fact that semiconductor lasers are mostly used in applications where the pumping current is modulated. It is important then to understand its role in those regions of the parameters where instabilities occur. Moreover, as the laser in the mode-hopping regime can be described in terms of a bistable potential with noise, we are interested in demonstrating that stochastic resonance [25] can be found in this system. In this case modulating the potential wells periodically and injecting a controllable amount of noise into the system becomes essential, so we will study if this is possible acting on the bias current.

We will see that, in the mode-hopping regime, the symmetry of the experimental bistable potential is, unexpectedly, affected by a symmetrical current modulation. This is true for periodic as for noisy modulations. This change in the potential symmetry suggests that the experimental one-dimensional characterization stated by eq.II.20 should be expanded, including the bias current fluctuations as a new multiplicative term of the equation. Stochastic resonance can be demonstrated, either implementing a more involved way to change the time scale of the hopping as compared to simply adding noise into the current, either using this change of symmetry in the modal emission.

II.4.1. Effects of noise and sinusoidal modulation

We add experimentally to the bias current of the laser the voltage *noise* produced by a function generator (hp 33250A), which have zero mean, gaussian shape, bandwidth ranging from 100 Hz to 50 MHz and whose amplitude is a controllable parameter. In this case the DC component of the bias current is fixed independently in order to have, in absence of external noise, symmetry between the two modes, i.e. $\eta = 1$. However, the results are qualitatively the same for every choice of the starting value of η (unless the system is brought outside the transition region). For increasing levels of the noise strength, we extract from the time series the mean residence time of each mode, and we plot them in fig.II.14 (right). The effect of such modulation is twofold: on one hand the dynamics is accelerated, this means that the residence times are in average decreased. This can be understood easily because the probability of passing the potential barrier increases with increasing noise. On the other hand, this variation is not symmetric for both modes. The average residence time of mode (+) is strongly

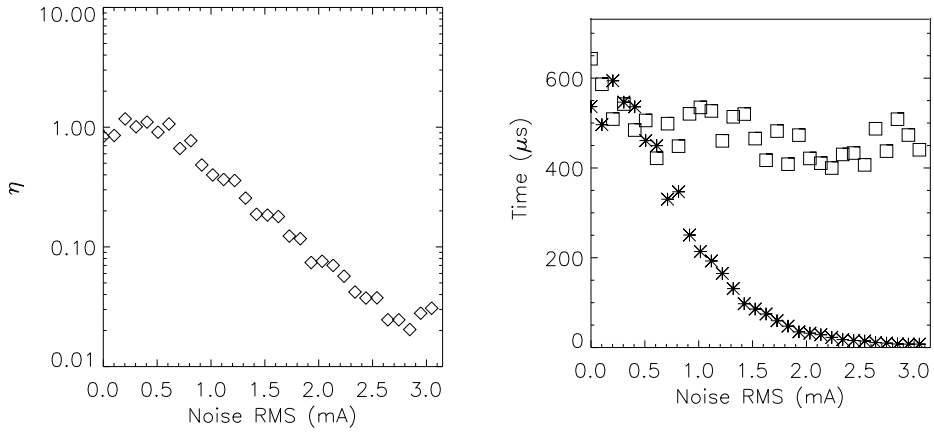

Figure II.14.: *Right:* Average residence times for increasing levels of noise amplitude. Squares: mode (−), stars: mode (+). *Left:* Values of the potential symmetry measured by η for increasing noise amplitude. The DC level of the current is 91 mA, the laser threshold is 83 mA.

reduced, while the variation is smaller for mode (−). The average residence time of mode (−) is reduced but it remains always of the order of its noise-free value (around 500 μs), while for mode (+) it goes from this value to few μs. The variation of almost two orders of magnitude of the symmetry indicator η, shown in fig.II.14 (left), clearly indicates that the symmetry of the potential is strongly affected by the injection of noise.

Following the analysis presented in sec.II.3.5, we show in fig.II.15 the experimental potential $U(\phi)$ extracted from the data, relative to each level of noise strength of fig.II.14. The potential well relative to mode (−) (close to $\phi = \pi/2$) becomes deeper increasing the noise amplitude, while the depth of the one relative to mode (+) (close to $\phi = 0$) decreases. In other words, noise makes mode (−) in average more stable and more probable than mode (+). At the same time, jumps from one well to the other become more frequent, but statistically the system spends more time close to the solution "mode (−) ON, mode (+) OFF", than in the other.

The same effect is present when the pumping current is modulated by a *harmonic modulation*. We inject into the pumping current a sinusoidal signal, the frequency and amplitude of the modulation being controllable parameters. The result over the potential symmetry, given by η, is shown in fig.II.16. It is worth noting that here the largest change in η appears for high frequencies and amplitudes of the modulation, while for low amplitudes (< 0.25 mA) the symmetry of the potential does not vary

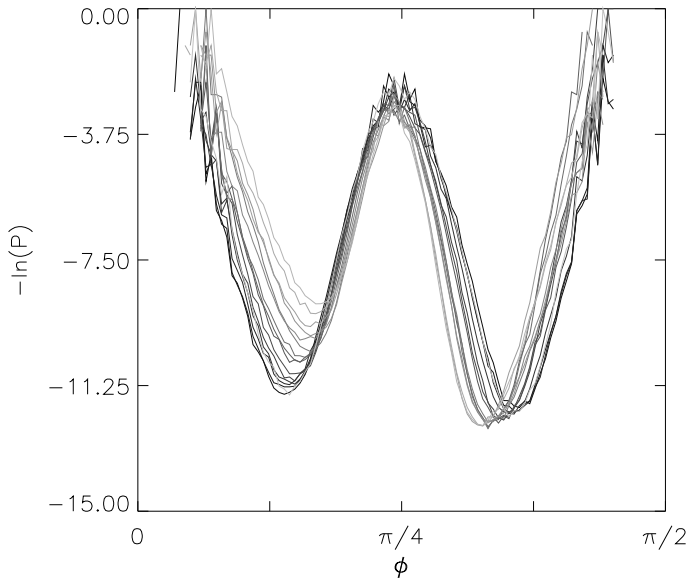

Figure II.15.: Experimental potentials for increasing noise amplitude. The noise strength increases from zero (black curve) to 3 mA RMS (gray curve) as in fig.II.14.

appreciably. While in the following we give an interpretation of the effect of the amplitude of an arbitrary current modulation, we cannot give an exhaustive explanation to the effect of the frequency of the periodic modulation, nor we can exclude that the observed frequency dependence of η in fig.II.16 is not due to some spurious filter effect in the experimental setup (i.e. the amplitude of the modulation would be function of its frequency). However, this measurement will be important in sec.II.5 where we will describe stochastic resonance for our system.

The effect of the amplitude of a symmetrical modulation added to the pumping current over the symmetry of the experimental potential is then similar to a reduction of the DC level of the bias parameter[1]: mode $(-)$ becomes more probable than mode $(+)$. Therefore it is important to check that such effect does not come from the electronics of the setup external to the laser. In fact, it could be possible that some rectifier-like mechanisms could cut the voltage noise shape arriving to the laser, giving rise to an effective non-zero mean modulation of current. Another hypothesis could be the non linearity of the current-voltage curve in diodes which could be invoked to explain the overall decrease of the DC level of the current for high voltage level of noise. Both these mechanisms imply that an increase of voltage applied to the laser (like a spike of the noise giving rise to a positive current pulse) is less efficient than

[1] A similar result was found experimentally and theoretically in [40] observing the total intensity of a mono-mode laser under the action of multiplicative noise in losses.

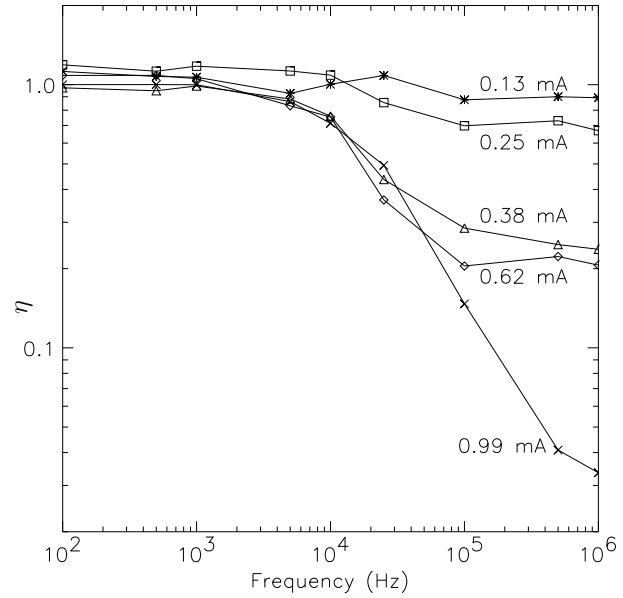

Figure II.16.: The symmetry of potential measured by η as a function of the sinusoidal modulation frequency, for different amplitudes of the signal. Amplitudes below 0.25 mA (rms) do not affect the emission symmetry.

a decrease (like a spike towards low currents). But this would be true for the modal as for the total intensity. Therefore, if this were true, the average value of the total intensity would also decrease with increasing noise.

For current close to the transition region we have therefore measured the signal of total emitted intensity for increasing values of the injected noise, and its probability distribution is shown in fig.II.17 (left). While the standard deviation of the distribution increases with the noise amplitude, the mean value does not change appreciably. This is shown in fig.II.17 (right), where it is visible that the mean value of the distribution does not show a monotone slope towards lower intensities, but remains constant. In order to achieve a difference in the symmetry indicator η of two orders of magnitude as obtained in fig.II.14, the mean value of the DC current should decrease by more than 1 mA (see fig.II.10). On the contrary, as the noise is increased, the observed fluctuations of the mean value of the total intensity correspond to variations of the DC current of the order of 0.01 mA, that therefore cannot explain the change of modal symmetry. Also, the average voltage measured across the diode remains constant for all the used noise intensities. In this way it possible to exclude the previous hypothesis, and the observed behavior becomes a property inherent to the system itself. The multiplicative nature of current fluctuations is a possible explanation.

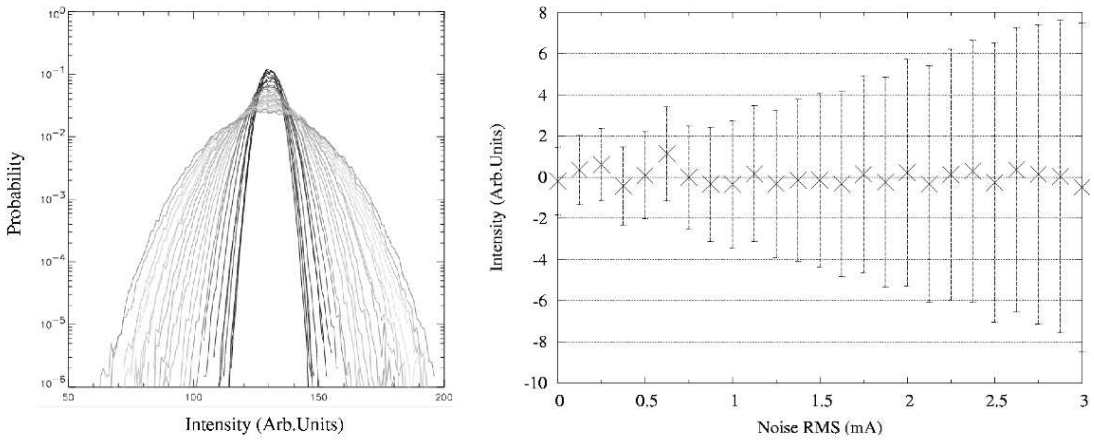

Figure II.17.: *Left:* the normalized probability distribution of the total intensity as a function of noise strength in logarithmic scale. The injected electric noise has zero mean value gaussian shape, and its amplitude increases from 0 mA (black line) to 3 mA RMS (grey line). *Right:* crosses indicate the mean value of the distribution as a function of the noise amplitude, while the standard deviation is shown as error bars.

II.4.2. Multiplicative noise

For systems where the noise enters as a multiplicative term, it can be responsible for new states and behaviors that are not recovered in the noise-free limit [41]. Phenomena like noise sustained spatial structure and noise induced transitions are examples of such richness [42][37]. The most probable states of a system can, in fact, be changed when the noise enters multiplicatively in the mathematical description. We consider the stochastic differential equation of eq.II.5 for a general variable $x(t)$ with time-independent drift $f(x)$ and multiplicative $g(x)$ terms:

$$\frac{dx}{dt} = f(x) + g(x)\xi(t) \tag{II.21}$$

where the white noise source $\xi(t)$ has an amplitude σ given by the correlation $\langle \xi(t)\xi(t') \rangle = \sigma^2 \delta(t - t')$. The function $f(x)$ can be seen as the derivative of a deterministic potential $f(x) = -U'(x)$, whose extrema are the fixed points that should be recovered in the limit of small noise ($\sigma \to 0$). Here the multiplicative term $g(x)$ becomes important, in fact solving the Fokker-Plank equation (eq.II.13) for the complete problem, one finds that the values of the extrema $\bar{x}$ of the stationary probability distribution depend on the amplitude σ of noise. In fact they are found from the

solution of the equation

$$f(\bar{x}) - \frac{\sigma^2}{2} g(\bar{x}) g'(\bar{x}) = 0 \tag{II.22}$$

This means that for non zero values of the multiplicative noise amplitude σ, the solutions (in the sense of the most probable points visited by the system) diverge from the solutions of the deterministic noise-free problem, which are simply given by $f(\bar{x}) = -U'(\bar{x}) = 0$. From the experimental point of view, this may give rise to a change in the symmetry of the system, increasing with noise amplitude. We will in fact take into account the current fluctuations in the experiment as a multiplicative term in the one-dimensional equation.

II.4.3. Expanding the dynamical hypothesis

As we are confident that the effect of current fluctuations over the modal emission symmetry is not due to spurious effects external to the laser, we can try to expand the validity of the one dimensional model of eq.II.20 including current fluctuations. The current parameter J controls the symmetry of the potential, and when J becomes time-dependent we have seen that there is a change in the probability of the modal emission. Therefore if the one dimensional model is correct, this effect can be modeled by a new term proportional to the current fluctuations. When $J \to J_0 + \delta J(t)$ (with $\langle \delta J(t) \rangle = 0$), eq.II.20 should become

$$\dot{\phi} = -U'(\phi, J_0) + g(\phi)\, \delta J(t) + \xi_\phi(t) \tag{II.23}$$

where (as in eq.II.20) $U(\phi, J_0)$ is the deterministic bistable potential (whose symmetry is controlled by the DC current J_0) and $\xi_\phi(t)$ the additive noise along ϕ. The new function $g(\phi)$ has an effect over the system only when $\delta J(t) \neq 0$. When the current is randomly modulated (which can be modeled by an Orstein-Uhlenbeck stochastic process for δJ), eq.II.23 becomes a standard stochastic equation with a multiplicative noise source. As discussed before, multiplicative noise can have important effects over the solutions of the noise-free problem.

From the experimental results presented previously, we can give a characterization of the function $g(\phi)$ as follows. The modulation $\delta J(t)$ has not the same effect over the two potential wells: the modulation is more effective for mode (+) than for mode (−). Equivalently, the potential barrier relative to mode (+) is affected by a current variation more than that of mode (−). Translating this arguments into equation II.23 is equivalent to say that the function $g(\phi)$ has a different symmetry with respect to that of the potential $U(\phi)$. In other words, it should have a higher value in the well close to $\phi = 0$ (mode (+)) than in that close to $\phi = \pi/2$ (mode (−)). This is valid for an arbitrary choice of the modulation: even when the modulation is periodic,

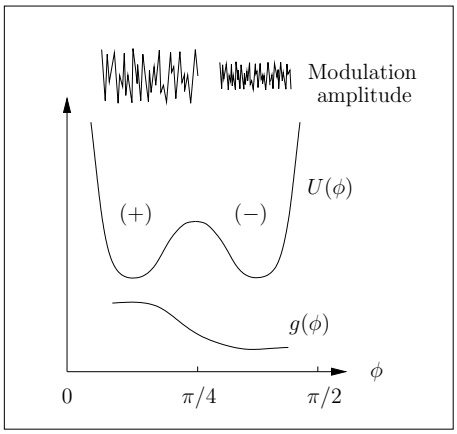

Figure II.18.: Simple scheme of the experimental hypothesis, showing that the multiplicative function $g(\phi)$ should have a different symmetry with respect to the potential $U(\phi)$ and higher value in the well close to $\phi = 0$.

the potential barrier of mode (+) is modulated (periodically) more deeply than that of mode (−), so the internal (additive) noise makes the system escape more often from mode (+) then from mode (−). In fig.II.18 we summarize schematically these ideas, drawing the bistable potential and a possible shape for the function $g(\phi)$ with a different symmetry. The higher value of $g(\phi)$ in the well relative to mode (+) implies there an effective modulation stronger than in the other solution. We will see that this characterization qualitatively well reflects the results of the theoretical one dimensional description of sec.II.6.

II.5. Stochastic Resonance

Stochastic resonance was introduced for the first time in 1981, in order to explain ice ages dynamics [43], but the range of applicability of this new concept quickly increased. It is now for example studied in a variety of fields such as biology and biophysics [44][45] or electronic circuits [46], generally where noise can interact in a non conventional way with signal transmission (for a review article see [43]). Non linear optics, and especially laser physics, had the privilege to give the fist experimental demonstration of stochastic resonance in a real system (a ring laser where bistability occurs between two counter propagating modes [47][48]). Recently, this phenomenon has been found and characterized in the polarization dynamics of vertical cavity semiconductor lasers [32][49] and in edge-emitting semiconductor lasers with optical feedback [50].

The counter intuitive idea of stochastic resonance is that noise can induce order in suitable non-linear systems. In fact the interaction between a bistable system driven by noise and a small periodic modulation[2] can give rise to an enhancement of the coherence of the output response because of the presence of noise. Fixing the frequency and amplitude of the modulation acting over the relative depth of the potential wells, and increasing the noise amplitude from zero, one finds that for a non-zero level of noise the synchronization of the system response with the modulation is optimized. In absence of noise, jumps between the potential wells are not possible because of the choice of sub-threshold periodic modulation amplitude. For very high noise strength, jumps between the two stable points are completely driven by the stochastic force and the synchronization is lost again. Between these two limit behaviors, a noise amplitude exists which can help the periodic modulation to trigger the escape from one solution to the other. In general, this happens when the modulation period T_{mod} becomes equal to $2\,T_k$, where T_k is the intrinsic escape time of the system from one solution (Kramers time [38][39], or average residence time), decreasing function of the noise amplitude. Then the condition

$$T_{mod} = 2\,T_k \tag{II.24}$$

indicates the best synchronization of the system with the modulation, from a statistical point of a view because T_k is a statistical quantity.

Then experimentally is possible to find stochastic resonance in a bistable system either acting over the noise amplitude with fixed modulation frequency, either keeping the noise fixed and varying the deterministic time T_{mod} of the modulation. The

[2] It was demonstrated [51] that the condition of periodicity of the modulation is not necessary, therefore information transmission can be done with a stochastic resonant system.

former is the standard stochastic resonance while the latter is referred to as a "bona fide" resonance [52][32] because the standard frequency analysis, as we will see, cannot reveal the resonant behavior, even if the dynamical principle is for both the same. In the following we will give evidence of both cases found in our system, focusing on modulations around the bistable and symmetric potential. This means that experimentally we fix the parameters in order to have, in absence of current modulations, the symmetry value $\eta = 1$ for the quasi-potential.

II.5.1. Variation of the stochastic time scale

We have shown in sec.II.4.1 that adding an external modulation (noisy or sinusoidal) in the pumping current affects the symmetry of the modal dynamics. This effect is not taken into account in the standard stochastic resonance treatment, where noise acting over the system is additive and it cannot change the symmetry of the potential. Due to this fact, we have to find a way to change the stochastic time scale T_k without injecting noise into the pumping current. On the other hand this effect of the current modulation can be used to study stochastic resonance with multiplicative noise, as we will describe further in sec.II.5.4.

In order to tune the stochastic time-scale, we move the system in the space of parameters (J, T_{sub}) of fig.II.5 choosing a path that preserves the symmetrical modal emission. We plot in the inset of fig.II.19 the path in the plane (J, T_{sub}) corresponding to the symmetrical emission $\eta = 1$. Evidently, these points are found in the middle of the transition region, so the shape of the curve is the same. Along this path we measure the average resident times of the two modes, and the result is plotted in fig.II.19 as a function of the temperature. As it appears, the value of the average residence time (equal for both modes because of the choice $\eta = 1$) depends on the point (J, T_{sub}) where the system is kept in the parameter plane. This average time varies by many orders of magnitude moving along the path at $\eta = 1$. We refer to this path as Γ_1, and we remark the existence of two branches (Γ_1^a and Γ_1^b) along which the average residence time $\overline{T}$ varies monotonically with temperature T_{sub}.

The structure of the curve of fig.II.19 is related to the modal stability as a function of the parameters, and a very refined theoretical treatment taking into account microscopic effects in semiconductors would be necessary to explain the observed behavior. The development of such a complete model is well beyond the aim of this work, where we just take advantage of the relatively regular shape of the mean residence times in the space of parameters for this device.

Therefore, changing the two parameters J and T_{sub}, allows to vary the stochastic time-scale T_k of the hopping maintaining the symmetry of the potential constant. Then modulating periodically the relative depth of the potential wells with a fixed

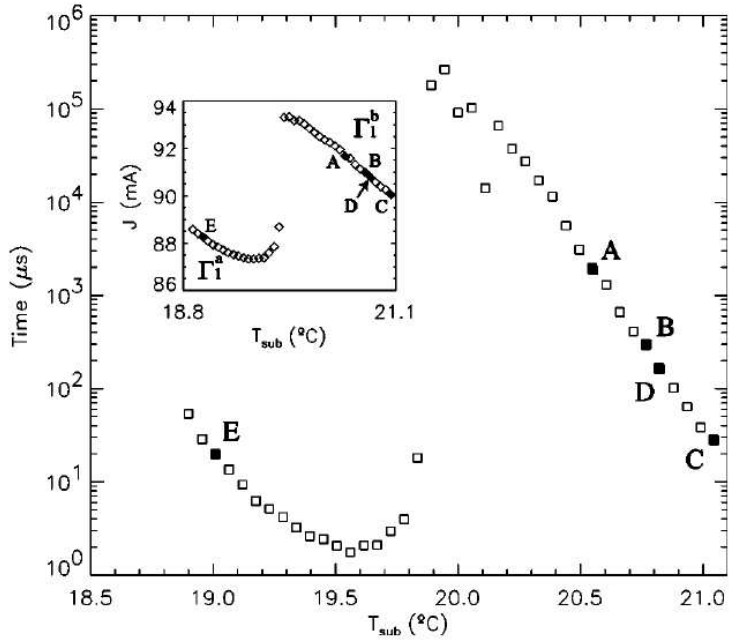

Figure II.19.: Average residence time $\overline{T}$ for the two modes as a function of the substrate temperature along the path Γ_1. Inset: the path Γ_1 in the parameter space (T_{sub},J) found in order to maintain the emission symmetry ($\eta = 1$). Points A,B,C and D will be used in sec.II.5.2 and II.5.3.

period T_{mod}, it is in principle possible to fulfill the condition $T_{mod} = 2\,T_k$ and observe stochastic resonance.

II.5.1.1. Checking the sub-threshold periodic modulation

Stochastic resonance is induced by a subthreshold (periodic) signal amplitude. This means that, in absence of noise, the external force is unable to induce synchronized jumps between the two wells. In our system we cannot eliminate the internal noise, so this condition on the modulation amplitudes A_{mod} added to the pumping current has been verified using an alternative method. We have checked that, at frequencies $\nu_{mod} = 1/T_{mod}$ much lower than the Kramers rates T_k^{-1}, the amplitudes A_{mod} used are small enough in order not to have significant interaction between modulation and modal behavior. This means that the hopping statistics of the modulated system at $\nu_{mod} \ll T_k^{-1}$ are very similar to the ones of the unforced system: the residence time probability distributions remain exponentially decaying functions with the same Kramers rates. In this way the periodic modulation alone should not be able to drive the system from one solution to the other and could be considered small.

A second important requirement is that the modulation amplitude A_{mod} should not modify the symmetry of the experimental potential because of the multiplicative nature of the bias parameter. As it was shown in fig.II.16, we observe that the symmetry η remains unaffected, in the whole experimental frequency range, if the amplitude A_{mod} is lower than 0.25 mA. For the studied transition, this condition on the modulation amplitude is more restrictive than the condition for subthreshold excitation discussed above. Then, in practice, when modulating the system, if η remains unchanged for the used frequencies, both conditions are verified.

II.5.2. Experimental results: Stochastic Resonance

The experimental set up used in the following is the same described in sec.II.1. We investigate the response of the system applying a sinusoidal modulation with a subthreshold amplitude at a period T_{mod}. Then we vary the average mode-hopping duration $\overline{T}$ by changing the parameters according to the path Γ_1. In the following, we will refer to the parameters used in the experiment indicating the value of T_{sub} ; the corresponding value of J and $\overline{T}$ can be induced from fig.II.19. Choosing T_{mod} compatible with the hopping time scales described in fig.II.19, the temporal behavior of a modal intensity is shown for the branch Γ_1^b in fig.II.20. For a different T_{mod}, a similar response is found along the branch Γ_1^a. If T_{mod} is chosen such that it is compatible with the time scales of both branches, then a double resonance can be found by increasing T_{sub} along Γ_1.

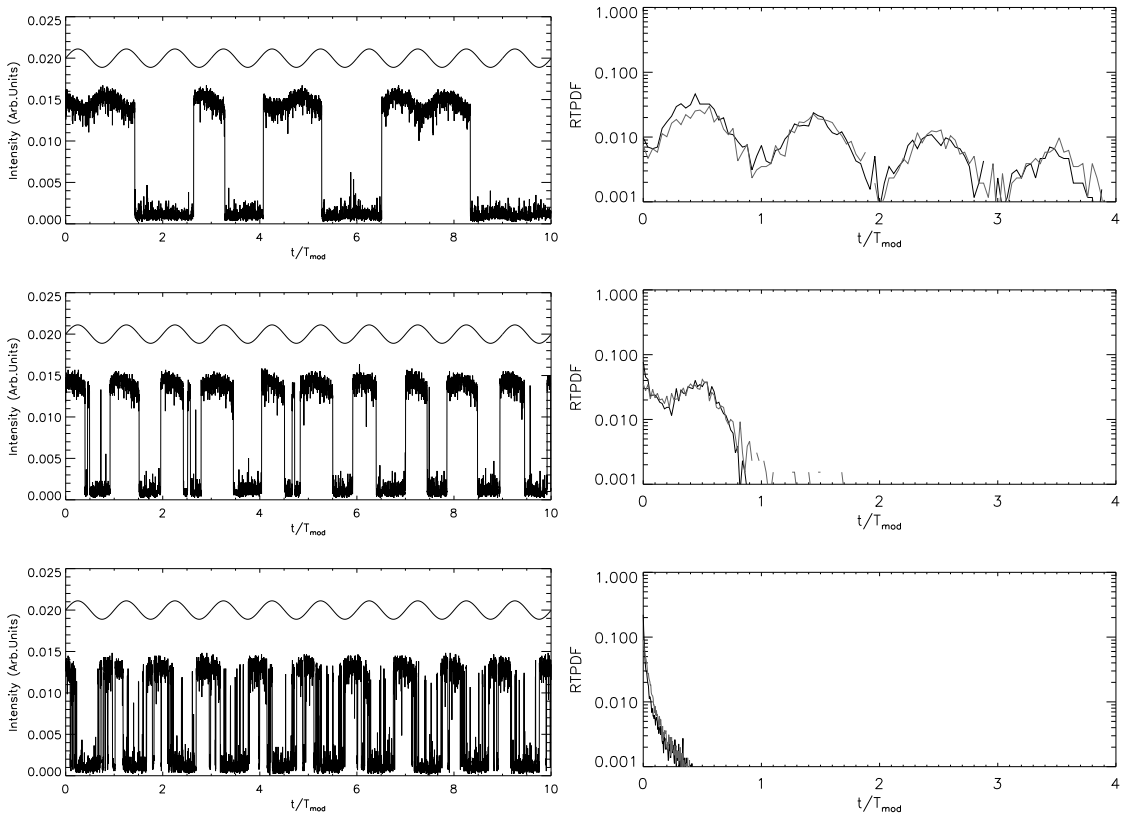

Figure II.20.: *Left:* modal intensity time series for different parameter values. The time base is normalized to the modulation period. From top to bottom the parameters correspond to the points marked in fig.II.19 respectively by A (where $\overline{T} \simeq 2$ ms), B ($\overline{T} \simeq 300$ μs) and C ($\overline{T} \simeq 30$ μs), in the branch Γ_1^b. The period of the modulation is 500 μs (2 kHz), while its amplitude is 0.25 mA (rms). *Right:* Corresponding residence time probability distribution functions (RTPD). The black [gray] trace is relative to mode $(-)$ $[(+)]$.

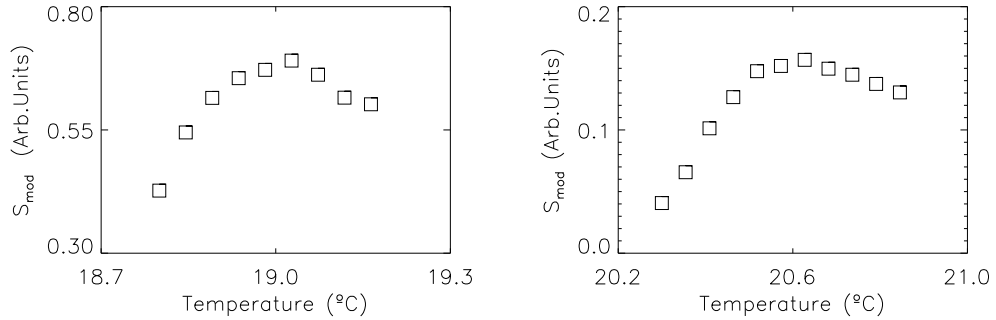

Figure II.21.: Height of the peak at the modulation frequency in the modal intensity power spectrum as a function of the position along Γ_1, expressed by the laser substrate temperature. The corresponding pumping current can be obtained by fig.II.19. *Left:* moving along Γ_1^a, with a modulation in the pumping current of 40 kHz and an amplitude of 0.30 mA rms. *Right:* moving along the branch Γ_1^b with a modulation of 2 kHz and an amplitude of 0.25 mA rms.

Analyzing the modal time series (fig.II.20 left column, from bottom to top), we observe that, if $2\overline{T} < T_{mod}$, the system exhibits random-mode hops not synchronized with the forcing. If $2\overline{T} \approx T_{mod}$, the mode hopping occurs synchronously with the modulation and a maximum of coherence in the modal signal is found. Finally, for $2\overline{T} > T_{mod}$, mode hopping does not occur anymore at every half-period of the forcing and synchronization may be present but only for time windows lasting few modulation periods.

A quantitative description of the resonance can be extracted from the measured power spectrum of each mode. For each value of $\overline{T}$ the magnitude of the component in the modal signal at the frequency of the modulation is found. The result is shown in fig.II.21, where we plot the response along the branch Γ_1^a (left) and Γ_1^b (right). A clear maximum can be noticed in both cases when the resonance condition $T_{mod} = 2\overline{T}$ is fulfilled. This is a clear evidence of stochastic resonance, obtained by proper tuning of the stochastic time scale of the system to the external modulation period.

Another useful analysis of the observed behavior can be performed by considering the residence times T of a mode and perform the corresponding statistics [25]. In fig.II.20 (right column), we plot the residence time probability distributions (RTPD) extracted from the corresponding time series, evaluated for both modes. For $2\overline{T} < T_{mod}$ (lower row) the RTPDs are exponentially decaying functions, as a consequence of the random hopping inside a period of the modulation. For $2\overline{T} > T_{mod}$ (upper row), the RTPDs exhibit several peaks corresponding to odd multiple of $T_{mod}/2$, indicating that the hopping is not synchronous with the modulation but it may occur after few

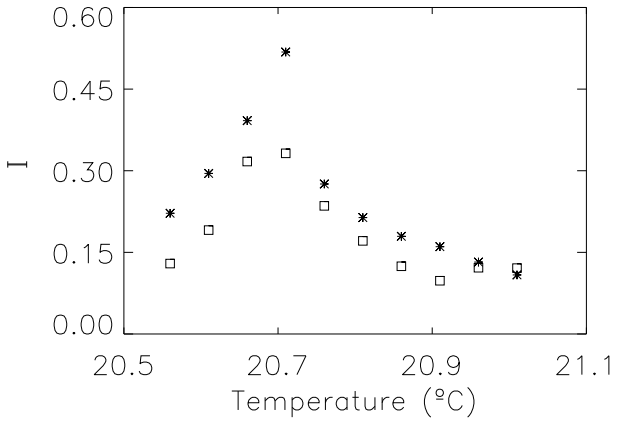

Figure II.22.: Indicator I as a function of the position along Γ_1, expressed by the laser substrate temperature. Squares are relative to mode $(-)$, stars to mode $(+)$. Modulation characteristics are as in fig.II.21.

modulation periods. Finally, for $2\overline{T} \simeq T_{mod}$ (central row) the RTPDs present a single peak centered at half of the external period, showing that most of the residence times are comparable with half of the modulation period and a statistical synchronization is present.

In order to quantify the resonance in this context, an indicator has been introduced measuring the excess of jumps synchronized to the forcing with respect to the jumps distribution without modulation [52][32]. This is done by integrating the probability distributions of the resident time (in fig.II.20, right column) in a small interval around $T/T_{mod} = 1/2$. All the events whose residence time is in this interval are considered synchronized with the external modulation. The definition of the indicator is

$$I = \int_{T_{mod}/2-\beta T_{mod}}^{T_{mod}/2-\beta T_{mod}} \tilde{P}(T)dT \tag{II.25}$$

where $\tilde{P}(T)$ is the residence time probability distribution of the modulated system (with subtraction of the background distribution found in absence of the modulation), and $\beta = 1/4$ defines the width of the integration region. In fig.II.22 we plot, for both modes, I as a function of the position of the system along the parameter path Γ_1^b. The presence of a maximum of I when $2\overline{T} \approx T_{mod}$ is a further indication of the occurrence of stochastic resonance.

II.5.3. Experimental results: Bona Fide Resonance

Keeping fixed the stochastic time scale $\overline{T}$ of the mode hopping and varying the modulation period T_{mod} it is possible to observe a resonant behavior in the response of the system. In this way, the condition of synchronization between the two time scales

is reached taking the period T_{mod} as a parameter. This alternative way of evidencing stochastic resonance is referred as *bona-fide* resonance and was introduced in [52].

Even if stochastic and bona fide resonance evidently rely on the same dynamical principles, while the frequency analysis of conventional stochastic resonance (as in fig.II.21) reveals a resonant response of the system around a certain value of the noise amplitude, for "bona fide" resonance this does not appear. This is due to the fact that the spectral component of the output signal at the forcing frequency, suffers no degradation at low frequencies, so a clear peak is not visible in the curve. In fig.II.23 three time traces are shown for different values of the modulating frequency, while the amplitude is kept fixed at a sub-threshold value (0.25 mA rms). The time base is normalized to the modulation period. Increasing the forcing frequency (from bottom to top) the response of the system passes trough a synchronized behavior with the external modulation (central panel). For low frequencies (lower panel) this synchronization is broken by events appearing inside a period of the injected signal; anyway the spectral component at the modulation frequency is not decreased. This happens instead for high frequencies (upper panel) where jumps between modes cannot follow the rapid modulation. In fig.II.24 the frequency response of the system is shown: as discussed no resonance can be detected, and the experimental points can be fitted with a single-pole response function of the form

$$F(\nu) = \frac{A_o}{\sqrt{1 + (\nu/\nu_o)^2}} \tag{II.26}$$

where $A_o = 0.21$ and the cut frequency $\nu_o = 28$ kHz for branch Γ_1^a (left), while $A_o = 0.34$ and $\nu_o = 3.8$ kHz for branch Γ_1^b (right). The cut off frequency corresponds to the resonant response, as can be detected by analyzing the temporal traces.

The integral indicator I defined in eq.II.25 was introduced in [52] in order to overcome this problem. Even if this kind of resonance is not visible in a standard frequency analysis, it exists and it is detectable if one takes the resident time as observable. This is the reason of the name *bona fide* given to this resonance. For our system the indicator I as a function of the forcing frequency is given in fig.II.25. When the system is prepared at the point E of branch Γ_1^a (see fig.II.19), the stochastic time scale is around $\overline{T} \approx 20\mu$s , so the resonance is expected at the frequency $(2\overline{T})^{-1} \approx 25$ kHz. When the system is prepared at the point D in the branch Γ_1^b (where $\overline{T} \approx 160\mu$s) the resonance is expected at $(2\overline{T})^{-1} \approx 3.1$ kHz. The two curves of the indicator as a function of the driving frequency, shown in fig.II.25, have maxima around these expected values. This gives evidence of the occurrence of bona fide resonance. The difference between the curves of the two modes is due to the experimental imprecision in the setting of parameters in order to obtain the modal symmetry ($\eta = 1$).

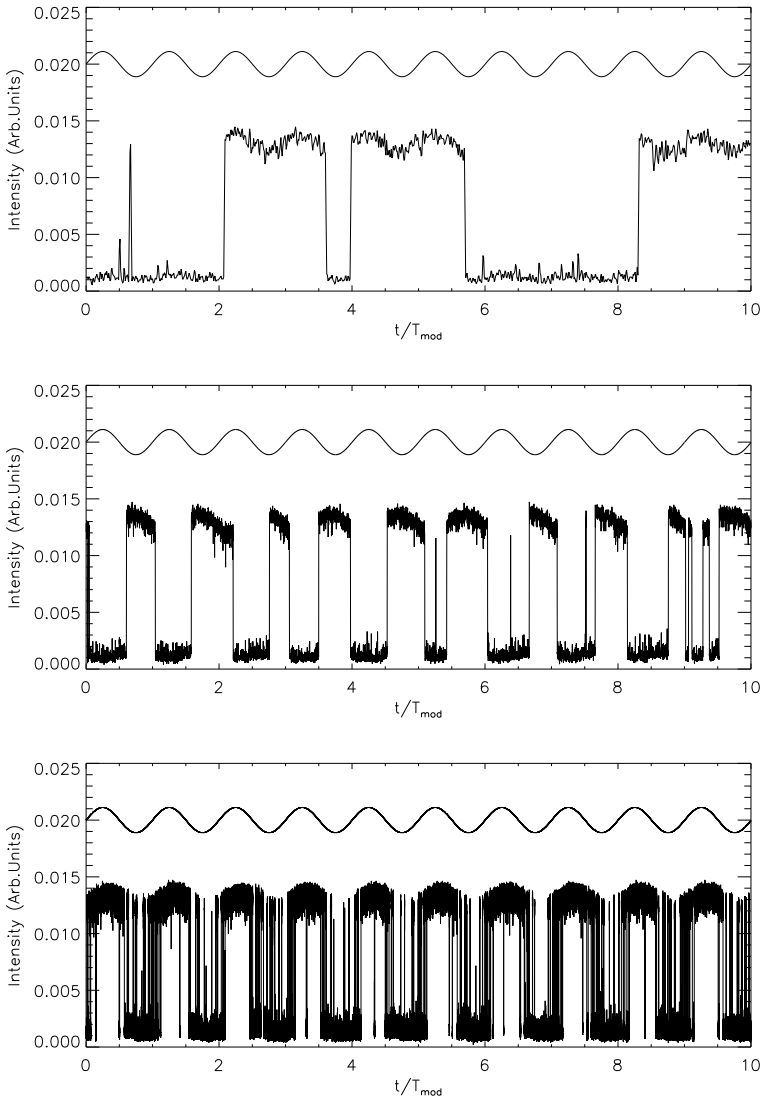

Figure II.23.: Modal intensity time series for different modulation frequencies at the temperature $T_{sub} = 20.5^oC$, corresponding to point D of fig.II.19. From top to bottom: 20 kHz, 2 kHz, 0.1 kHz. The amplitude of the modulation is 0.25 mA (rms). Since at point D one obtains $\overline{T} \approx 160\mu$s, the resonant frequency is $(2\overline{T})^{-1} \approx 3.1$ kHz.

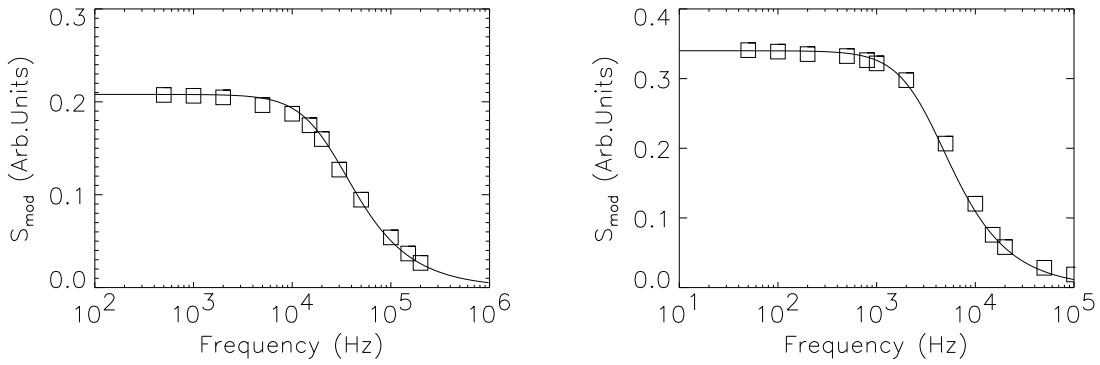

Figure II.24.: Height of the peak at the modulation frequency in the modal power spectrum, as a function of the modulation frequency. In the left panel the system is prepared at the point E (for which $\overline{T} \approx 20\mu$s, $(2\overline{T}^{-1}) = 25$ KHz) of branch Γ_1^a plotted in fig.II.19. In the right panel the system parameters correspond to the point D (for which $\overline{T} \approx 160\mu$s, $(2\overline{T})^{-1} =$ 3.1 KHz) of branch Γ_1^b. Experimental points (squares) are fitted with single-pole response functions (lines), see eq.II.26.

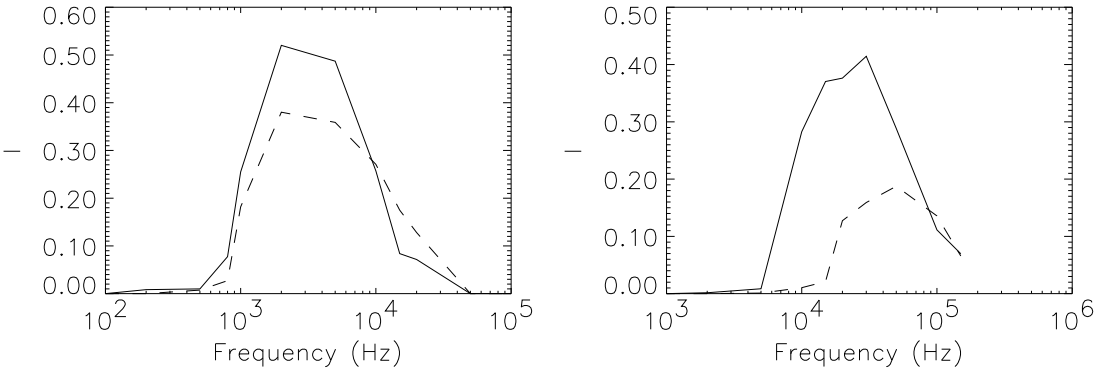

Figure II.25.: Indicator I as a function of the modulation frequencies. In the left panel the system parameters correspond to the point E of fig.II.19, in the right panel they correspond to point D. Dashed lines are relative for mode $(-)$, solid lines for mode $(+)$.

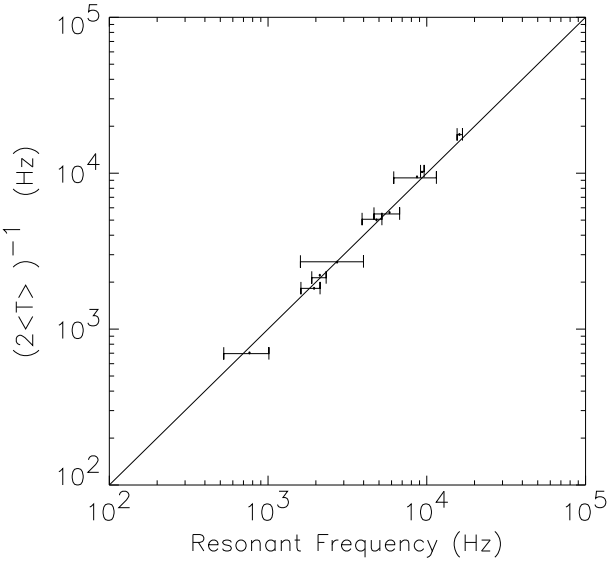

Figure II.26.: *Bona fide* resonance. The expected resonant frequency ($(2\overline{T})^{-1}$) (measured removing the modulation) plotted as a function of the frequency of the modulation that maximizes the indicator I (calculated on the intensity of mode $(-)$, but a similar curve holds for mode $(+)$).

We have also verified that bona fide resonance can be found all along the path Γ_1 in the parameter space. Preparing the system in different points on Γ_1, i.e. fixing the stochastic time scale $\overline{T}$, we have found the relative resonant frequency of the external modulation. In fig.II.26 it is shown that the value of the resonant frequencies are (within the experimental error) equal to the expected resonance frequencies $(2\overline{T})^{-1}$, where the average resident time $\overline{T}$ was measured for the same parameters in absence of the external modulation.

II.5.4. Stochastic resonance with multiplicative noise

We want to show here to show that stochastic resonance is possible adding noise on the bias current of the laser. We have seen that conventional stochastic resonance does not take into account the symmetry dependence of the potential over the noise amplitude. The standard theory is developed with white or colored gaussian additive noise, while more recent studies focused on the interplay between additive and multiplicative noise as in [53][54]. In these works two independent sources of noise are present: a multiplicative noise creates new states for the system, and an additive one makes the system jump between them. In [54] the effect of the multiplicative noise term is to change the relative stability of the two stable points of the system (strongly asymmetric in absence of multiplicative noise), and restore the symmetry of the resi-

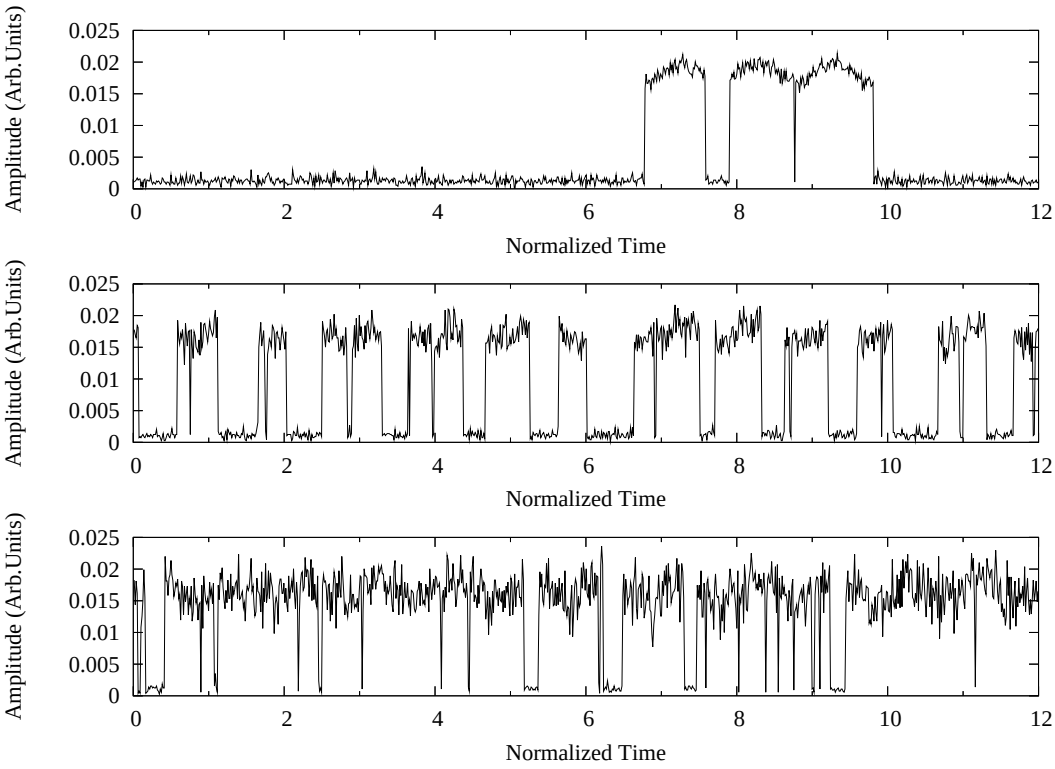

Figure II.27.: Temporal traces of mode (−) intensity for increasing amplitude of injected noise (from top to bottom: 0 mA, 2.4 mA, 4.8 mA (rms)). The time scale is normalized to the small external modulation period (with frequency of 320 Hz and amplitude 0.25 mA (rms)).

dence times. Then stochastic resonance is found for an optimum non-zero level of the additive noise, which does not affect the symmetry of the problem. They demonstrate theoretically this mechanism in a FitzHugh-Nagumo system and experimentally in a purpose-built electronic circuit.

In our system we can identify the source of additive noise as the spontaneous emission of the laser. This is fixed once the system is maintained stable in a point of the parameters space. We have seen in fact that the average residence time $\overline{T}$ of each mode depends on the position of the system in the space of parameters (J,T_{sub}). On the other hand, according to the dynamical characterization discussed above, the noise injected into the bias current acts, at least partially, as a multiplicative source, and this affects the symmetry of the potential. Because of our definition (see eq.II.4 and fig.II.14), the effect of noise is to reduce the value of η (the effect on the symmetry is similar to a reduction of the DC current). So it is possible for the multiplicative part to restore the symmetry to $\eta = 1$ if, in its absence, the emission was asymmetric with $\eta > 1$. Once the symmetry is restored, synchronization will be possible with

a suitable periodic modulation whose frequency is "resonant" at that total level of noise, given by spontaneous emission and current fluctuations. Then for higher noise amplitudes the symmetry and the synchronization is lost again with $\eta < 1$.

Therefore we modulate the pumping current with a subthreshold periodic signal at a frequency of 320 Hz, so $T_{mod}/2 = 1.6$ ms should be the Kramers time of the forced system in order to find stochastic resonance. We prepare the system increasing suitably the DC current (by a value that depends on T_{mod} chosen) from the symmetric point inducing a strong asymmetry in the potential ($\eta \approx 10$), and we increase the current noise amplitude. The experimental temporal traces (mode $(-)$ intensity) are shown in fig.II.27. In the upper panel noise is absent, and it is clear that mode $(+)$ prevails over mode $(-)$ and that the periodic modulation cannot be followed by the mode hopping, because of the asymmetry and because the large difference between the time scales ($2\overline{T} \gg T_{mod}$). Increasing the injected noise, the symmetry of the potential changes (η decreases), and the system passes trough a resonant region (central panel) for intermediate values of noise. Here $\eta \simeq 1$ and the hopping can be triggered by the modulation ($2\overline{T} \simeq T_{mod}$). For higher noise amplitudes then (lower panel), the potential is taken away from symmetry again, but from the other side with respect to the noise free limit: η becomes lower than unity ($\eta \approx 1/10$) and the hopping cannot follow the external modulation because $2\overline{T} \ll T_{mod}$ and because of the strong asymmetry.

The results are resumed in fig.II.28. In the upper panel the values of η as a function of the injected noise strength show the large variation of the symmetry due to the multiplicative source. In the central panel we calculate from each time series the integral indicator defined in eq.II.25, and in the lower panel the spectral analysis discussed in sec.II.5.3 is performed. It is clear that a maximum of these two last quantities, indicating stochastic resonance, is found for the noise level where the symmetry of the potential is restored. The amplitude of the noise source of our system acts as a symmetry parameter. When multiplicative noise has restored the symmetry, then multiplicative and additive noises make the system to respond coherently to the external modulation. This demonstrates that in our system stochastic resonance can be found acting on the multiplicative source of noise.

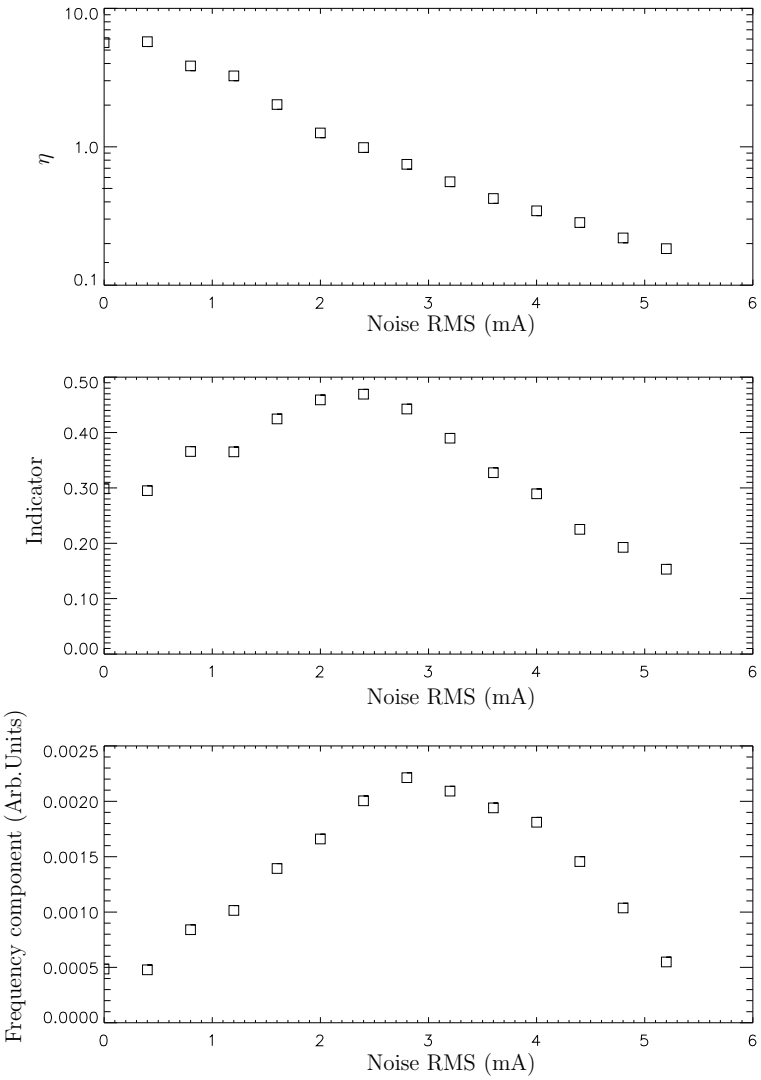

Figure II.28.: *Upper panel:* The symmetry indicator η defined in eq.II.4 as a function of the noise amplitude. The system is suitably prepared, in absence of noise, in a strongly asymmetric state, than noise injected into the current changes the symmetry. *Central panel:* the coherence indicator I, defined in eq.II.25, as a function of the noise amplitude. *Lower panel:* height of the peak at the modulation frequency in the power spectrum as a function of the noise amplitude.

II.6. Model

This section should be considered an overview of the theoretical work done mainly by S.Balle (Imedea, Spain), G.Giacomelli and S.Lepri (CNR, Italy). The tight collaboration with our experimental group at INLN was for me a very interesting and fruitful experience, as ideas from both fields improved globally the work, giving theoretical basis to the ideas and hypothesis we could formulate from the experimental exploration.

In this section we describe the theoretical model that can qualitatively explain the experimental results presented above. Starting from a standard set of rate equations describing the field of the two modes and carriers in the laser, it is possible to reduce the problem to just one dimensional Langevin equation under some hypothesis over the modal gains, and after having eliminated the carriers and total intensity dynamics. This is justified by the fact that the time scale we are interested in, i.e. the hopping of the significant variable $\phi(t)$ as it was defined in the experiment in sec.II.3.5, it is long enough ($\approx \mu$s) to neglect transient effects and relaxation oscillations ($\approx$ ns). Under these assumptions, we will deduce the potential that drives the deterministic part of the dynamics, while spontaneous emission provides a Langevin force of additive noise. The effects of a modulation of the bias current are taken into account in the reduced model. When the current parameter becomes a fluctuating quantity, a new multiplicative term appears in the Langevin equation, proportional to these fluctuations. This results in a change of the potential symmetry due to current fluctuations, in good agreement with the experimental evidences.

II.6.1. Reference Model

The starting point of the theoretical analysis is a stochastic rate equation model for semiconductor lasers that may operate in two longitudinal modes. The standard laser theory developed by Lamb et al. in [55] states the reference model for such dynamics, and we will build rate equations starting from this. This is a *ab initio* treatment, which starts directly from Maxwell equations, finds the polarization of the medium in the optical cavity by means of quantum treatment of the density matrix, and writes the equation of movement for the slowly varying field amplitude for the general multimode case. When two modes are considered the model becomes

$$\dot{E}_1 = E_1(a_1 - \beta_1 I_1 - \theta_{12} I_2) \tag{II.27}$$

$$\dot{E}_2 = E_2(a_2 - \beta_2 I_2 - \theta_{21} I_1) \tag{II.28}$$

where β_1 and β_2 are the self saturation coefficients, θ_{12} and θ_{21} give cross saturation and $I_{1,2}$ are the dimensionless intensities of the two modes. The gains are expressed by

the terms $a_{1,2}$, which have a Lorentzian shape as a function of the detuning between field and atomic resonance.

Different dynamical scenarios can be found from these rate equations according to the sign of the coupling factor C defined as the ratio between cross and self saturation terms:

$$C = \frac{\theta_{12}\,\theta_{21}}{\beta_1\,\beta_2} \tag{II.29}$$

In the strong coupling regime ($C > 1$), which is the relevant case in our system, it is found that the two single mode solutions ($[E_1 \neq 0,\ E_2 = 0]$ and $[E_1 = 0,\ E_2 \neq 0]$) can coexist. The final state depends on the initial conditions and in presence of noise mode hopping can appear. For our system we will include in this model an expression for the carriers dynamics and for the modal gain as a function of the carriers. We will change slightly the expression for the self and cross saturation, but these two main ingredients will remain.

II.6.2. Rate equations

A complete physical modeling of the complex mechanisms taking part in the laser structure is beyond the aim of this work. We want to concentrate the attention on the dynamics of the laser in the mode-hopping regime, and give a simple characterization in dynamical terms of the role of the parameters. The first step is writing the rate equations for the slowly varying complex envelope of the electric field E_- and E_+ of two longitudinal modes. Both modes interact with the same carrier density N which provides the necessary gain. Writing the pumping current as a generic function of time $J(t)$, normalizing the time with respect to the cavity decay time (of the order of 10 ps) and considering the stochastic equations in Itô sense [35] the complete model can be written as

$$\dot{E}_+ = \frac{1}{2}[(1+i\alpha)g_+ - 1]E_+ + \sqrt{2D_{sp}N}\,\xi_+ \tag{II.30}$$

$$\dot{E}_- = \frac{1}{2}[(1+i\alpha)g_- - 1]E_- + \sqrt{2D_{sp}N}\,\xi_- \tag{II.31}$$

$$\dot{N} = \gamma[J(t) - N - g_+|E_+|^2 - g_-|E_-|^2] \tag{II.32}$$

The decay time of carriers is about 1 ns, and it is taken into account by $\gamma = 0.01$.

The dispersive effects that are always present in semiconductors, even at the frequency of the gain maximum, are included through the linewidth enhancement factor α (or Henry's factor [56]). From a dynamical point of view, α couples the amplitude variations of the field with its phase variations. Any deviation of the intensity from its stationary value will result in (damped) oscillations ΔN in the carrier number around

its stationary point. A non-zero value of α will then cause a frequency shift proportional to $\alpha\Delta N$. In this way, amplitude variations give rise to frequency variations. However, as it will be shown in the following, we are interested just in the dynamics of the modal amplitudes, which are not affected by phase variations, then α becomes irrelevant in our treatment.

As already mentioned, the polarization dynamics in VCSELs [57][26] has many similarities with mode-hopping in longitudinal modes of bulk lasers. Rate equations similar to eq.II.30-II.32 have been used to analyze polarization switching and hopping in VCSELs. On one hand, switching between the two modes, in absence of bistability, is found if the modal gains $g_\pm$ can change, above threshold, by increasing the current. In this way the authors model the thermal effects in the active area, by a different dependence of the gain on current J for the two modes. On the other hand, bistability (and so mode-hopping) is found only if saturation terms are inserted in the expression of the gains. In our system, as we never observe switching between the two modes without bistability, then saturation terms are necessary and will be introduced. The frequency profile of the modal gains is not taken into account, so the two modes are to be considered very close to the maximum of the gain curve. In this approximation the gain $g_\pm$ of each mode is assumed a linear function of N.

The symmetry of eq.II.30-II.32 with respect to the exchange of the fields $E_+ \leftrightarrow E_-$ should be altered in order to recover the experimental observations: mode $(-)$ is active at threshold and a transition to mode $(+)$ appears above threshold, involving bistability between them. Therefore we introduce phenomenologically a small asymmetry between the two linear gains of the modes: $g^{\,l}_{\pm} = N \pm \varepsilon(N - N_c)$, where ε determines the difference between the differential gains and N_c defines the carrier density where these unsaturated linear gains intersect. In this way we model, by means of ε, all the possible gain asymmetries between the two modes, simply by a small asymmetry in their linear gains ($\varepsilon > 0$, $\varepsilon \simeq 0$). Saturation is then included in the expression of the gain, as it is the case in the classical approach of sec.II.6.1, by a self ($s > 0$) and a cross ($c > 0$) saturation term. The complete modal gains then read

$$g_\pm = \frac{N \pm \varepsilon(N - N_c)}{1 + s|E_\pm|^2 + c|E_\mp|^2} \tag{II.33}$$

In this model, because of the presence of saturation (necessary to have bistability), carriers are not clamped above threshold. This means that an increase of the current gives rise always to a (small) increase of N even above threshold, and this makes possible the modal switching. In fact, due to the asymmetry ε, an increase of the current J (giving an increase of N) produces a change of the sign of the difference between the two gains $g_\pm(N)$ (for $N > N_c$). The switching occurs without taking into account the dependence of the modal gains directly on the current, because carriers

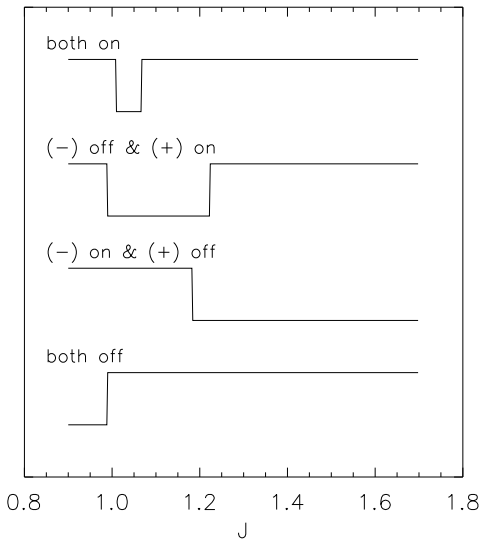

Figure II.29.: Linear stability analysis for the solutions of the model eq.II.30-II.32 as a function of the current J. The stable solutions are expressed by a "low" index when stable, otherwise they are unstable.

are not clamped above threshold. Then, in the bistability region mode hopping may occur, because of the high modal coupling ($c > s$) and of the presence of spontaneous emission noise. Therefore the small asymmetry ε together with saturation in the modal gains, reproduce phenomenologically the observed transition from mode $(-)$ to mode $(+)$ and mode hopping.

The model is then appropriate for transitions between two consecutive longitudinal modes of the spectrum. A more detailed physical description of the gain suppression mechanisms among modes would be necessary to explain the transitions between modes that are not contiguous, as experimentally observed in sec.II.2 for high currents. However the general dynamical behavior displayed by the real system in all these transitions is recovered in the model and in its reduction to a single stochastic differential equation.

Spontaneous emission in each mode has to be inserted phenomenologically, because the semiclassical approach cannot describe quantum fluctuations. The strength of spontaneous emission is controlled by the term D_{sp} multiplying two stochastic sources $\xi_{\pm}$ for the two modes. These are two independent complex white noise processes with zero mean and unit variance

$$\langle \xi_{\pm}(t) \rangle = 0 \tag{II.34}$$

$$\langle \xi_i(t) \xi_j^*(t') \rangle = \delta_{ij} \delta(t - t') \tag{II.35}$$

The deterministic version of eqs.II.30-II.32 admits four different solutions: the

trivial solution [$E_\pm = 0$], two single mode solutions [$E_- = 0$, $E_+ \neq 0$] [$E_- \neq 0$, $E_+ = 0$], and a solution where both modes are lasing [$E_\pm \neq 0$]. The trivial solution [$E_\pm = 0$] is the only stable solution for current $J < \min(J_-, J_+)$, where

$$J_\pm = \frac{1 \pm \varepsilon N_c}{1 \pm \varepsilon} \tag{II.36}$$

For definiteness, we consider $N_c > 1$, then $J_- < 1 < J_+$ and J_- has to be considered the laser threshold. When the bias current is increased from zero the solution [$E_\pm = 0$] looses stability for $J = J_-$ and the system switches to the first mono-mode solution [$E_- \neq 0$, $E_+ = 0$]. Upon further increasing of the bias current J, the sequence of bifurcations depends strongly on the choice of the parameters s, c and N_c. For $c > s$ (strong coupling) this first mono-mode solution may coexist with the other [$E_- = 0$, $E_+ \neq 0$], or even with the solution [$E_\pm \neq 0$] (in this case only within a small current range). Finally, for higher current the solution [$E_- = 0$, $E_+ \neq 0$] prevails.

In fig.II.29 the stability analysis of the solutions is shown for the parameters $\varepsilon = 0.1$, $s = 0.98$, $c = 1.3$, $N_c = 1.1$, $\gamma = 0.01$. Each solution is stable when the corresponding index is lower, unstable when it is higher. Below threshold the only stable solution is the zero solution, then it is visible that there exists a range for the current around $J = 1.2$ where bistability exists between the two single mode solutions.

II.6.3. Reduction to one dimensional model

In the following we want to introduce the suitable transformations and conditions in order to reduce the rate equations model in eqs.II.30-II.32 to an effective 1D bistable system. We start by introducing the amplitude-phase coordinates for each mode

$$E_\pm = \rho_\pm \exp(i\psi_\pm) \tag{II.37}$$

From eqs.II.30-II.32, using standard transformations [35], it is possible to obtain the new set of rate equations

$$\dot{\rho}_\pm = \frac{1}{2}\left[g_\pm - 1 + \frac{2D_{sp}N}{\rho_\pm^2}\right]\rho_\pm + \sqrt{2D_{sp}N}\,\xi_\rho^\pm \tag{II.38}$$

$$\dot{\psi}_\pm = \frac{\alpha}{2}\,g_\pm + \sqrt{2D_{sp}N}\,\xi_\psi^\pm \tag{II.39}$$

$$\dot{N} = \gamma\left[J(t) - N - g_+\rho_+^2 - g_-\rho_-^2\right] \tag{II.40}$$

Since the modal phases $\psi_\pm(t)$ do not appear in the equations of $\dot{\rho}_\pm$ and $\dot{N}$, they do not influence the evolution of the modal amplitudes and carrier density and we can disregard them without loss of generality.

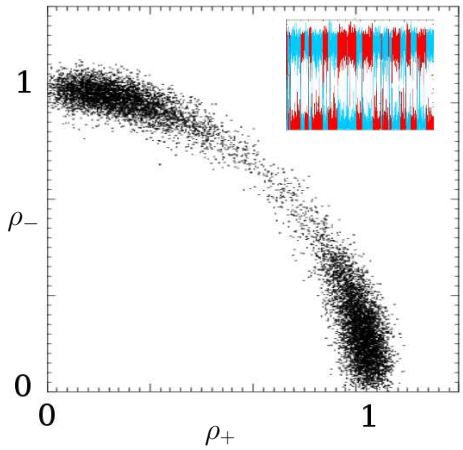

Figure II.30.: The mode hopping regime as it appears in the plane (ρ_+, ρ_-) (here normalized to the mean total intensity) from the simulation of the complete model. In the inset the corresponding time traces are shown. The parameters are $\varepsilon = 0.1$, $s = 1.0$, $c = 1.3$, $N_c = 1.1$, $\gamma = 1.1$, $J = 1.197$, $D_{sp} = 7\,10^{-6}$.

It is convenient to perform the change to "cylindrical" coordinates, as we have done for the experimental data in sec.II.3.5, introducing two new variables $(r(t)\,, \phi(t))$:

$$\rho_+ = r\cos\phi \qquad \rho_- = r\sin\phi \tag{II.41}$$

In these new variables, r^2 is the total intensity emitted by the laser and ϕ determines how this power is partitioned among the two modes. When $\phi = 0$ the emission is carried out by mode $(+)$, the one active at high current which corresponds to the one with longer wavelength in the experiment, while for $\phi = \pi/2$ mode $(-)$, the one active at the laser threshold with the shorter wavelength, is active. Between these two points, intermediate values of ϕ give different power to each mode.

The space (ρ_+, ρ_-), normalized to the average total intensity, is shown in fig.II.30, for the level of J where both modes have the same probability. As for the experiment (see fig.II.13), the dynamics of the system develops close to the unitary arc of circle, where the two fixed points relative to the two modes are found. As discussed in sec.II.3.5, spontaneous emission has a twofold effect. On one hand it adds noise to the modal emission, which can be divided in "in phase" fluctuations along r (then the visited region of the plane increases radially its shape) and in "antiphase" along ϕ (and in consequence mode hopping occurs with higher rate). On the other hand it shifts the position of the two fixed points from the axis along the unitary arc, because the emission of each mode becomes always greater than zero.

The variables $r(t), \phi(t), N(t)$ describe then the dynamics of the system. From eqs.II.38-II.40 using again the transformations described in [35], it is possible to find

the rate equations driving these new variables. Two quantities

$$\sigma = \frac{c+s}{2} \qquad \delta = \frac{c-s}{2} \tag{II.42}$$

appear in these rate equations: σ is related to the gain saturation induced by the total power of the laser (which is found to be proportional to σr^2), while δ reduces the gain saturation because of the partitioning of the power among the two modes.

We assume that the asymmetry of the modal gains is small (i.e. $N_c > 1$, $N_c \simeq 1$, $\varepsilon \ll 1$, $\delta \ll 1$) and that the laser operates close to threshold, so that the saturation is small ($\sigma r^2 \ll 1$). In these limit it is possible to find that, to the lower order in the small terms, the dynamics is governed by

$$\dot{r} = \frac{r}{2}\left[N - 1 - N\sigma r^2 + \frac{6D_{sp}N}{r^2}\right] + \sqrt{2D_{sp}N}\,\xi_r \tag{II.43}$$

$$\dot{\phi} = -\frac{\sin 2\phi}{2}\left[N\delta r^2 \cos 2\phi + \varepsilon(N - N_c)\right] + \frac{2D_{sp}N}{r^2 \tan 2\phi} + \sqrt{\frac{2D_{sp}N}{r^2}}\,\xi_\phi \tag{II.44}$$

$$\dot{N} = \gamma\left(J - N - Nr^2\right) \tag{II.45}$$

It is easy to recognize that ϕ is completely driven by the other two variables, because it is absent from their equations of motion. Moreover its evolution time scale ($\dot{\phi} \simeq -\phi(\delta + \varepsilon) \ll 1$) is of the second order in small quantities, while that of r and N are of the first order ($\dot{r} \simeq -r$, $\dot{N} \simeq -N$). Since we are mainly interested in time scales long enough (the hopping is of the order of tens of μs) in order not to take into account transient effects and to have completely damped relaxation oscillations of r or N, we will consider that they both have reached the vicinity of their steady states. Therefore, neglecting the stochastic terms in eq.II.43 and eq.II.45, r and N take the following values

$$r \cong r_0 = \sqrt{\frac{J-1}{1+\sigma J}} \tag{II.46}$$

$$N \cong N_0 = \frac{1+\sigma J}{1+\sigma} \tag{II.47}$$

When the current J is time dependent, this approximation is valid if J does not change too fast in time. In the case of an Orstein-Uhlenbeck stochastic process (that we will consider later), it should be required that its correlation time τ (see sec.II.3.4) is longer than the typical relaxation time of total intensity. This condition is generally met in the experiment because the setup allows for τ^{-1} of the order of tens of MHz, while relaxation oscillations are in the GHz regime for the DC current used.

With these assumptions the dynamics can be geometrically represented as follows. As the total intensity r^2 is taken as fixed at the value r_0, in the plane (ρ_+, ρ_-) of

fig.II.30 and fig.II.12 the motion is now forced along a manifold (approximated as a portion of a circle of radius r_0) connecting the fixed points. Radial fluctuations of total intensity (the "in phase" component of noise) are completely neglected. In this way the hopping dynamics is effectively one-dimensional and, as it was done in the experiment (see sec.II.3.5), it is described by the variations of $\phi(t)$, which determines how the total power is partitioned between the modes. The equation of motion for ϕ brings then all the relevant information. After the hypothesis expressed in eqs.II.46-II.47, $\phi(t)$ is described by one single stochastic differential equation

$$\dot{\phi} = -\frac{1}{2}\left[a\cos(2\phi) + b\right] + \frac{2D_\phi}{\tan(2\phi)} + \sqrt{2D_\phi}\,\xi_\phi \tag{II.48}$$

where the parameters are defined by

$$a = N_0\delta\, r_o^2 = \delta(J-1)/(1+\sigma) \tag{II.49}$$

$$b = \varepsilon(N_0 - N_c) = \frac{\varepsilon\sigma}{1+\sigma}(J - J_s) \tag{II.50}$$

$$D_\phi = \frac{D_{sp}N_0}{r_0^2} = \frac{(1+\sigma J)^2}{(1+\sigma)(J-1)}D_{sp} \tag{II.51}$$

$$J_s = \frac{(1+\sigma)N_c - 1}{\sigma} \tag{II.52}$$

Eq.II.48 can be written in a usual Langevin form (see eq.II.8) extracting from its deterministic part a potential $U(\phi)$:

$$\dot{\phi} = -U'(\phi) + \sqrt{2D_{sp}}\,\xi_\phi \tag{II.53}$$

where the potential is given by

$$U(\phi) = -\frac{a}{16}\cos 4\phi - \frac{b}{4}\cos 2\phi - D_\phi \ln\sin 2\phi + c \tag{II.54}$$

Then one single equation describing the hopping between modes is obtained when the current J is a fixed parameter. Here noise is given by spontaneous emission (D_ϕ then D_{sp}) and it enters as an additive term in the equation. The dynamical hypothesis formulated from the experimental observations in sec.II.3.6 and the one dimensional stochastic differential equation eq.II.53 resulting from the reduction of the complete model are in good agreement.

It is worth noting that the same equation II.48 has been derived in [28] to describe polarization switching in VCSELs, the starting point for this theoretical derivation being the San Miguel-Feng-Moloney model [58]. In this work the physical meaning of the variable ϕ differs from here, as it represents the polarization angle of the emitted light. Thus the two potential minima correspond to the two orthogonal linearly polarized directions. Also in [26] the authors have derived a one-dimensional Langevin

equation for the polarizations in VCSELs starting from a rate equation model. Indeed it can be shown that, with a suitable reinterpretation of the variable and parameters, this equation can be reduced to eq.II.48. This makes a link between the two different systems, and it will be interesting to study similarities and differences of current modulation effects over the symmetry of the polarization states in VCSEL with respect to that of longitudinal modes of bulk lasers.

II.6.3.1. Discussion

The stationary probability distribution $\mathcal{P}(\phi)$, solution of the Fokker-Plank equation corresponding to eq.II.53, is easily found once the potential $U(\phi)$ is known (see sec.II.3.4.2) from

$$\mathcal{P}(\phi) = \mathcal{P}_o \exp(-U(\phi)/D_\phi) \tag{II.55}$$

with $\mathcal{P}_o$ being the normalization constant. Importantly, it is found from the shape of the potential of eq.II.54 that, in the strong coupling regime ($c > s$), there exists a range of current values where the system is bistable. Within this region, the current J controls the symmetry of the potential through the term proportional to b. At the value $J = J_s$, b vanishes and and the potential becomes symmetric under the transformation $\phi \to (\pi/2 - \phi)$. This is the symmetrical situation where the residence times of the two modes are equal. It is worth noting that the potential depends explicitly on D_ϕ (i.e. on D_{sp}) through the logarithmic term in eq.II.54. This term is usually very small for weak noise except at the extrema ($\phi = 0, \pi/2$) where it diverges logarithmically. Then $\mathcal{P}$ vanishes linearly there. Physically, this corresponds to the fact that spontaneous emission is always present in the modal emission so the two modes are never completely switched off, as it was discussed in sec.II.3.5 for the experimental phase space.

In order to check the validity of the reduced model, the potential given by the probability distribution of ϕ, extracted from the direct simulation of the complete model (eq.II.30-II.32), is compared to the potential found in eq.II.54. As from the experimental time traces, the value of $\phi(t)$ is found from the simulated modal amplitudes by $\phi = \text{atan}(|E_+|/|E_-|)$. From its distribution $\mathcal{P}(\phi)$, the potential is found by eq.II.55 and plotted in fig.II.31 for the symmetrical value of the current $J = J_s = 1.195$. The form of $U(\phi)$ of eq.II.54 then accurately follows the numerical data.

The experimental quasi-potentials of the variable ϕ can be well fitted by the functional form of the potential $U(\phi)$ of the reduced model. These potentials were shown in fig.II.13 where we discussed the reduction to one dimension for the real system. The fitting of the experimental points, shown as a continuous line in the second row of fig.II.13, was performed using the function $U(\phi)$ given by eq.II.54.

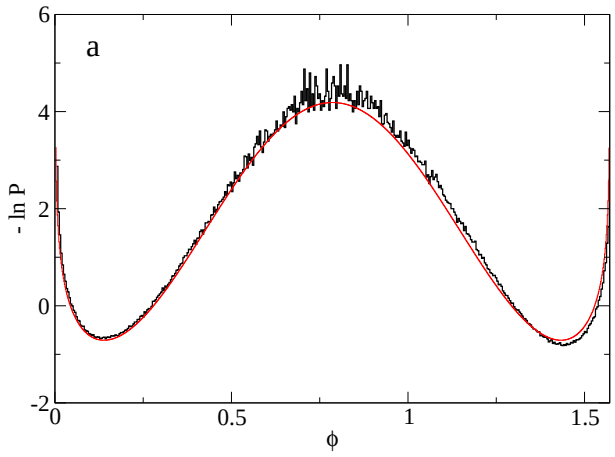

Figure II.31.: Comparison between the reduced model and the simulation of the rate equations for $J = 1.197$, $D_{sp} = 7\,10^{-6}$. The grey line is the potential of the reduced model, the black line is the quasi-potential extracted from the simulated temporal traces of the complete model. We use the following values for the parameters: $\varepsilon = 0.1$, $s = 1.0$, $c = 1.3$, $N_c = 1.1$, $\gamma = 1.1$.

For weak noise it is also possible to estimate from $U(\phi)$ (eq.II.54) the two potential barriers as $\Delta U_\pm = \frac{(a \pm b)^2}{8a}$. In the vicinity of the symmetrical point $J \simeq J_s$ these become

$$\Delta U_\pm \simeq \frac{\delta(J_s - 1)}{8(1+\sigma)} + \frac{\delta \pm 2\varepsilon\sigma}{8(1+\sigma)}(J - J_s) \tag{II.56}$$

We can neglect the fact that the noise strength D_ϕ depends on J; in fact it was verified that this gives negligible effects with respect to variations due to the current over $\Delta U_\pm$. Therefore we assume that changing the current only affects the barriers through eq.II.56. With this simplification the corresponding residence times are given by (see eq.II.9 and II.10)

$$T_\pm = T_s \exp\left[\frac{\delta \pm 2\varepsilon\sigma}{8D_\phi(1+\sigma)}(J - J_s)\right] \tag{II.57}$$

Here T_s is the residence time at the symmetry point and, as expected, it decreases with increasing spontaneous emission noise. Comparing this equation with the experimental results, it is possible to reduce the choice for the relevant region of parameters. In fact the behavior of the residence times with the DC level of the current depends on the value of the difference $\delta - 2\varepsilon\sigma$ in the exponent of $T_\pm$. Increasing J around J_s may lead to an increase of both $T_\pm$ if $2\varepsilon\sigma < \delta$, or to an increase of T_+ accompanied by a decrease of T_-, if instead $2\varepsilon\sigma > \delta$. It is possible to discriminate which case is the relevant by comparing the experimental residence times of the two modes as a

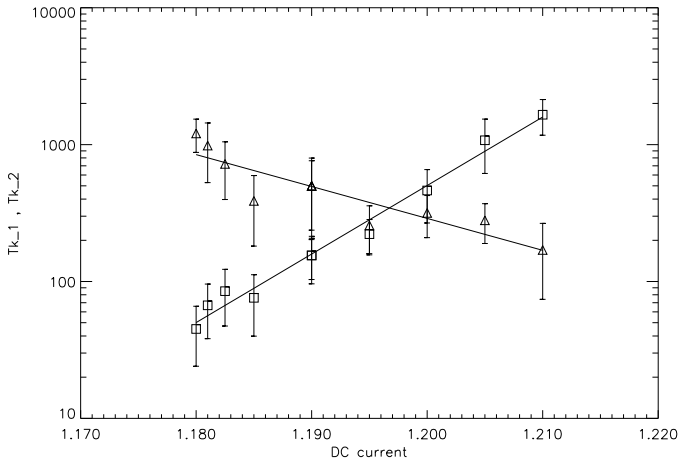

Figure II.32.: Simulation of the complete model: the average residence times are extracted from the simulated time series and plotted as a function of the DC level of J. Triangles refer to mode $(-)$, squares to mode $(+)$ and lines are exponential fits. Parameters: $\varepsilon = 0.11$, $s = 1$, $c = 1.1$, $N_c = 1.1$, $\gamma = 0.01$ (then $2\varepsilon\sigma > \delta$). See fig.II.10.

function of J, that were shown in fig.II.10. As it appears, an exponential dependence was also found in the experiment so the parameters of the model should be limited to the case

$$2\varepsilon\sigma > \delta \tag{II.58}$$

in order to fit the experimental asymmetry of slope of the two curves. The average residence times can be extracted also from the simulation of the complete model, and their dependence with J (shown in fig.II.32) is in agreement with the exponential one found in eq.II.57 and with the experimental result presented in fig.II.10.

II.6.4. Current fluctuations and multiplicative noise

It is possible to include current fluctuations letting $J \to J + \delta J(t)$. The following considerations hold for an arbitrary time dependence of $\delta J(t)$, under the limitations necessary to eliminate the total intensity dynamics and obtain eq.II.46. If we are interested in a noisy current modulation, we have to model the finite bandwidth of the experimental electrical noise like a Ornstein-Uhlenbeck process with zero mean $\langle \delta J(t) \rangle = 0$ and correlation time τ. Its dynamics can be described by

$$\dot{\delta J} = -\frac{\delta J}{\tau} + \sqrt{\frac{2D_J}{\tau}}\,\xi_J \tag{II.59}$$

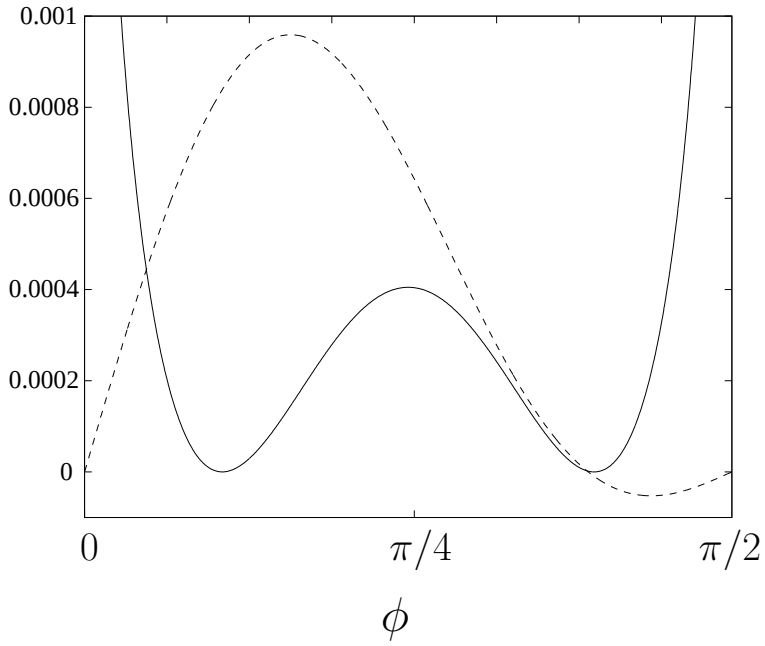

Figure II.33.: Solid line: potential $U(\phi)$ from the reduced model (eq.II.54). Broken line: rescaled multiplicative term $-V'(\phi)/40$ of eq.II.63. Multiplicative effects of current modulations come from the different symmetry of these two terms. Parameters used: $c = 1.3$, $s = 1.0$, $\varepsilon = 0.1$, $J = J_s$, $D_{sp} = 9\,10^{-6}$

(where ξ_J is a white noise source) which means that the correlation function is given by

$$\langle \delta J(t) \delta J(0) \rangle = D_J \exp(-|t|/\tau) \tag{II.60}$$

The effect of a time-dependent current makes the potential become fluctuating: the a, b, and D_ϕ coefficients become time-dependent quantities and the potential barriers $\Delta U_\pm(t)$ change accordingly. For weak noise, and close to the symmetry point ($\delta J \ll J_s - 1$) they are computed from the approximated formula II.56 with $J - J_s$ replaced by $\delta J(t)$:

$$\Delta U_\pm(t) \simeq \frac{\delta}{8(1+\sigma)}(J_s - 1) + \frac{\delta \pm 2\varepsilon\sigma}{8(1+\sigma)}\delta J(t) \tag{II.61}$$

The barriers' height depends linearly on δJ to leading order. Obviously, this last expression makes sense only when the fluctuating term is subthreshold, i.e., whenever the system is bistable (a large enough δJ could occur making the potential single well).

The effect of the current modulation over the symmetry of the emission becomes more evident writing the new Langevin equation when $\delta J \neq 0$. Putting all the terms

together it is found, to the first order in δJ, that eq.II.53 becomes

$$\dot{\phi} = -U'(\phi) - V'(\phi)\,\delta J + \sqrt{2D_\phi}\,\xi_\phi \tag{II.62}$$

where the new multiplicative term $(-V'(\phi)\delta J)$ appears. This is given by the expression

$$-V'(\phi) = -\frac{1}{2(1+\sigma)}(\delta\cos 2\phi + \varepsilon\sigma)\sin 2\phi \tag{II.63}$$

and can be derived from the "multiplicative potential"

$$V(\phi) = -\frac{\delta}{16(1+\varepsilon)}\cos 4\phi - \frac{\varepsilon\sigma}{4(1+\sigma)}\cos 2\phi \tag{II.64}$$

From fig.II.33 it is clear that the function $-V'(\phi)$ has a different symmetry with respect to the original potential $U(\phi)$. Given the condition for the parameters expressed in eq.II.58, this different symmetry is due to the positive value of δ, i.e. to the higher value of the cross with respect to the self saturation term (strong coupling).

As discussed for the experiment in sec.II.4.3, it results that the effect of the modulation δJ is not the same in the vicinity of the two solutions. When the current is randomly fluctuating in time, mode (+) (corresponding to $\phi \simeq 0$) experiences noise stronger than mode (−) ($\phi \simeq \pi/2$). Then mode (+) becomes less stable than mode (−) with increasing injection of noise. This is a simple representation of multiplicative noise, i.e. noise whose amplitude depends on the state of the system, here indicated by ϕ. When the current is modulated sinusoidally (and with a subthreshold amplitude), this description holds but internal noise is the only responsible for switching. As the modulation amplitude is not the same for the two modes, the system has more probability to escape from the (+) solution than from the (−) solution. The global effect of a modulation is therefore in average a change in the symmetry of the potential (that in the experiment was measured by the ratio of the residence times η) towards mode (−) ($\phi \simeq \pi/2$).

When noise is injected into the current, it is important to compare the time scales present in the system. In particular, one should compare the relaxation time T_R within the wells with both the injected noise correlation time τ and the residence times $T_\pm$. An estimate of T_R is given by the inverse of the curvature of the potential well and it is of the order of 5 ns. Moreover, relaxation oscillations should contribute to T_R, and as they are in the GHz regime we can consider T_R as the shortest time scale in our system. In fact τ is of the order of 100 ns and $T_\pm$ is found in the range between 1 and 1000 μs. Then we have $T_R \ll \tau \ll T_\pm$. This corresponds to the situation in which spontaneous emission is weak, so the jumps between modes are rare. Current noise modulates the potential barriers "slowly" (with respect to T_R), so the switching from one well to the other happens whenever the current fluctuations reduce enough

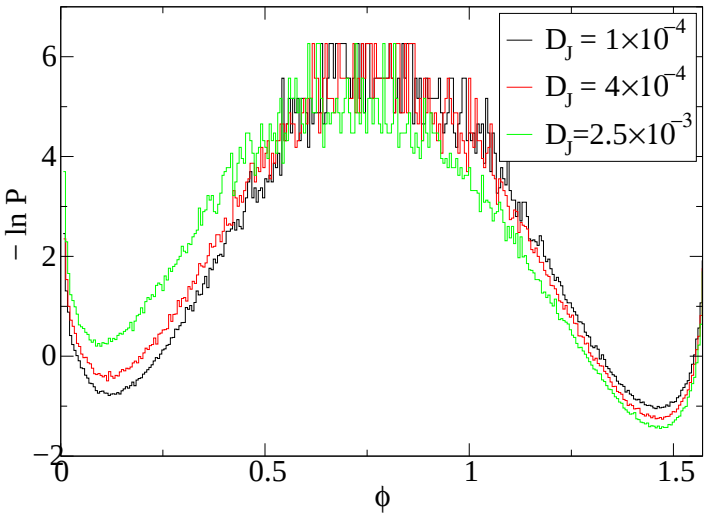

Figure II.34.: Simulation of the rate equations with current fluctuations given by D_J. The symmetry of the potential is affected by zero-mean noise injected into the current. Here $c = 1.3$, $J = 1.194$, $D_{sp} = 1.5\,10^{-5}$ and the other parameters are defined in the text. See fig.II.15.

the barrier of the potential. The minimal values of the potential barriers $\Delta U_\pm$ are statistical quantities, but in order to quantify the resident times we could choose them at the values attained for $\delta J \sim \mp\sqrt{D_J}$ (see eq.II.59). In this way, from eq.II.57, one obtains the expression for the residence times with current modulation strength D_J as

$$T_\pm \simeq T_s \exp\left[-K\,\frac{2\varepsilon\sigma \pm \delta}{1+\sigma}\,\frac{\sqrt{D_J}}{D_\phi}\right] \tag{II.65}$$

where K is a numerical constant. From this expression we can find the ratio η of the residence times, quantity that we used experimentally to measure the potential symmetry

$$\eta \equiv \frac{T_+}{T_-} = \exp\left[-K\frac{2\delta}{1+\sigma}\,\frac{\sqrt{D_J}}{D_\phi}\right] \tag{II.66}$$

As in the experiment, η is exponentially decaying if the current noise (rms) strength $\sqrt{D_J}$ is increased. This gives further confidence that the model and its reduction describe well the experimental system.

In fig.II.34 the result of the simulation of the complete model, taking into account random current fluctuations, is shown for three different levels of injected noise. The probability distribution of ϕ is converted into the potential by eq.II.55, as done pre-

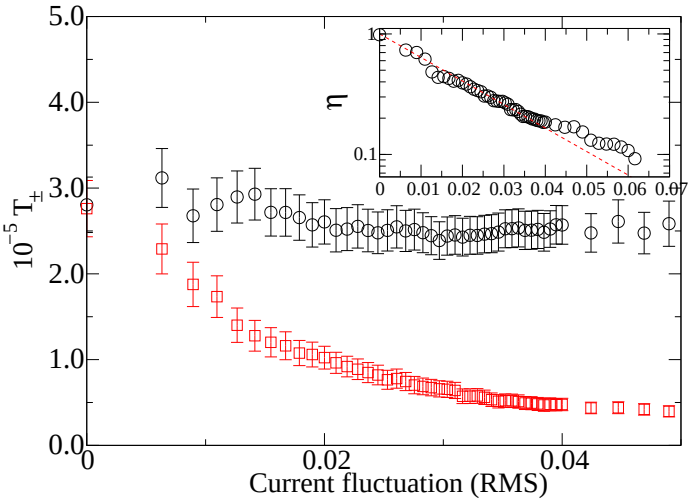

Figure II.35.: Simulation of the rate equations with current fluctuations: residence times T_+ (squares) and T_- (circles) as a function of the current noise. The inset show the ratio η of the two times and the dashed line is an exponential fit. Parameters are the same as in fig.II.34. See fig.II.14.

viously. As it is immediately clear, an increase of the noise strength injected in J changes the relative symmetry of the potential towards mode $(-)$ at $\phi \simeq \pi/2$. This result is in agreement with the experimental facts described in fig.II.15. In fig.II.35 the outcome of the simulation of the complete model, measuring the two residence times, is presented. It is found that T_+ and T_- are affected asymmetrically by the noise modulation of the current. Their ratio η is an exponential decaying function of the rms current noise as it was for the experimental results shown in fig.II.14.

In conclusion, all these features derive from the difference of symmetry (in eq.II.62) between the multiplicative term (proportional to the fluctuations $\delta J(t)$) and the potential $U(\phi)$, found in absence of external modulation. From the model it appears that the strong coupling between the two modes is responsible for the bistability observed. Within this regime, the difference of symmetry of the two terms of eq.II.62 arises when $\varepsilon > 0$, which is a condition necessarily fulfilled (see eq.II.58) when model and experiment are compared. The dynamical hypothesis (sec.II.4.3) formulated from the experimental results and the one-dimensional analysis shown here are therefore in agreement and build confidence on the validity of the description of the model.

II.7. Conclusions

We have analyzed the temporal behavior of the longitudinal modes of bulk semiconductor lasers. Even if the emission in such devices is mono-mode for large regions of parameters, instabilities between two strongly competitive cavity modes always appear. In relatively small regions of parameters, in fact, in general it is found a switch of the active mode towards another resonance with longer wavelength. Fixing the parameters in these regions, because of bistability and noise, random *mode hopping* between the two modes is found.

We gave the description of the general (device independent) properties that characterize such transitions, focusing the attention on the role of the bias current. Based on the experimental observations, a dynamical hypothesis relates the laser system in the mode hopping regime with a simple one dimensional bistable dynamical system driven by noise. This reduction from a description of two variables to one single coordinate is possible because the total intensity is in good approximation a constant quantity even in the mode hopping regime.

Writing the rate equations for the laser, we could recover qualitatively the experimental features introducing phenomenologically a small asymmetry term between the linear differential gains of the two modes. A reduction from the rate equations to a single stochastic differential equation was performed, using time scales considerations and neglecting noise in the total intensity. This led to the expression of the deterministic potential which gives the framework for the noise-induced dynamics. The experimental modal distributions and their dependence on the bias parameter are in good qualitative agreement with the theoretical analysis.

We have studied experimentally how the mode hopping dynamics was affected by a modulation of the pumping current. Measurements suggested that the one-dimensional Langevin equation for the system should contain a multiplicative term proportional to the AC value of the current. The symmetry of the experimental potential in fact changes if the system is forced with a symmetric (periodic or random) modulation.

When current fluctuations are taken into account in the model, this new multiplicative term appears, depending on the difference between self and cross saturation terms and on the asymmetry between the modal gains, giving good qualitative agreement with the experimental characterization. The effect of the current modulations over the modal symmetry is explained then in terms of the multiplicative term, as it changes the effective strength of the modulation experienced by the two solutions.

Stochastic Resonance was also demonstrated in the experiment, both taking into account or avoiding the multiplicative effect of the bias current. In order to change the stochastic time scale of the hopping regime without changing the symmetry of the

potential, we took advantage of the knowledge of the parameters space of a particular device. On the other hand we have shown that in principle it is possible to realize Stochastic Resonance using the multiplicative effect of the current modulation to restore the symmetry of an initially asymmetric potential.

As a perspective, it will be interesting to analyze the similarities between *mode hopping* described here in cavity modes of bulk lasers and that found for the polarization states in VCSELs. It is possible in fact an unified description of the dynamics of both systems by means of the same Langevin stochastic equation, so it would be interesting to explore the multiplicative effect of current modulations in VCSELs.

III. Experimental study on control of cavity solitons in injected VCSELs

Abstract:
Non linear interaction between a semiconductor cavity and an external coherent electromagnetic field may give rise in the transverse plane to the formation of localized, self-sustained, bright peaks of laser emission, called cavity solitons. *We have analyzed experimentally their properties in Vertical-Cavity Surface-Emitting Lasers with external injection. The aim of our work is the control of their positions and velocities in the transverse plane. In fact their plasticity, together with their bistable nature and fast time-scales associated to semiconductors, make these structures attractive for applications, as optical bits of reconfigurable devices for parallel information processing. The control of such structures is limited experimentally by imperfections in the medium and in the injection beam. We study the role of imperfections of the laser cavity and we demonstrate that cavity solitons can be displaced by the action of external gradients in the injection beam. A soliton can be created by a local optical perturbation and, once generated, it can drift along the applied gradients. We observe this behavior and we measure velocities of the structures close to* 10^4 *m/s. Finally using a liquid crystal light valve to spatially modulate the phase of the injection, we can create, in the transverse plane, different stable configurations of cavity solitons, pinned by the external parametric profile.*

The work presented in this part of the thesis concerns the study of cavity solitons (CS) found in broad area Vertical-Cavity Surface-Emitting Lasers with external injection. Cavity solitons are bistable localized structures appearing as local intensity peaks in the homogeneous background of the field emitted by a nonlinear microresonator, under external coherent injection. As indicated by theory of localized structures, their positions on the transverse plane are in principle not rigid, and they can move under the effect of gradients in the parameters.

One of the main results in this field obtained by our group at INLN, was in [59] [60] the experimental demonstration of the existence of such transverse structures in semiconductor microcavities (2001). Once the existence of CS was proven, their

properties were analyzed extensively in [61]. The experimental results are affected by the homogeneity of the devices. In the past, inhomogeneities of the system were present in form of a strong length gradient of the laser cavity (2.6 GHz/μm in [59], then reduced of one order of magnitude in [61]) and in form of randomly distributed defects in the surface of the resonator. The observation of stable CS under the effect of such strong cavity length gradient was possible because of the presence of cavity defects. These have a pinning effect on CS, preventing their drift along the cavity gradient. Then the imperfections help the observations of CS, but, as long as the cavity gradient exists, it is difficult to show that their presence is not necessary for CS to exist.

We can now take advantage of the improved technology (from Ulm Photonics) in growing homogeneous cavities with large diameter and Fresnel number ($\simeq 4000$), reducing the effect of the cavity length gradient to be practically negligible. In these new devices it becomes then possible in principle to assess the distinctive features of localized structures in terms of motion. All the practical applications that make the use of such structures interesting in real systems, rely on the control of their state (on or off) together with their positions in the transverse plane. In fact, the plasticity of localized structures together with the fast response time of semiconductors [62] make these systems interesting for parallel information transmission or storage. The strength of an ideal soliton-based device is the possibility to be configured easily. Indeed this configuration is neither rigid nor definitive, but controllable by external parameters. Localized structures in an ideal system can be displaced and pinned over the transverse plane, acting on gradients over the system. Our work is then an effort in the direction of controlling the localized structures.

The first step is the experimental observation that a localized structure can be displaced in the transverse plane, over distances greater than its width, by a *change* of the external gradients acting on it. We observe that the stable position of the soliton changes accordingly to the strength of the applied gradients. This clarifies the role of the external gradients and of the defects in the cavity. On one hand, these observations indicate that the gradients act as a force over the soliton, as stated by the theory. On the other, this demonstrates that imperfections stabilize the structures but their presence is not necessary for the existence of CS.

Using then a *stationary* profile of the injection, we show experimental observations interpreted as the motion of localized structures, over distances much larger of their size, along the applied external phase and intensity gradients. This shows that the pinning effect of cavity roughness is small compared to the external gradients and that it can be overcome to some extent. In such conditions, the drift of a cavity

soliton along the applied gradients follows its switching-on. This can be induced by the internal noise of the system or, more interestingly, by an applied local optical perturbation. This latter result opens the way to applications with solitons as the optical shift register. We describe the region of the parameters where the motion along the stationary gradients can be found, and we give a description of the complex phenomenology shown by the system.

A further improvement of the experimental set-up was achieved by the use of a spatial modulator. This optoelectronic device allows to control the intensity and/or the phase of the injected beam. We show the possibility to fix the positions of the localized structures in different configurations on the transverse plane, defined by the applied phase profile.

This chapter is organized as follows. In sec.III.1 a brief introduction to the theoretical descriptions of localized structures is given, together with an overview of the mechanisms explaining their motion under external influences. In sec.III.2 we will describe the experimental setup. We study in sec.III.3 the effects of phase and intensity gradients over the stable positions of solitons. Here we propose also a simple method, based on localized structures, to visualize the cavity imperfections in the device. In sec.III.4 we report experimental observations indicating the motion of localized structures with stationary injection parameters. Finally, in sec.III.5 we describe the experimental system, based on a liquid crystal light valve, used in order to separately control the phase and intensity of the injection.

III.1. Introduction

Spatial structures arising from dynamical instabilities are present everywhere in nature; they were firstly studied in biology [63], hydrodynamics [64] and chemistry and finally in optics [65][66]. In this field, the interest also comes from possible applications based on the transverse dimensions of suitable optical systems.

In mathematics and physics, a soliton indicates a self-sustained solitary wave created by a balance between nonlinear and dispersive effects in the medium. In optics, with the name of spatial solitons are indicated propagating beams of light in which nonlinearity counterbalances diffraction, leading to a robust structure which propagates without being altered [67]. The non linear media that can host such beams needs to be, in this conservative scheme, self-focusing: the index of refraction is proportional to the intensity of the light (Kerr media).

It became clear that it is possible to find similar soliton-like solutions in systems where the propagation is confined in an optical cavity. In this scheme, the losses from the cavity mirrors needs to be balanced by some external mechanisms, as optical injection. Such system is then intrinsically dissipative because losses and pumping mechanisms are necessarily present. Cavity solitons should be distinguished from spatial solitons. In fact, stable cavity solitons can exist, somehow unexpectedly, in media with different properties from, even opposite to, those required for spatial solitons, as self-focusing. The relationship between cavity solitons and non-linear patterns makes this difference. In fact the origin of cavity solitons cannot be simply described as the result of the balance of diffraction and focusing in the cavity. Rather, they should be considered as single independent cells of a larger non-linear pattern.

Cavity solitons in semiconductor cavities were extensively studied theoretically since the works in '80 [68][69]. The main ingredient that the theory suggested is the use of a system that presents a large aspect ratio, or Fresnel number, together with energy injection from a plane wave (which is often called holding beam, HB). For semiconductor lasers, as in our work, the input energy into the system comes from the optical injection of the holding beam together with the electrical pumping of the diode. The system is driven in a region of parameters where the output is uniform. This homogeneous solution of the system coexists, for the same values of parameters, with a pattern solution (hexagons, rolls etc.). Injecting then a localized optical pulse over the transverse plane (the so called writing beam) one can write a cavity soliton, which consists of a localized peak of high intensity over the homogeneous background. Due to its bistable nature, the soliton persists stable even after the pulse as long as the injected holding beam is kept on [70].

The idea at the base of possible applications, is to use the transverse plane of the system (perpendicular to the propagation) as a blackboard where spots of light can

be written and erased. In fact once the soliton is created, it can be erased by a similar pulse out of phase with respect to the first one [62]. Many solitons can be created across the transverse plane, and importantly they all are independent. In this way a configurable matrix of independent bistable bits can be created. This control is not possible with other types of transverse structures in optical systems. Transverse modes have always a correlation length along the transverse dimensions of the order of the size of the system; different distant points of the space are then coupled, and a local control of the output is not possible. On the contrary the transverse correlation length when solitons are present in the system is of the order of the soliton size (about 10 μm in our VCSELs). This property allows for creating arrays of independent structures.

In conclusion, it is worth noting that semiconductors cavities are the systems where the experimental finding of the presence of cavity solitons is the more appropriate for applications because of their fast response times (the switching-on of a soliton has been measured as less than 1 ns [62]). Anyway, similar structures have been observed in different optical systems, as for example in photorefractive resonators [71] and in lasers with saturable absorber [72]. The experiments on sodium cell and liquid crystal light valve give impressive experimental evidences of many properties of localized structures (for two reviews on these subjects see [67] [73]). The position of localized structures has been controlled experimentally by injection gradients [74] and the demonstration of the possibility of a shift register was also shown [75].

III.1.1. Theoretical descriptions

The theoretical works on cavity solitons can be divided roughly in two groups that have different approaches [77], differing on the identification of the mechanism at the origin of such localized structures. One approach (referred as "diffractive autosolitons") was developed by Rosanov and collaborators [69][78] from the study of fronts connecting different solutions. Switching wave connecting different stable states are found in many systems, as those described by reaction-diffusion equations. When diffusion in the medium is predominant, the most stable state wipes out the less stable [79]. When diffusion of carriers and diffraction of the field are present, small ripples are formed around the switching wave, and this constitutes a possible trapping mechanism for other fronts. In two dimensions then a front can close on itself and form a stable localized region where one solution is surrounded by the other. In this interpretation a soliton is then a self trapped switching wave [67].

For the other approach, started by Mandel in [80], the necessary mechanism is the so called modulational instability [81][76]. Under injection of an external field, for a certain region of parameters, the stationary homogeneous solution looses its stability

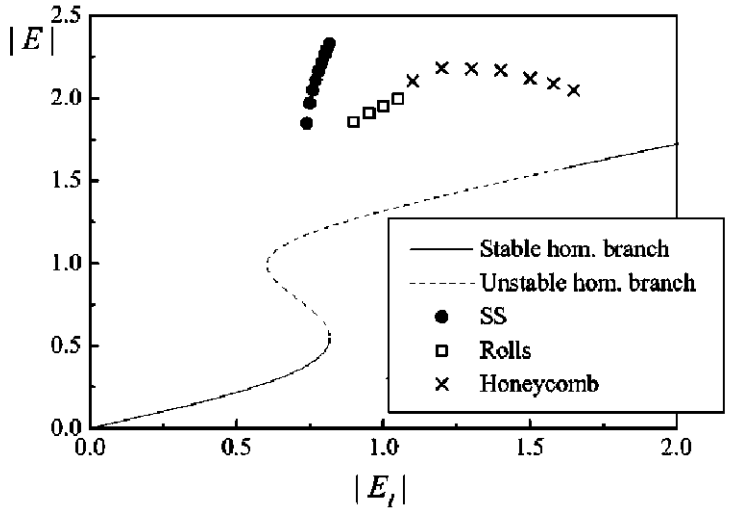

Figure III.1.: Output ($|E|$) versus input (E_I) field for the model in [76] for the active (with population inversion above transparency but below threshold) resonant case. The line corresponds to the homogeneous solution E_S which loses stability from a modulational instability. Results from numerical simulation (points) show the region where patterns and cavity solitons (SS) are found.

in favor of a periodically modulated one. Mathematically one homogeneous solution $E_s(x, y)$ is unstable against a spatially modulated perturbation if its perturbated form

$$E = E_s + e^{\lambda t + i(k_x x + k_y y)}\ \delta E_S \tag{III.1}$$

can grow exponentially in time (i.e. exists $\lambda > 0$) for a non zero value of $k = (k_x,\ k_y)$. Then the system will develop a spatial frequency with transverse wave vector k, and this leads to the onset of a pattern. A second necessary condition is, for an interval of the injection intensity, the coexistence between the pattern and the homogeneous stationary solutions. Cavity solitons are then a special solution which connects the pattern solution with the homogeneous stationary state. Therefore they are an example of localized structures previously discovered in other fields [82][83]. In this scheme of modulational instability, the region of parameters where solitons are found is therefore very close to a branch of stable spatial patterns, as in fig.III.1; this feature is found also in our experiments (even if the observation of regular patterns as hexagons still misses in semiconductor lasers, probably because of cavity inhomogeneities) and contributes in building confidence in this mechanism for the onset of spatial instabilities in our experimental system.

This scenario was analyzed by Coullet et al. in [84] where the authors, using general properties of differential equations, give a general dynamical characterization for one

dimensional systems (however similar results are obtained also in 2D simulations [85]). Considering a stable infinite pattern coexisting with a homogeneous stable state, they demonstrate that there exists a region of parameters where a front connecting the two solutions is stable. In that region of parameters one solution cannot prevail on the other, as in purely diffusive systems, because of a "nucleation energy" needed in order to create or annihilate every cell of the pattern. In that region, they show that an infinite set of localized N-peaked states can be found with the N=1 states (single peak solitons) the most probable to observe.

III.1.2. Cavity solitons motion

Many theoretical analysis show that cavity solitons can move along the transverse plane without energy cost. This is related to the translational symmetry of the equations. The results indicate that the soliton behaves as an overdamped Aristotelian particle [67][86], whose velocity (instead of acceleration) is proportional to the external force.

One of the first works [87] showing the effects of a phase gradient of the holding beam, considered a class A two-level system in the mean-field approximation [88], with saturable absorber nonlinearity. When the input holding beam $E_I = E_{I_0}\, exp(i\overrightarrow{K} \cdot \overrightarrow{x})$ is considered tilted with respect to the optical axis ($\overrightarrow{K} \neq 0$), creating a phase gradient, the equation indicates that any static solution existing for the on-axis injection ($\overrightarrow{K} = 0$) should survive in the misaligned problem, but drifting with a velocity proportional to $\overrightarrow{K}$. Then, when the phase profile of the injected beam presents extrema, cavity solitons (here called optical bullet holes because of the saturable nature of the absorber) are attracted towards them, where their velocity becomes zero. Therefore it is possible to configure an array of localized structures.

The general behavior of stable solutions like cavity solitons under the effects of external or internal variations of parameters can be found, following ref. [89], writing the equations driving the system in the concise and general form

$$\frac{\partial E}{\partial t} = f(E) + E_I \tag{III.2}$$

Here E represents all the possible variables, E_I the driving field(s) and f is the non linear function for the system. All these quantities are in general vectorial. A stationary solution for the problem is E_S (so $\partial_t E_S = 0$), and a small perturbation is considered. Due to the perturbation the solution suffers a slight deviation from the stationary value, then $E = E_S + \epsilon$. It is important to understand how the perturbation ϵ evolves in time, so its evolution equation is written from eq.III.2. Regardless the

nature of the perturbation (internal or external) the evolution of ϵ is driven by

$$\frac{\partial \epsilon}{\partial t} = J_S \cdot \epsilon + \mathcal{P} \tag{III.3}$$

where $J_S = \left(\frac{\partial f}{\partial E}\right)_{E_S}$ is the Jacobian of $f(E)$ at the stationary solution and $\mathcal{P}$ is the general perturbation. Then the deviation ϵ is decomposed on the basis formed by the eigenvectors $|u_j\rangle$ of the Jacobian as $\epsilon = \Sigma\ a_j|u_j\rangle$, where $J_S|u_j\rangle = \lambda_j|u_j\rangle$, and the similar condition $\langle v_j|J_S^t = \langle v_j|\zeta_j$ holds for the transposed problem. Using this decomposition and projecting eq.III.3 on the transposed basis $\langle v_j|$, one arrives to the equation describing the evolution of the components a_j of the perturbation ϵ

$$\frac{da_j}{dt} = \lambda_j a_j + \frac{1}{\langle v_j|u_j\rangle}\langle v_j|\mathcal{P}\rangle \tag{III.4}$$

where the vector basis can be further normalized. It is reasonable to consider that the deviation ϵ from the stationary solution grows from zero when the perturbation is turned on, i.e. $a_j(t=0) = 0,\ \forall j$. Then from eq.III.4 one obtains a different temporal behavior of $a_j(t)$ if λ_j is equal or not to zero. In fact

$$a_j(t) = \frac{1}{\lambda_j}\frac{\langle v_j|\mathcal{P}\rangle}{\langle v_j|u_j\rangle}(e^{\lambda_j t} - 1) \quad \text{if} \quad \lambda_j \neq 0 \tag{III.5}$$

$$a_0(t) = \frac{\langle v_0|\mathcal{P}\rangle}{\langle v_0|u_0\rangle}\, t \quad \text{if} \quad \lambda = 0 \tag{III.6}$$

Because E_S is a stable solution, all the eigenvectors $|u_j\rangle$ have eigenvalues with negative real part, except $|u_0\rangle$. This means that after a transient ($t \to \infty$), all a_j will be damped and a_0 will dominate. This shows how the effect of a perturbation on a stationary stable solution is determined by the projection $\langle v_0|\mathcal{P}\rangle$ of the perturbation $\mathcal{P}$ over the neutral mode $\langle v_0|$ of the transposed Jacobian J_S^t. All the internal degrees of freedom of a cavity soliton are then suppressed, leaving only its translational freedom, giving it its particle-like behavior.

In fact, the velocity of the stationary solution E_S is proportional to da_0/dt found in eq.III.6. For times long enough (few medium lifetimes) we have seen that the perturbation ϵ can be written only in terms of the neutral mode, $\epsilon = a_0|u_0\rangle$, and the perturbed solution is then $E = E_S + a_0|u_0\rangle$. When E_S is a cavity soliton, one finds [89] that the neutral mode $|u_0(x)\rangle$ is proportional to the spatial gradient of the soliton itself, i.e. $|u_0\rangle = \alpha\frac{dE_S}{dx}$. So the perturbed solution can be written as $E = E_S + a_0\alpha\frac{dE_S}{dx}$. If now we consider a soliton slightly displaced from its initial position x_o, we can write at the first order the perturbed solution as $E = E_S(x_o + \xi) = E_S(x_o) + \xi\frac{dE_s(x_o)}{dx}$, then $a_0\alpha = \xi$. The velocity of the soliton is given then by the evolution of the displacement

ξ, which can be written in terms of a_0:

$$v = \frac{d\xi}{dt} = \alpha \frac{da_0}{dt} = \alpha \frac{\langle v_0 | \mathcal{P} \rangle}{\langle v_0 | u_0 \rangle} \tag{III.7}$$

where eq.III.6 has been used. Therefore at first order the velocity is directly proportional to the projection of the perturbation on the neutral mode.

In the case of small phase and amplitude gradients, the perturbation can be written as $\mathcal{P} = E_I^h ikx$ and $\mathcal{P} = E_I^h kx$ respectively. This comes from the approximation of small variations $[E_I(x) = E_I^h e^{(i)kx} \simeq E_I^h(1+(i)kx)]$ from the background homogeneous input field E_I^h. The result is a linear dependence of the velocity on the phase or intensity gradient k.

Theoretical studies on the effects of external or internal gradients over the motion of solitons exist also taking into account the frequency and the size of the spatial modulations [90] [86] or thermal effects in semiconductor microcavities [91][92].

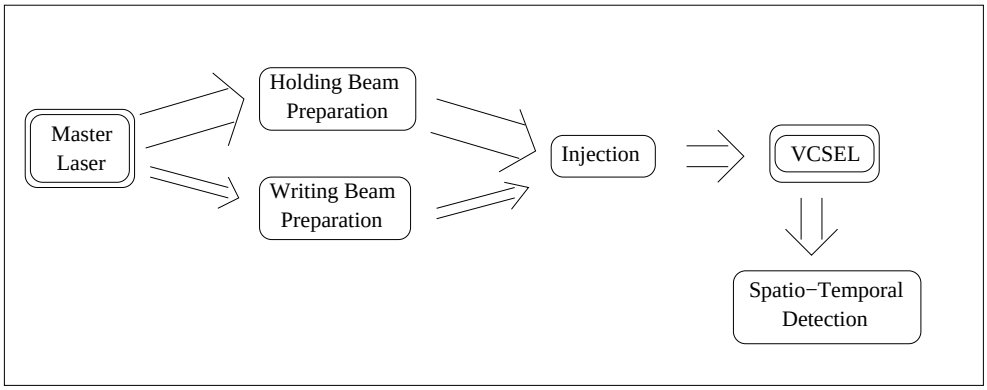

Figure III.2.: Scheme of the experimental setup

III.2. Experimental Setup

The experimental setup is based on a master/slave configuration, where the injected beam (holding beam, HB) from the master laser is manipulated in order to have controlled modulations of its intensity and phase transverse profile. A second weaker injected beam (writing beam, WB) can be used as a local optical perturbation. We divide the setup for clarity in different parts, shown in fig.III.2: master laser, holding and writing beam preparation systems, injection system and spatio-temporal detection.

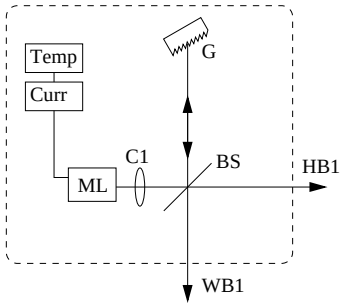

Figure III.3.: Master laser source.

1. *Master laser.* This is the coherent source of laser light needed for injection. It consists of a Pirelli edge emitting semiconductor laser (ML) with frequency-filtered feedback from an external cavity (in a modified Littrow configuration) as in fig.III.3. The laser current is controlled with a stable (10 μA) current generator, and the substrate temperature is kept fixed (up to 0.01^{o}C) by a Peltier module. After the collimator C1, the beam is divided in two by the beam-splitter BS (50% reflectivity) and one part is sent back into the laser as the first order of

the diffraction grating G (1800 lines/mm). The laser displays then monomode stable emission with a bandwidth lower than 290 KHz (estimated by heterodyne measurement), and almost continuously tunable frequency (using the interplay of the external and internal comb of modes) in the range 960-980 nm. Its main exit beam (HB1) has a power of 70 mW at the typical current of 150 mA, and it will be used as the principal injection source for the VCSEL. The second beam (writing beam, WB1) has a power of 20 mW, and will be used highly focused on the VCSEL acting as a local perturbation.

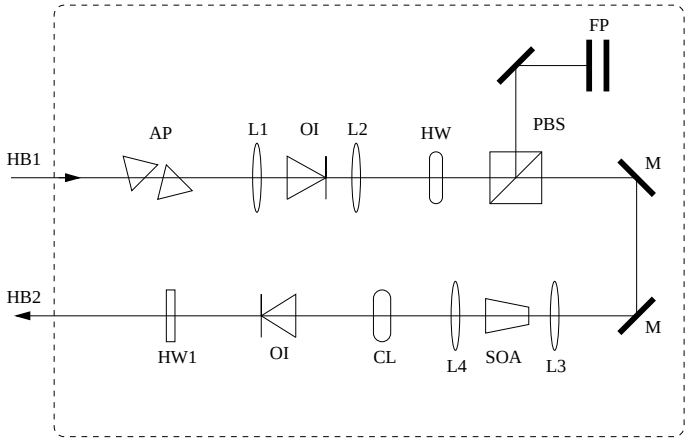

Figure III.4.: Holding beam preparation.

2. *Holding beam preparation.* Fig.III.4. The beam HB1 needs to be prepared before being injected into the VCSEL. At the master exit two anamorphic prisms (AP) adjust the elliptical profile of the collimated beam, and an optical isolator OI inserted in a 1:1 telescope (L1, L2) makes the injection unidirectional and prevents for spurious feedback towards the master laser. The use of the half-wave plate HW and the polarizer beam splitter PBS allows for changing the level of injected power, and the spectral purity of the master laser is monitored in a Fabry-Perot interferometer. When higher powers are needed, the tapered semiconductor optical amplifier SOA (between a 1:1 telescope formed by collimators L3 and L4) is used. A cylindrical lens CL is then necessary to adjust the strong asymmetry of the exiting beam and a second optical isolator OI prevents destructive feedback to the amplifier. The last element is a half-wave plate (HW1) used to turn and fix the polarization vertical with respect to the plane of the table. This will be important using the Liquid Crystal Light Valve described in sec.III.5.

3. *Writing beam preparation.* Fig.III.5. The writing beam follows an independent

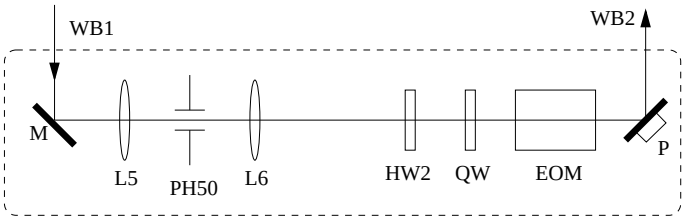

Figure III.5.: Writing beam preparation.

path. It is spatially filtered by the Fourier filter formed by the lens L5, L6 (a 1:1 telescope) and the 50 μm diameter pin hole PH50. When a fast pulsing writing beam is required, the electro-optic modulator EOM is inserted. The half-wave plate HW2 and the quarter-wave plate QW are used in order to match the input polarization of the EOM. The resulting beam consists of a train of pulses at a frequency in the KHz range, with width of 100 ns each and with a rise and fall time less than 1 ns. A piezo electric element (P) is mounted on the back of the last mirror in order to vary the optical path of the WB with respect to the HB in a sub-wavelength scale, so to change their interference condition.

4. *Injection.* Fig.III.6. The prepared holding beam HB2 (whose polarization is vertical) is spatially filtered by the Fourier filter formed by the collimator L7 (C280TM-B, 18 mm focal length), the 30 μm pin hole PH30 and the lens L8, which has a focal length of 10 cm and is mounted on a translational stage to control its distance from the aperture PH30. This distance is critical as it changes the phase profile of the injected beam arriving to the VCSEL. We will always work with a quasi-collimated holding beam, trying to have on the VCSEL a phase profile as flat as possible. This is done acting on the position of lens L8 along the axis, and minimizing the width of the far field of the reflected light on the VCSEL (see Detection). In fact minimizing the size of the Fourier transformed of the injected field, should produce the flattest phase profile as the number of transverse vectors in the injected field is minimized. The HB passes then trough a Mach-Zender interferometer formed by three beam splitters and one mirror mounted on a piezoelectric element (BS3: reflectivity 50%, BS4: 90%, BS1: 50%). The contrast of the interference fringes on the VCSEL plane is close to unity, and their orientation is easily changed by alignment. The total injected power, in front of the last collimator, is of the order of 10-15 mW. In spite of the relative simplicity of this scheme, amplitude and phase of the injected beam are in this way always coupled. In sec.III.5.1 we will describe the modifications of this set up, made in order to build a system that could control the phase and amplitude separately. The WB is superimposed to the

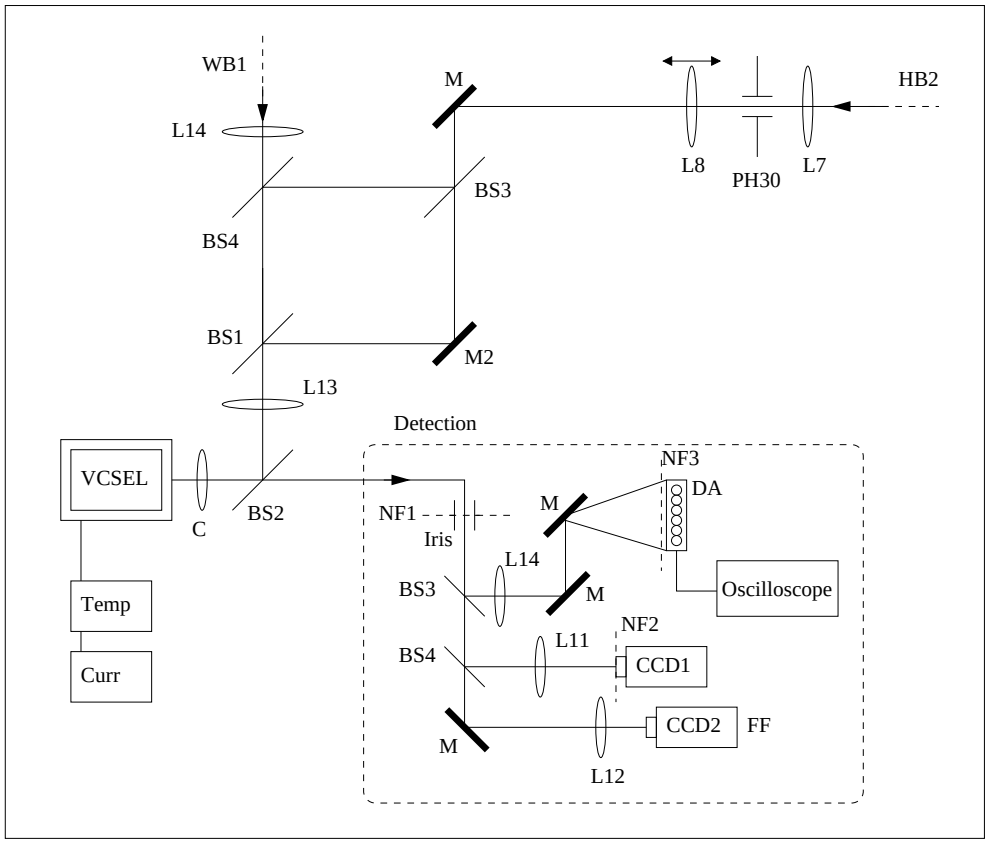

Figure III.6.: Injection and spatio-temporal detection (inset) scheme.

HB trough the beam splitters BS4 and BS1, and its power in front of the VCSEL is few tens of μW. Finally by means of the telescope formed by lens L13 (10 cm focal length) and collimator C (C350TM-B, focal length 4.5 mm), the size of the HB is reduced to the size of the VCSEL ($\simeq 200\mu$m). At the same time the WB is focused on the VCSEL passing through L14, L13 and C, having a waist of the order of 10 μm. The bias current of the VCSEL is controlled by a stable current generator (10 μA), and the substrate temperature is stabilized by a Peltier element (up to 0.01 ^{o}C).

5. *Detection*. Fig.III.6 (inset). The light injected into the VCSEL and reflected by its output mirror, together with the emission of the VCSEL itself, are sent to the detection system through the last beam splitter BS2 (reflectivity 90%). The collimator C determines a near field image of the VCSEL at the plane NF1 (indicated by a dashed line). There we put an iris (whose diameter is controllable) that we can move along the (x, y) plane, being z the propagation direction. We can therefore filter in the near field the zone we are interested

in. Two other near field planes exist (NF2 and NF3) in this configuration: NF3 (formed by the lens L14) is a large image of the VCSEL (the total magnification is around 1000) on the plane of a linear array of 6 fast avalanche photo-diode detectors (APDs), which give the temporal dynamics (with bandwidth of 350 MHz) of small regions of the transverse plane. The separation between two points in the VCSEL plane monitored by two neighboring detectors is of 8.9 μm. The area monitored by each detector has a diameter of less than 7.2 μm, which is of the order of the size of the CS found in this system. In order to maximize the length of the monitored spatial region, we use six detectors together with two synchronized oscilloscopes (Lecroy 7200A: 500 MHz analog bandwidth, 1Gs/s and HP Infinium 54831b: 600 MHz analog bandwidth, 2Gs/s) for simultaneous monitoring of six channels. The other near field image of the VCSEL output (NF2) is monitored by a CCD camera (CCD2) which is used together with the iris placed on the near field image NF1 to locate the points monitored by the detectors. Finally, CCD2 provides the far field profile of the VCSEL output.

III.2.1. The injected VCSEL

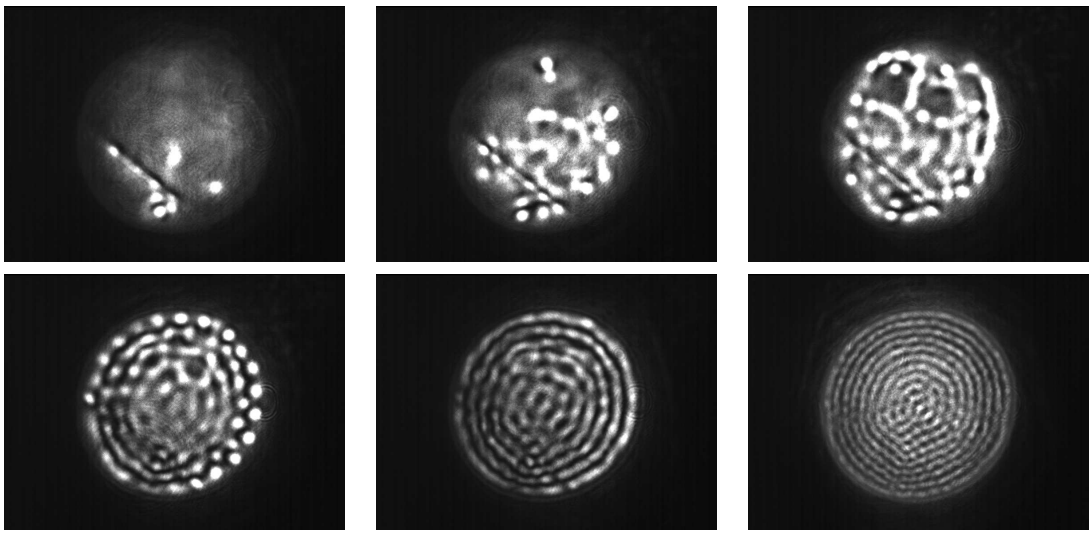

Figure III.7.: VCSEL near field under injection at fixed wavelength and for increasing current J. From left to right, top to bottom: J = 310, 333, 351, 372, 387, 450 mA.

The injected laser is a broad area (diameter 200 μm) bottom emitting Vertical Cavity Surface Emitting Laser, provided by Ulm Photonics. We have tested several devices with the same characteristics, and we have found very similar results. In the

explored range of temperature (16-23^{o}C), when the current is increased, due to the large surface, this laser does not reach a clear threshold before the occurrence of the thermal roll-off. Therefore, for the range of current explored, we consider that the VCSEL is driven below threshold and above transparency.

In these devices the cavity length gradient (as in [60]) can be neglected. However, in every tested device we have found some cavity defects that appears in form of lines or extended regions. These defects are visible when the VCSEL is injected close to resonance, as in fig.III.7 where the bias current of the VCSEL is increased. For a current level where interaction between the medium and the injection appears (310-330 mA), the presence of a line at the bottom of the image is evident. For higher currents (350-370 mA) two extended defects are also visible at the top of the image, as almost circular dark regions. The origin of the latter inhomogeneities is unclear, while the line defects may originate from the atomic strain of the semiconductor structure due to the difference in the lattice constant along the device. According to the manufacturers, these lines can propagate in the wafer for distances of the order of 1 mm. We have found that after about 300 hours of current injection into the VCSEL of fig.III.7, a new line defect appeared in the right side of the device. These defects are the main limiting factor for the observation of motion of localized structures, because they create strong local gradients, limiting the available transverse space.

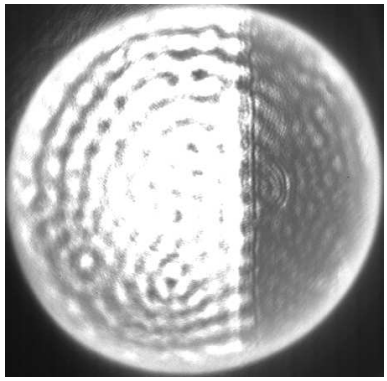

Figure III.8.: Near Field of the VCSEL under strongly modulated injection. Even if a black screen, imaged onto the VCSEL, prevents injection to the right side of the laser, patterns tend to extend to the whole surface. $J = 512$ mA.

III.3. Phase and intensity gradients

In this section we analyze experimentally the effects of phase and intensity gradients of the holding beam on the stable positions of cavity solitons, using as injection a set of interference fringes. For different configurations of the two beams from the arms of the interferometer (see fig.III.6), we observe different stable positions of the localized structures.

The following results of this section rely on the fact that the injection beam is in form of interference fringes (see for example fig.III.10). We note here that the spatial coupling of the system is assured even under a strongly modulated injection, by diffraction inside the VCSEL cavity. In fact, as it is shown as an example in fig.III.8, for detuning where patterns develop they extend to the whole surface of the VCSEL by diffraction inside the cavity, even if the injection does not cover the whole surface. Then the spatial dimensions of the system are still coupled, by diffraction, even with a strongly inhomogeneous injection. We observe that inside an intensity fringe whose width is slightly larger than its diameter, a soliton maintains unchanged the properties which are observable in the case of two dimensional homogeneous injection, as its shape and bistability. Moreover, it can move in both directions, as we will show in the next sections.

III.3.1. Phase and intensity gradients induced by interference

The aim of this section is to give the general expressions of the intensity and phase profile of the injected field when the holding beam passes through an interferometer and consequently is split in two coherent beams, whose amplitudes and directions are

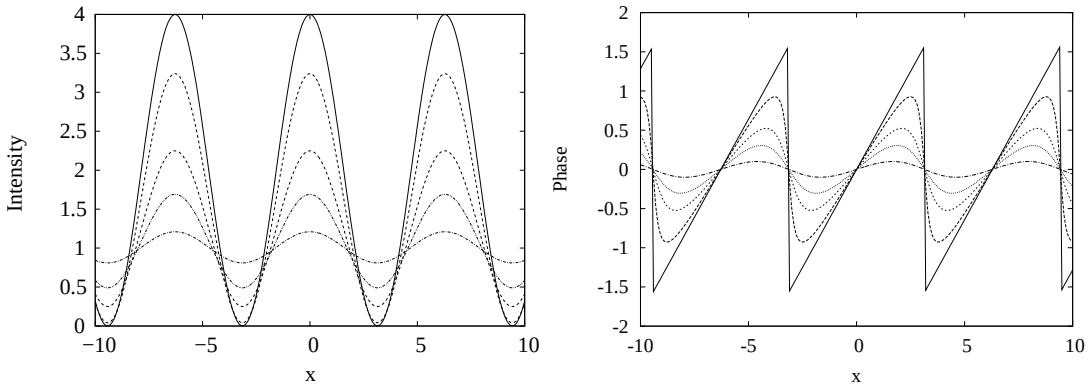

Figure III.9.: Intensity $\rho^2(x)$ (left) and phase $\phi(x)$ (right) profile for $k_1 = 1$ and $k_2 = 0$ from eq.III.11. The amplitude $A_2 = 1$ is kept constant, while A_1 increases ($A_1 = 0.1, 0.3, 0.5, 0.8, 1$) producing higher modulations in phase and amplitude.

controllable experimentally. In the simple hypothesis that the two beams are two plane wave, the angle they form with the optical axis is controlled by their transverse wavevectors k_1 and k_2, while their amplitude are A_1 and A_2. The total field on the transverse plane of the VCSEL is then the sum of the two fields $E = A_1\, e^{ik_1 x} + A_2\, e^{ik_2 x}$.

It is possible to write the total field E in terms of its amplitude and phase as $E = \rho\, e^{\,i\phi}$, defining the quantities

$$K = \frac{k_1 + k_2}{2} \tag{III.8}$$

$$\delta k = \frac{k_1 - k_2}{2} \tag{III.9}$$

In this way the amplitude ρ and phase ϕ of the total field along the transverse direction x are given by

$$\rho(x) = \sqrt{4\, A_1\, A_2\, \cos^2(\delta k\; x) + (A_1 - A_2)^2} \tag{III.10}$$

$$\phi(x) = \mathrm{atan}\left[\frac{A_1 - A_2}{A_1 + A_2}\, \tan(\delta k\; x)\right] + Kx \tag{III.11}$$

The equation for the amplitude shows that the interference term is obviously controlled by the product of the amplitudes $A_1 A_2$, while the spatial frequency by the difference δk of the transverse vectors. The interference fringes have then a constant component given by the difference $(A_1 - A_2)^2$, i.e. the contrast is maximum when the two beams have equal intensity, otherwise it decreases.

The simplest case is when both beams are normal to the VCSEL, so the transverse wavevectors are zero, $k_1 = k_2 = 0$. In this case the total amplitude is simply the sum of the two amplitudes along x ($\rho = A_1 + A_2$) and the phase profile is flat ($\phi = 0$).

If now we consider the beam A_1 tilted in respect to the beam A_2 ($k_1 = 1$, $k_2 = 0$), then the phase and amplitude profiles become modulated. In fig.III.9 we show the ρ and ϕ profiles for different amplitudes A_1 in the case $k_1 = 1$, $k_2 = 0$ (that will be useful for the experimental observations of sec.III.3). The contrast of the intensity modulation ρ^2 increases with A_1 approaching to A_2, while the phase modulation grows from zero to $\phi(x) = Kx \pmod{\pi/2}$ when $A_1 = A_2$. So when the two beams have the same intensity the phase gradient is simply given by the non-zero transverse wavevector of the tilted beam, that can be measured directly in the near field finding the transverse frequency of the fringes. Increasing the amplitude of A_1 from zero to A_2, is then equivalent to increase the phase and intensity gradients along x.

III.3.2. General behavior

As the holding beam passes through the interferometer, and its phase profile is flat on the VCSEL plane, in the far field one can observe two small bright spots, each corresponding to the injection of one arm of the interferometer. We indicate these two beams, and their corresponding points in the far field, with the labels A and B (see fig.III.10). We fix the alignment of beam A (in absence of beam B) to be on-axis. This allows to observe stable solitons in the near field of the VCSEL. Then we inject beam B and we create vertical intensity fringes in the near field. This corresponds to a small (horizontal) misalignment in the far field of the two points A and B, as in fig.III.10 (bottom).

As it can be seen in the images, the positions of the localized structures along the fringes in the near field changes with the position of the point B in the far field. Aligning point B at left of the zero defined by the point A, induces positions in the near field tilted to the left with respect to the center of the fringes. On the other side, if point B is at right of the zero of the far field, then the structures in the near field are "pushed" towards the right of each fringe.

Points A and B are the Fourier transformed of the two beams coming from the interferometer, and a misalignment of them in the far field means a different angle of incidence on the VCSEL plane. As discussed in sec.III.3.1, in a plane wave approximation this means that the beam B is responsible for a phase gradient on the plane of the VCSEL, along the horizontal direction. In the case of fig.III.10, the relative phase of the two beams has a variation of π every $\simeq 30\,\mu$m along the direction perpendicular to the fringes (to give easily an estimation we consider equal intensities). Then we can estimate the phase gradient of the order of 0.1 rad/μm and an angle of about 0.02 rad between beams A and B. On the other hand the interference creates intensity fringes. The maximum intensity gradient is quite strong because the two arms of the interferometer have similar intensities (the modulation has an amplitude of 90% of

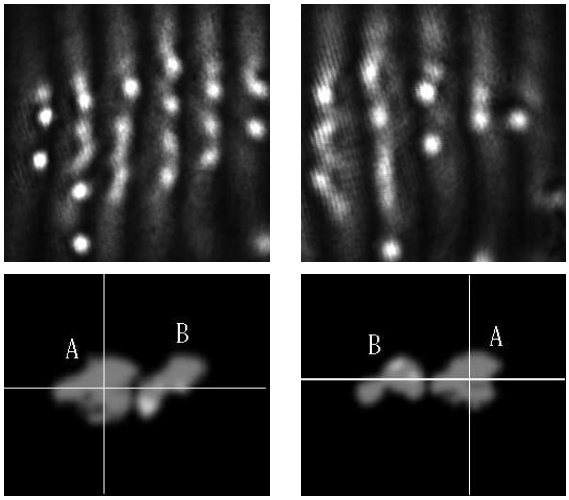

Figure III.10.: Near field (top) and respective far field (bottom) images of the VCSEL (250 μm diameter) using as injection the two coherent beams A and B coming from the interferometer. The cross in the far field indicates the direction of beam A, which is chosen normal to the VCSEL surface, i.e. giving the origin of the transverse plane. The sign of the angle of incidence of B changes from right to left.

the maximum value, estimated of the order of 10^4 mW/cm^2).

The observations can be interpreted as follows. The structures are at rest and the only parameter changed is the sign of the phase gradient, so what we observe are the stable positions of the structures due to the compensation between phase and intensity gradients. The overall result is a shift of the equilibrium point of the localized structures inside the bright fringes, along the direction and orientation defined by the transverse vector $\overrightarrow{AB}$ in the far field plane. We can roughly estimate that the magnitude of the intensity gradient that each soliton experiences in its position is of the order of 10% of the maximum amplitude for every micron (10^3 mW/(cm^2 μm)). Neglecting for the moment the effect of cavity defects, as the solitons are at rest, the effect induced by the intensity gradient should equal that of the phase gradient. This gives the order of magnitude for both modulations when their effects (i.e the velocities they produce) over the solitons are equal: $\nabla\phi \simeq 0.1$ rad/μm and $\nabla I \simeq 10^3$ mW/(cm^2 μm).

The observed behavior changes injecting the beams A and B with the same but opposite angle with respect to the normal, as in fig.III.11 (left). In this configuration the far field origin is in the middle between the two points A and B. The phase profile of the total injection is then flat and the phase gradient is zero (see sec.III.3.1). Under these conditions we observe that the positions occupied by the localized structures

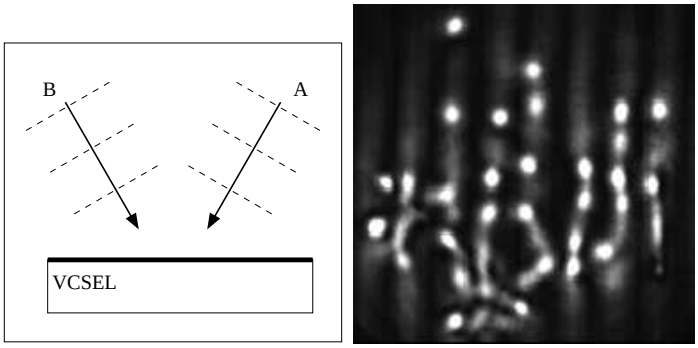

Figure III.11.: *Left:* scheme of the injection for which the phase gradient is zero. Both beams have the same but opposite angle with respect to the axis. *Right:* near field of the VCSEL. The structures occupy the center of the fringes, where the intensity gradient is also zero.

correspond globally to the center of each intensity fringe where the intensity gradient is also zero, as in fig.III.11 (right).

These observations, made in stationary conditions, are in agreement with the theoretical prediction that cavity solitons should experience a force (and a velocity) proportional to, and directed as, the phase and intensity gradients in the injection field. Here, controlling these gradients, we could put in evidence their effects on the equilibrium positions. In fact we have seen that, when a positive phase gradient is present, the stable positions of the structures are found where a negative intensity gradient is able to compensate it (fig.III.10). When the applied phase gradient is zero, the equilibrium is at the positions where the intensity gradient is also vanishing (fig.III.11). This describes the general behavior observed, but the details of the displacement of each soliton may change for different transverse region of the laser, mostly due to imperfections pinning the structures, as we will see in the next section.

III.3.3. Effect of imperfections

In the previous section we have neglected the effect of imperfections over the solitons. These are intrinsic to the semiconductor cavity or can be present in the injected field, and their effect should be taken into account together with the external gradients. In the following we will try to explain the observations considering that three kinds of forces can act over the soliton: defects, phase and intensity gradients. Other types of gradients can possibly exist, especially long range gradients due to the temperature or current profile for example. Their effect, if any, is superimposed to that of cavity imperfections.

We can identify the role of these three forces by the following experiment, described

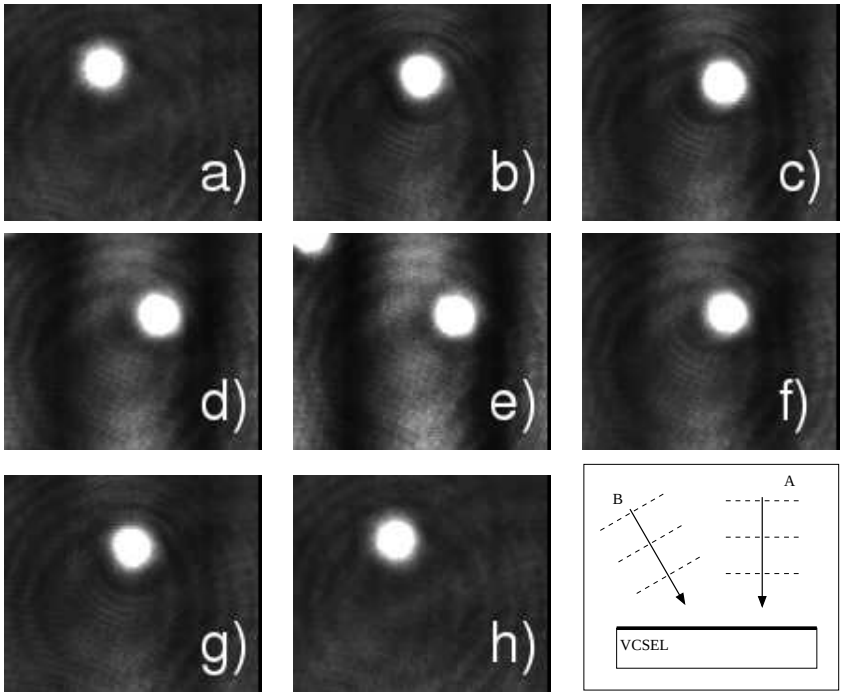

Figure III.12.: Detail of the near field of the VCSEL with double injection, as shown in the last picture. The intensity of B, tilted with respect to the axis, increases from a) (B = 0) to e) (B = 0.92 A) and decreases from e) to h) (B = 0), while the intensity of A is kept fixed. The horizontal direction is referred as x

in fig.III.12. We inject as in the previous section the holding beam in form of fringes, with one beam (A) from the interferometer taken normal to the VCSEL, while the other (B) forms an angle with the axis. We control now the intensity of B by means of a polarizer and a half-wave plate (HWP) inserted in arm B of the interferometer. As discussed in sec.III.3.1, increasing the amplitude of B (from zero to a maximum where A and B have similar intensities) increases both the amplitude and phase gradients. Therefore the position of the soliton, for every amplitude of B, will be that where all the forces, including defects, sum to zero.

In fig.III.12 all the positions of the soliton correspond to equilibrium points, and the soliton moves continuously with the change of the parameter (the intensity of B). Referring to fig.III.12, initially (.a) a soliton is spontaneously created by the on-axis injection of beam A alone. Increasing the amplitude of B, the phase profile tends to push the soliton to the right of the image. The intensity gradient seen by the soliton, for small amplitudes of B (.a - .b) has the same sign of the phase gradient, because the soliton initially is at left of the center of the fringe so the intensity force is towards

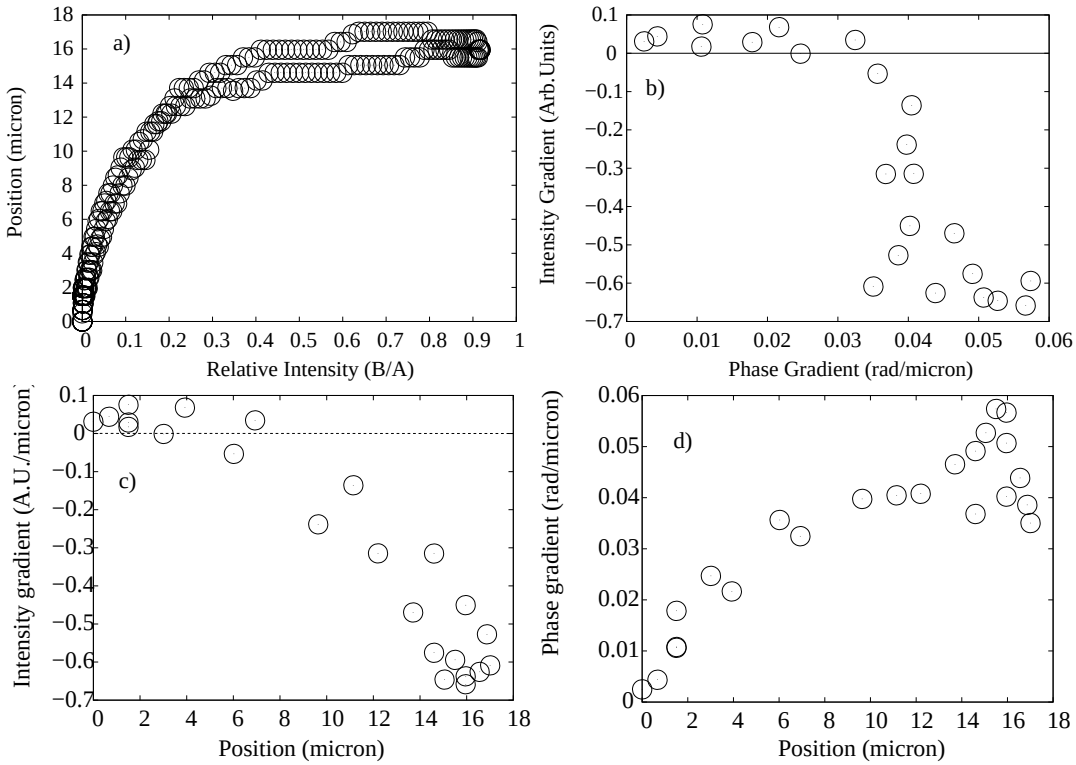

Figure III.13.: *Upper-Left:* Distance of the soliton from its original position (where no gradient is applied) as a function of the relative intensity of the two holding beams (A and B). *Upper-Right:* Intensity gradient versus phase gradient calculated at each equilibrium position of the soliton. *Lower-Left:* Intensity gradient seen by the soliton as a function of the distance from its original position. *Lower-Right:* Phase gradient seen by the soliton as a function of its distance from the original position.

the intensity maximum to the right. Increasing more the amplitude of B (.b - .d), the phase force becomes stronger and the soliton is pushed towards the right, passing through the center of the intensity fringe (.b), where the intensity gradient is zero. Here (.b) an equilibrium is not possible in such conditions (zero intensity gradient, non zero phase gradient) unless considering a force directed to the left due to imperfections. The effect of imperfections is also visible decreasing again the amplitude of B, in fact the soliton is pushed back to its original position (from .e to .h), that corresponds to the left side of the intensity fringe where both gradients are non zero for small amplitudes of B. Again, this would not be possible in absence of a third force due to defects.

In fig.III.13 the quantitative analysis of these measurements is shown. The position of the soliton (with respect to the position for B=0) is shown in fig.III.13.a as a

function of the relative intensity of the two beams (B/A). It results that the maximum displacement occurs for equal amplitudes, where the gradients are maxima. In fig.III.13.c and .d we plot the values of the intensity and phase gradients at each position of the soliton. For every amplitude of B, the intensity gradient at the position of the soliton is obtained from the intensity profile on the surface of the VCSEL, and the corresponding phase gradient is estimated using eq.III.11. In fig.III.13.b we plot the phase gradient at each position of the soliton as a function of the corresponding intensity gradient. In absence of imperfections and with a first-order linear effect of the gradients, this curve should be a straight line (with negative slope), because the position of the soliton is such that the applied forces always cancel. At equilibrium, in fact, one would have $\nabla\phi(x) = -\alpha\nabla I(x)$ with $\alpha > 0$ ($x > 0$ indicates the right of the images). In the real system this linearity is not observed: for small intensities of B the equilibrium is found where the intensity gradient has the same direction as the phase gradient.

Therefore, controlling phase and intensity of the injection we observe the soliton in stable positions where the two gradients do not cancel (for low amplitudes of B). Moreover, lowering the amplitude of B, the soliton is attracted back to its original position where the gradients are not zero for small intensity of B. This can be explained only by the presence of a third force, due to a defect, attracting the soliton at its original position. We can estimate the force of this gradient as follows. When the trajectory in fig.III.13.b crosses zero (at about 7 μm from the initial position, see fig.III.13.c), the soliton is at the center of the fringe, where the intensity gradient is zero. So there the effect of the defect should equal that of the phase alone, which has a value around 0.03 rad/μm.

This result demonstrates that in these VCSELs the combined action of the injection gradients can move the localized structures over a distance greater than their width, balancing the force of imperfections. An imperfection is then defined by the point of the VCSEL that corresponds to the original position of the soliton (when the injection is normal to the VCSEL), which acts as a source of an attracting gradient. Its effect can be experienced in an extended region around it: in the case of fig.III.12, a region of the VCSEL with extent to the right of about 20 μm attracts the soliton to the defect center, while at left of the imperfection the soliton cannot exist. This imperfection attracts and stabilize the soliton, but importantly its presence is not necessary for the soliton to exist. In this way using the interplay of two injected beams it could be in principle possible to draw a map of the VCSEL defects, as it is described in the following section.

III.3.4. Mapping the defects of the laser cavity

As defects in the laser cavities seems to be the most limiting factor (and the most difficult effect to overcome) in the practical development of a soliton based device, it is important to get an insight of their strengths and positions over the transverse plane of the laser. The aim of this section is to describe a simple method that we propose in order to get these informations from real systems. Hopefully this can be useful in visualizing the transverse homogeneity of devices supporting localized structures. In the practical operation with our devices, even if we can recover by this method the defects that we have already known, some limitations need to be discussed after its description.

In all the tested VCSELs we have found that some positions of the transverse plane are preferred for stable solitons, while others are always avoided. The former indicate pinning imperfections, the latter repulsive defects. In order to have a map of all these positions we propose a simple statistical analysis over the stable positions spontaneously occupied by solitons. We inject the two coherent holding beams coming from the interferometer as in fig.III.14.a: both wavevectors form the same and opposite angle with the optical axis. In this way the phase profile is flat, as discussed above, while intensity fringes are formed on the VCSEL plane by interference. When solitons are spontaneously formed, as the phase force is absent, they are confined by the intensity gradient perpendicularly to the fringe, while they are in principle free to move in the direction parallel to the fringe. The only force experienced along the fringes is due to imperfections in the medium and/or in the injection.

In fig.III.14.b we plot the output profile of the VCSEL with injection in form of horizontal fringes. We observe that the cavity solitons are organized along horizontal lines and ,if the holding beam is removed and reapplied, they appear always at the same positions along the injection fringes. This means that, inside each fringe, they are in stable positions defined by imperfections, which remove the translational invariance.

Using a piezoelectric element mounted to the back of the mirror in one arm of the interferometer, we can change the relative phase of the two beams on a wavelength scale. This makes the fringes shift slowly (about 1 μm/s) in the near field of the VCSEL, along the direction perpendicular to them, preserving the angle between the two beams (so also the size of the fringes and the flat phase profile). The soliton tends to occupy the stable position defined by the intensity maximum, where the force due to intensity is vanishing, so the slow shift of the fringe induces a displacement of the soliton. The motion of each soliton does not follow a straight line but complicated trajectories are observed, and solitons can also appear and disappear during the shift of the fringes. The stable positions inside the fringe are defined by the attracting defects present along the path of the soliton.

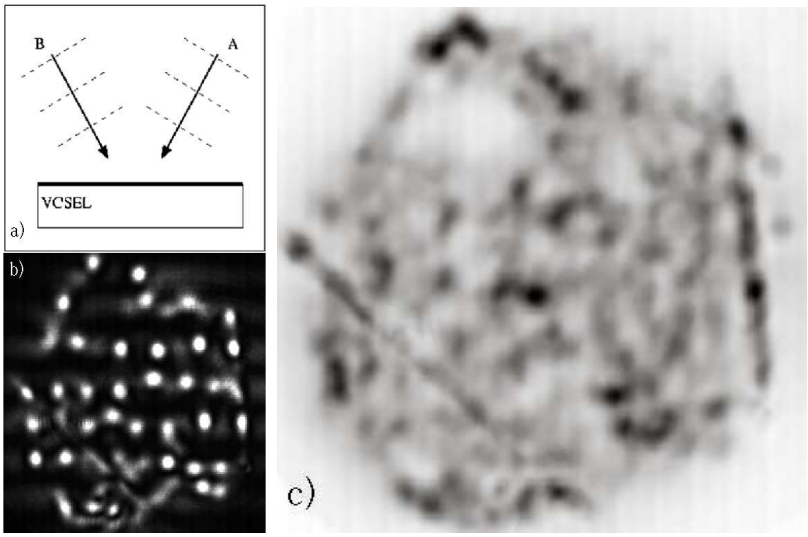

Figure III.14.: Mapping the roughness of the laser plane. *a)* Scheme of the injection for these measurements: the two coherent holding beams have the same angle with the optical axis, in order to have flat phase profile with intensity fringes. *b)* An example of near field of the injected VCSEL, where the fringes are horizontal and solitons present along them. The fringes are then shifted vertically. *c)* The result of the analysis described in the text. Black (white) regions correspond to pinning (repulsive) inhomogeneities.

Recording the movie of this motion along the whole transverse plane, summing and normalizing all the frames (which is the digital counterpart for keeping opened the shutter of analog cameras) one gets the trajectories chosen by each soliton while it is "pushed" by the moving fringes. Changing now the alignment of the two holding beams, this procedure is done again for many different directions of the fringes (covering $0 - 2\pi$), and finally all the frames are added and normalized again. In this way, statistically, solitons will track all the possible stable positions on the plane. The most visited points correspond to attracting imperfections, while the regions which are never visited will indicate the repulsive defects. It is important to note that the defects evidenced with this method correspond to the ones of the device and not to the ones of the injection, because the average on all the different alignments should cancel out the roughness in the injection beams.

The result of this analysis is shown in fig.III.14.c for the laser used also in fig.III.7, where a black color indicate the most visited regions of the plane (so attracting imperfections), while white corresponds to the avoided zones (so repulsive defects). In a perfectly flat laser this image would be homogeneously gray, indicating that all the

positions of the transverse plane have the same probability to host a soliton. Here on the contrary imperfections appear. The defects that were visible in fig.III.7 for different current values are recovered here in a single image, as the lines on the two sides and the white regions on the top of the image (where no interaction seems to exist in the soliton range of parameters).

A problem related to the presented method is the fact that it is strictly valid only when real independent solitons are involved and displaced along the intensity fringes. In our device it is not yet possible to observe solitons in the whole VCSEL surface for the same parameters, but bistable independent solitons may coexist with patterns where the correlation length is longer than the soliton size. If two structures are spatially coupled, then the equilibrium positions they will find is a complicated function of the parameters. Their positions affect the average, bluring the final image. So the simple method described above is not strictly reliable when correlated structures are present. However, even if in fig.III.14.b not all the structures are independent solitons, some indications of the VCSEL cavity defects can be recovered, as the main imperfections are well visible.

Figure III.15.: Holding beam in form of fringes.

III.4. Drift of localized structures

We describe in this section the experimental observations that can be interpreted as the motion of localized structures in the transverse plane of the injected VCSEL under the effect of stationary injection gradients. When using an injection profile which is homogeneous over the whole plane of the VCSEL, we have found quite difficult (even though not impossible) to observe the motion of a soliton in the transverse plane under the effect of gradients. In fact, injecting a slightly tilted plane wave, the trajectory followed by the soliton can be deviated randomly by all types of inhomogeneities of the system (as cavity and injection defects), making difficult the observation due to the fast time-scales.

Therefore we opted for the use of fringes that can guide the transverse displacement of solitons (as in fig.III.15). Fringes are created by the interferometer placed in the path of the injection beam, as in the previous section. The transverse size of the fringes is adjusted in order to fit completely the diameter of one soliton ($> 10\mu$m). Alternatively, another solution used was to use a cylindrical lens that reduces the size of the injected beam to one transverse dimension. Even if some interesting results were found in this latter case, this method is not very flexible since the injection parameters (amplitude and phase profiles) depend on the chosen lens together with its position.

With the use of intensity fringes, the conditions for the existence of localized structures are verified only in those regions of the transverse VCSEL plane where a sufficient level of injection occurs. When a soliton arises in those regions, it experiences a strong lateral confinement due to the intensity gradient perpendicular to the intensity stripes. Then its motion is possible only along the (linear) path defined by the fringe, where in principle the intensity profile is flat and the intensity gradient negligible. Detecting the local emission in different points along this path (using a set of fast

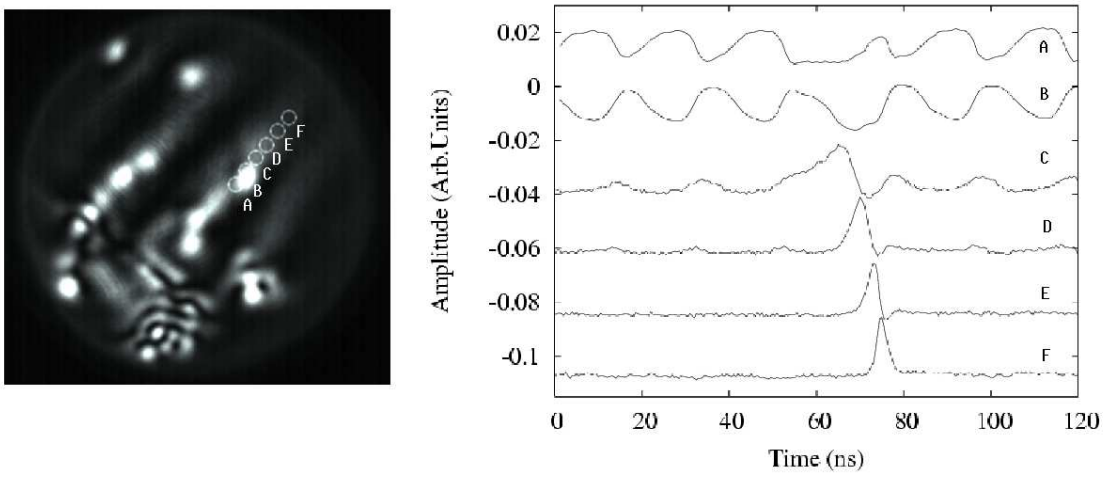

Figure III.16.: *Left:* near field of the VCSEL with the injection in form of fringes. The positions and sizes of the regions seen by the detectors A-F are marked as white circles. *Right:* corresponding temporal traces recored by the array of detectors. A constant offset shifts the traces for clarity. The bias current is 510 mA.

detectors), we could then observe time traces that suggest the displacement of peaks of intensity, in typical time-scales of ns (that are too fast to be observed by CCD cameras, that integrate over ms).

III.4.1. Results

The phenomenology experimentally found in our system is quite rich. We divide for clarity the description of the results in three parts.We discuss the observation of single shifting pulses which are randomly distributed in time in sec.III.4.1.1 and the transition to a periodic shifting regime in sec.III.4.1.2. The onset and drift of a single localized structure can also be optically triggered close to these region of parameters. This shows the feasibility of an optical shift register based on localized structures, and will be the subject of sec.III.4.3. The spatio-temporal dynamics observed is very sensitive to the parameters, rendering the experimental exploration and characterization difficult. Many details of the observations need to be further investigated but the motion of structures can be clearly identified.

III.4.1.1. Randomly activated shifting events

We inject the holding beam passing by the interferometer and we adjust the alignment in order to have the fringes as in fig.III.16 (left). The VCSEL current is 510 mA, and the total injected power is about 15 mW. We are interested in the central fringe on the VCSEL, where a localized structure is spontaneously formed. The positions and dimensions of the detectors are indicated on the image by white circles. They are adjusted parallel to the central fringe in order to have the bright structure between the first two detectors. Their recorded temporal traces (A and B in fig.III.16 right) show anti-phase oscillations of the local intensity (at about 100 MHz) where the structure appears. This seems to indicate that this structure is oscillating back and forth around an equilibrium point caused probably by a pinning defect of the VCSEL structure. More importantly, the other four detectors show that an impulsion starts to propagate towards the external part of the device. When this propagation is started (around $t = 65$ ns), the oscillations in the two upper detectors stop and restart after few ns. The amplitudes of the oscillations in the two first detectors and those of the escaping pulses have the same magnitude, suggesting the interpretation of one single moving localized structure. This kind of shifting events occurs randomly, or can be triggered by a mechanical perturbation.

Even if the origin of these oscillations is not clear, it is possible to interpret this observation as the motion of a localized structure which is weakly pinned by an imperfection of the system, and which is induced by a stationary holding beam profile. It is important to note that previous demonstration of the plasticity of CS [61] relied on the modification of the spatial profile of the injected beam in the course of time.

We remark that the behavior described above is only possible in very precise conditions of alignment, which are obtained by tilting the two holding beams coming from the interferometer with respect to the VCSEL axis. While this induces a phase gradient (which cannot be estimated here) along the intensity fringe defined by the holding beam, it also induces a radial intensity gradient. In fact, when tilted with respect to the VCSEL axis, the holding beam waist does not match anymore the VCSEL borders and homogeneity in terms of intensity is not assured. Indeed, in the direction of the fringe, the intensity of the injected beam decreases almost linearly from the maximum at the central region to the boundary of the laser (where its value is 40% of the central maximum). In the other direction, the amplitude modulation perpendicular to the fringes has an amplitude of 96% of the maximum. Therefore it is worth noting that the motion is done towards decreasing injected amplitudes: this would indicate that in this case the phase gradient, even if we cannot estimate it for these set of measurements, is more effective than the amplitude gradient, as the latter should induce a velocity opposite to that measured.

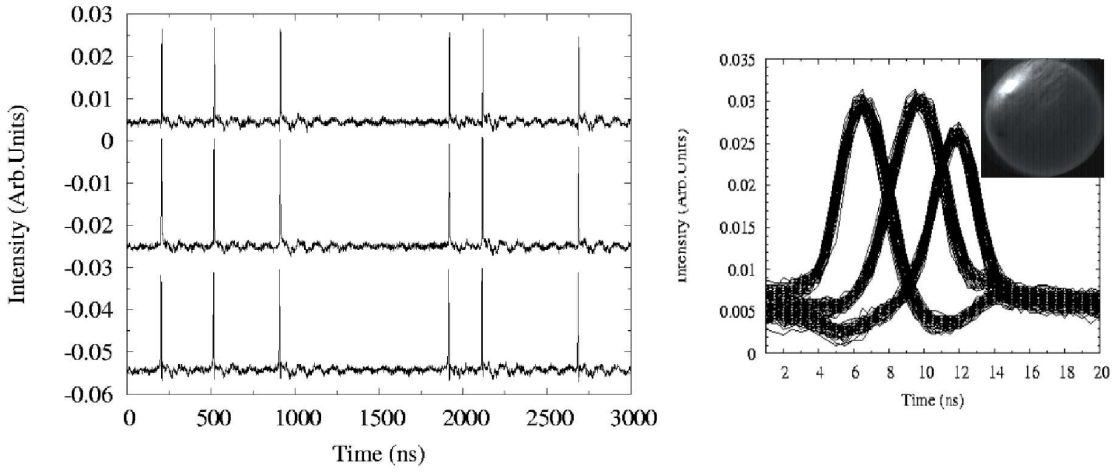

Figure III.17.: *Left*: time traces for 3 detectors along the injected line. A constant offset shifts vertically the traces for clarity. *Right*: superposition of 50 events on 3 detectors. The pulse propagates along the injected line with always the same shape and speed. The near field of the VCSEL is shown in the inset. The current is 441.72 mA.

In fig.III.17 we show a similar result observed in an other 200 μm-diameter device using a cylindrical lens instead of the interferometer in order to confine the injection along a line. The current is 441.72 mA and along the injected line the amplitude has a central maximum and decreases on the edges at a value of 30% of the maximum. The total injected power is again around 15 mW. In this case no structures are visible in the integrated image of the CCD camera in this region of parameters, but the observation of the time traces shows that a peak of intensity arises spontaneously (see fig.III.17 left) and escapes along the injection line immediately after its appearance, as indicates the delay of 3 ns between the peak measured by two consecutive detectors (see fig.III.17 right).

As before it seems that the pulses are originated randomly in time, but here a low amplitude modulation is visible in the traces of all the detectors. The origin and role of this global modulation is unclear: it appears after every high pulse, synchronously in all the traces, as a damped relaxation around 10 MHz and lasting few hundreds of ns. It can also appear without the generation of pulses, but it seems to participate in their excitation. In fact two subsequent pulses of a same trace are often found in correspondence of two local maxima of the small modulation. In this way we will see that, increasing the pumping current, in fig.III.17 the appearance of pulses becomes more frequent, and always synchronized with the small amplitude modulation. Finally

a periodic train of pulses is found for higher currents. This transition will be described more in detail in the following section.

A possible interpretation of this observation rely on the fact solitons in general can be switched-on by an addressing beam or they can appear spontaneously induced by the noise of the system when the parameters are close to the values for which the homogeneous solution looses its stability. Then, in this region of parameters, noise would be responsible for the switching-on of a soliton. Once created, the soliton drifts along the intensity channel, driven mainly by the phase gradient as discussed above.

Importantly, even if randomly activated, the motion of the structure is always identical, within the limits of our detection system (350 MHz, but we will see that it is sufficiently accurate), as shown in fig.III.17 (right). With stationary control parameters neither the delay between traces nor the shape of the peaks change, and the triggered traces in fig.III.17 can well be superimposed. This is also in agreement with the interpretation of drifting cavity solitons because the speed of the localized structure is determined by the external gradients, and its shape should be defined by nonlinearities of the system.

We can get an indication about the size of the moving structure from the following argument. In both cases presented above, the intensity recorded by the detectors corresponds to the value of the convolution between the drifting structure and the aperture of the detector on the near field (which is controlled by the imaging system). We observe pulses that do not saturate, not showing a clear top flat profile. This would indicate that the drifting structure and the recording area of each detector have comparable sizes (around 7-8 μm). This is of the same order of the waist of solitons at rest, giving another indication in favor of the interpretation.

Other randomly activated motions similar to those described in fig.III.16 and III.17 have been observed along several directions of space and for different devices (coming from the same wafer and with a diameter of 200 μm). These observations show that the inhomogeneities present in these improved semiconductor lasers are weak enough for the gradients of the holding beam to induce motion along the imposed direction along several tens of μm. The alignment of the injection and the VCSEL current level are critical parameters, rendering this dynamics quite difficult to find experimentally. We will see that the periodic regime that will be described in the next section can help in finding the good region of parameters.

III.4.1.2. Periodic regime

In both cases described in the previous section, a set of high intensity pulses is spontaneously created, indicating the drift of a localized structure triggered by internal mechanisms and noise. Here we describe the behavior of the system when the bias

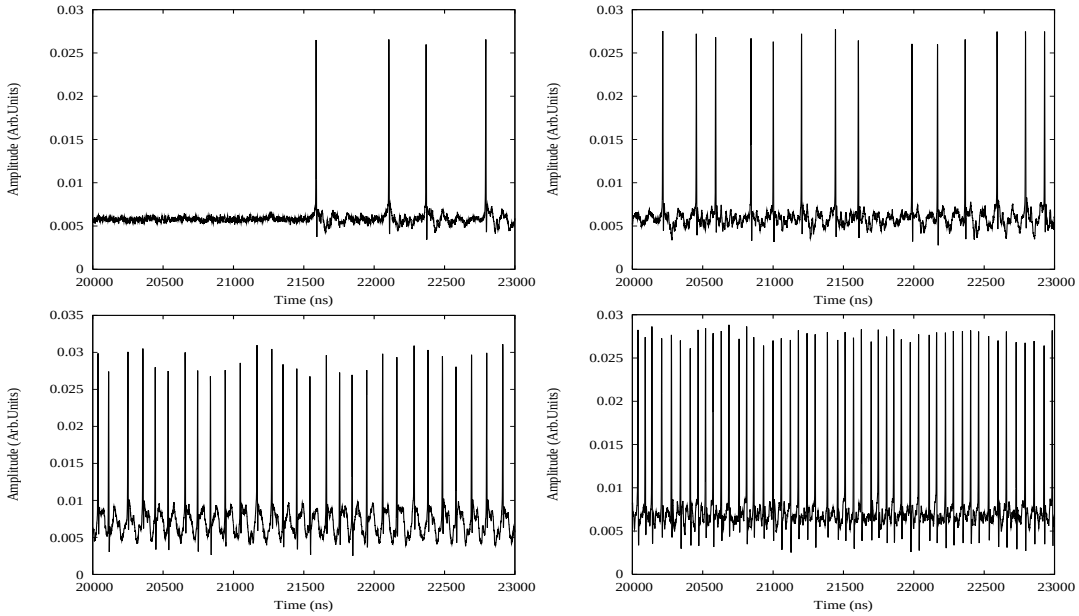

Figure III.18.: Time traces of the detector placed where the first pulse of the series shown in fig.III.17 grows. The VCSEL current increases from left to right, top to bottom, from 441.72 mA to 441.75 mA.

current is increased from fig.III.16 and fig.III.17. We will see that a periodic regime is attained in different ways.

We first describe the effect of the increase of current for the injection shown in fig.III.17. Referring to fig.III.18, for low currents (upper row, left) in each trace the pulses are rare and noise-triggered. Increasing further the bias current they become more frequent, and finally the signal of each detector becomes periodic. Here the small amplitude modulation, as discussed above, is present in the traces of all the detectors, and probably plays a role for the observed dynamics as a triggering mechanism. For higher currents, once the motion is periodic, the frequency increases slightly with current in a range of about 1 mA up to about 100 MHz (period of 10 ns), while the sequence of drifting remains the same (this means that the traces of two consecutive detectors show a periodic train of pulses with a delay of few ns between them). While two consecutive events approach continuously with increasing current, we do not observe a clear variation of the time between two consecutive peaks in two consecutive detectors when the current is increased. This means that once the motion is activated, the speed of the structures does not change appreciably within this small region of current, at least within our temporal resolution of 350 MHz.

In fig.III.19 we plot the mean value (continuous line) and the standard deviation (dashed line) of the time interval between two consecutive pulses in the same trace. Noise seems to drive the dynamics for low currents (441.7 mA), where groups of

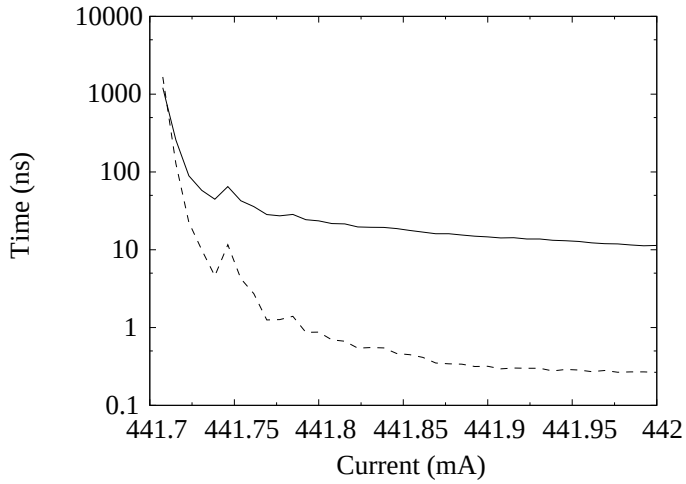

Figure III.19.: Statistics of the time between two consecutive peaks in the trace of the same detector (detector A of fig.III.22). *Continous line:* mean value. *Dashed line:* standard deviation.

pulses, probably coupled by the small amplitude modulation, are separated by many μs. Here the standard deviation is of the same order of the mean value, indicating the main role of noise as switching-on mechanism (but the statistics are calculated for a low number of events in this region because of the large time intervals). For higher values of current the traces become periodic, the number of events grows and the mean value (which gives now the period) decreases down to about 10 ns while the standard deviation is reduced to few hundreds of ps (the digital limit of our resolution is 500 ps). Increasing more the current, an abrupt transition to a stable emission profile is observed, where no oscillations are present, indicating subcriticality.

The smooth transition to a periodic regime as described above was found also for other directions of the injection and in different devices. However this is not the only possible transition to this regime. In fact, we have found that, starting from the situation shown in fig.III.16, an increase of the bias current makes the system subcritically jump to the periodic drifting. Increasing the current from 510 mA to 512 mA, the system abruptly changes its near field and the time trace of each detector becomes periodic, as shown in fig.III.20. A further increase of the current has the effect of increasing the frequency of the periodic signals, very similarly to what shown in fig.III.19. Around this transition region hysteresis is observed between the two solutions (i.e. the periodic regime and the pinned structure giving random shifting events described in fig.III.16).

From the experimental point of view the presence of such periodic regimes helps the identification of the good parameters where motion appears. In fact exploring the system the more accessible information is given by the integrated CCD images.

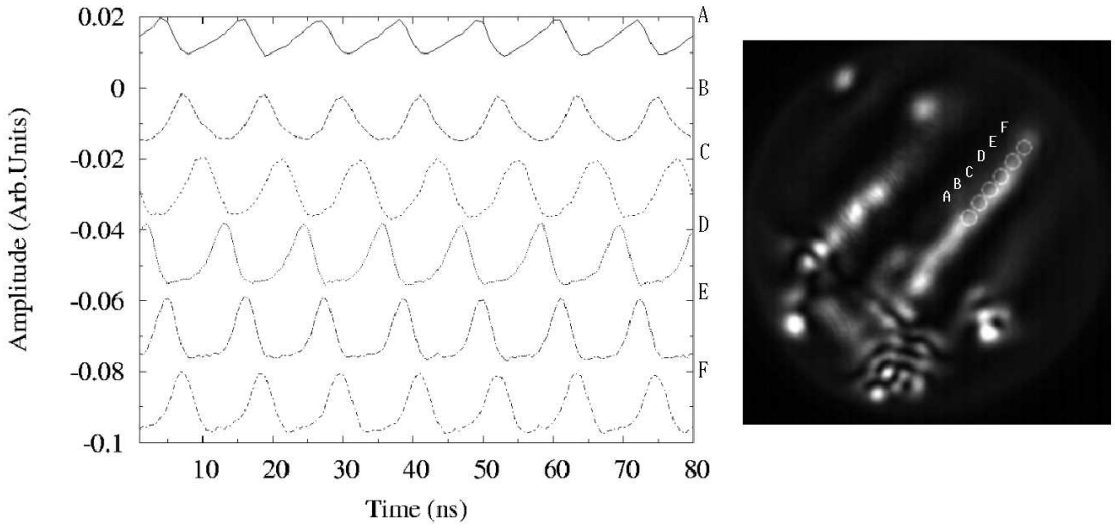

Figure III.20.: Periodic spontaneous regime. *Right:* near field of the injected VCSEL. The injection is made of interference fringes and the positions of the detectors are the same as in fig.III.16. *Left:* time traces of the array of detectors. Each trace is vertically shifted for clarity. The current is 512 mA.

When rare pulses are randomly triggered nothing is visible in the near field of the VCSEL. On the contrary the periodic regime is well visible as a bright stripe as in fig.III.20 (right). Experimentally this is the signature that motion along the injected line is possible.

Finally, in order to further confirm the interpretation of drifting structures, we could increase the bandwidth of the detection system up to 6 GHz and observe the pulses emitted by the system. We use a 8 GHz (Thorlabs PDA8GS) fiber coupled detector in combination with a 6 GHz oscilloscope (Lecroy WM8600A) at the place of the array of avalanche photo-diode detectors (350 MHz). In this way we can monitor the emission of a single region of the VCSEL with diameter less than 7 μm with a temporal resolution of 50 ps/point. We show the result in fig.III.21, where we have fixed the parameters in the region of periodic pulses, but the result is the same when randomly activated pulses are present. The fast detector used here has less sensitivity than the APDs used before, so the signal to noise ratio decreases. Anyway it is important noting that no temporal structures are visible inside a pulse at high frequencies up to 6 GHz, confirming the interpretation of a moving peak of intensity. Moreover this measurement indicates that the bandwidth of 350 MHz used in the previous measurements gives a sufficiently accurate description of the dynamics.

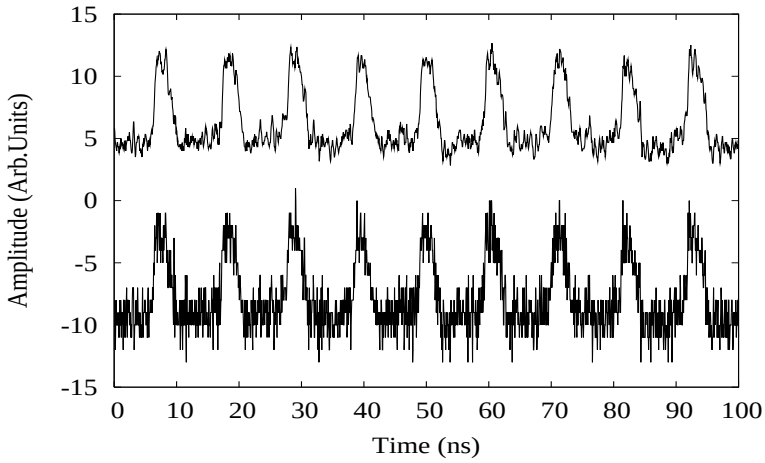

Figure III.21.: *Lower trace:* temporal detection of the periodic regime with a bandwidth of 6 GHz. *Upper trace:* smoothed trace using the convolution of the detected signal with a unitary vector of 6 elements (every point of the trace is replaced by the mean value of the signal calculated over 6 points around it).

III.4.2. Discussion

We have described the phenomenology of the injected VCSEL when one transverse degree of freedom of the solitons is eliminated using an interferometer or a cylindrical lens in the injection path. Similar results were found in different devices and for many directions on the VCSEL plane. The system exhibits a rich spatio-temporal dynamics with strong dependence over the parameters. We have observed noise-driven regimes where a single structure moves along the injection gradients, and a smooth or subcritical transition between these randomly activated pulses and a periodic regime.

When this transition does not happen subcritically, the presence of a small amplitude modulation seems important, even if its role needs to be clarified. Summarizing this case, increasing the parameter (in a small range of less than 1 mA, with DC level of 440 mA) we have observed (see fig.III.18):

1. for low current, a region where the ignition of the drifting peak is due to the internal noise, so the motion along the gradient is randomly activated while itself remains deterministic;

2. for higher currents, these random events become more frequent and the signal of each detector periodic with increasing frequency and with constant delay indicating constant velocity;

3. a constant emission attained by a subcritical transition.

It is interesting to note that the above sequence reminds the behavior of the injected VCSEL in standard conditions, when no gradients are present in the holding beam and when the structures are stable. In such conditions, increasing the bias current of the VCSEL, one observes initially single localized structures, then patterns that have transverse length decreasing with increasing parameter. If these stable structures could drift under the effect of external gradients, a sequence similar to the one described above would be observed: for low current single drifting solitons switched-on by internal noise, and for higher currents a periodic train of drifting pulses whose frequency increases as a function of the parameter. This intriguing similarity is just qualitative, because the orders of magnitude of the current intervals do not match. In fact, in the case of the patterns shown in fig.III.7 the current range is of the order of 100 mA, while the variations in fig.III.19 are less than 1 mA.

III.4.3. Optical delay line

One possible practical application of a soliton-based optical device is the all optical capability of shifting in the space bits of information. This feature is know in general as shift register, and here we demonstrate that in principle it is feasible in our system.

In digital circuits a shift register is a group of registers set up in a linear fashion which have their inputs and outputs connected together in such a way that the data is shifted down the line when the circuit is activated [93]. In our system we can transform a serial input into a parallel output, using the properties of localized structures moving under the effects of injection gradients. A soliton can be switched-on in one point of the plane of the VCSEL by the optical input bit given by the writing beam, and then it can drift along the injection gradients. All along the path followed by the soliton one can retrieve the optical input bit placing a detection system, which means that the serial input information is distributed in a parallel optical output line with some delay that in principle depends on the speed of the structure.

Here we demonstrate the possibility of optically induce the switching-on of a single localized structure inside an injection profile that produces the drift of the structure. Once the optical perturbation that induces the onset of the soliton is removed, we observe a drift along the injection gradients over distances of many tens of μm (which corresponds to many soliton diameters) in tens of ns, i.e. speed greater than 10^3 m/s. As we do not have at the moment the possibility of fine tuning the injection parameters, the speed of the structure is not easily variable experimentally. It will be very interesting and important in the future testing the possibility to control this velocity by means of the imposed gradients in the injection beam.

We fix the parameters as the ones for which fig.III.17 was found. Lowering the bias current of the VCSEL (less than 1 mA while the DC level is around 442 mA), the

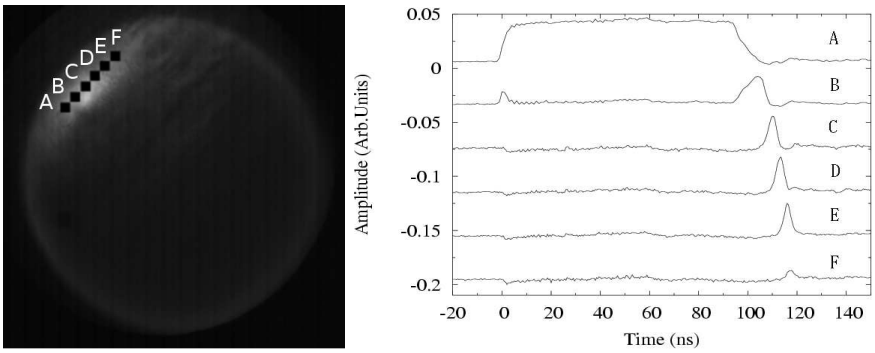

Figure III.22.: *Left*: near field of the VCSEL, with injection on a line given by the cylindrical lens. The positions and sizes of the detectors are indicated by the black squres. *Right*: Corresponding temporal traces of the detectors. A constant vertical offset shifts the traces for clarity. The writing beam pulse is addressed on the detector A. The structure then moves from A (upper trace) to F (lower trace). Current: 441.7 mA.

noise-triggered events become rare and finally disappear. In this limit region where they are absent, we found that the local optical perturbation, given by the pulsed writing beam, could trigger the switching-on and motion of one structure. This can be interpreted by the following argument: decreasing the pumping parameter decreases the effectiveness of the noise acting as ignition mechanism (always keeping the system in the region where solitons exist), then the switching-on threshold can be achieved by the optical perturbation.

Experimentally we use the writing beam with modulated amplitude by the EOM (see sec.III.2) as input bit. Because of technical limitations the duration of this perturbation is fixed to 100 ns (with rise and fall time less than 1 ns) and the repetition rate is fixed by the EOM driver at 10 KHz. The result is presented in fig.III.22. The writing beam is addressed in point A where the first detector is placed. The observations indicate that the first effect of the perturbation is to locally trigger the ignition of a cavity soliton (trace A). Once the writing beam is removed the soliton is free to move along the imposed direction under the action of phase and/or intensity gradients of the holding beam. The motion is monitored following the passage of the structure in front of the series of detectors. In this case, the cavity soliton drifts up to the detector E, and vanishes rather abruptly when arriving on the detector F. The result shown in fig.III.22 constitutes a demonstration of an all-optical delay line, since a bit of information applied at point A can be recovered at point E after a delay of about 10 ns. Since the distance on the VCSEL plane between two detectors is of 8.9 μm, the soliton drifts over about 45 μm and we can estimate the speed between points

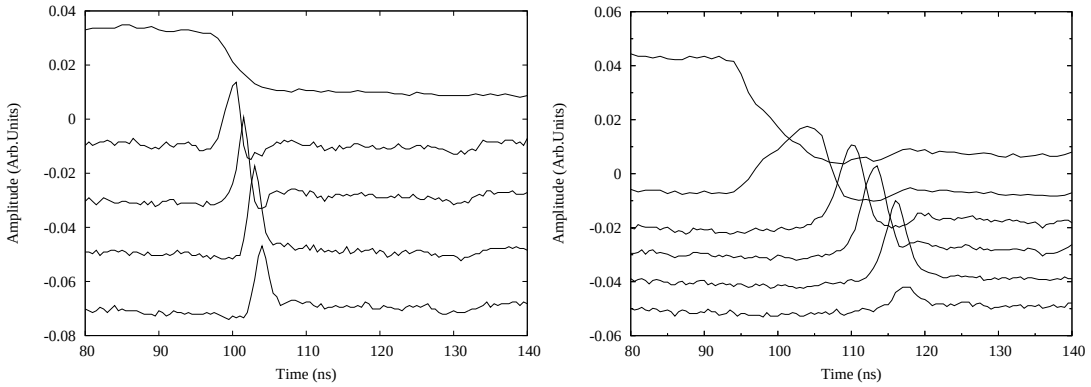

Figure III.23.: Two similar results found in two different devices of 200 μm diameter. *Right*: this is a zoom of fig.III.22(right). The speed of the structure is around 2.1 μm/ns, the current is 441 mA. *Left*: same as before but in another device under different injection parameters. Here the speed is around 9.6 μm/ns and the bias current 484 mA.

C and E of fig.III.22 (right) about 2.1 μm/ns. This confirms that the effect of cavity imperfections can be overcome by external gradients and that the presence of defects is not necessary for the existence of cavity solitons.

In fig.III.23 we compare the previous result (right) with a similar observation obtained in another identical device (left), focusing on the interval of time where the structure escape along the gradient. The current in the latter case (left) is 484 mA, and the speed of the structure is higher than the previous one, estimated around 9.6 μm/ns. Even if we cannot at the moment study the relationship between velocity of the structure and variations of the gradient, this measurement demonstrates that the observed behavior is general and gives an indication that under different injection conditions, the speed of the localized structure can change. Of course the fact that these results are found in two different devices does not allow us to indicate the difference in injection gradients as the only mechanism responsible for the difference in speed. There are for example theoretical indications [94] that the speed depends also on the carrier lifetime of the laser, however as the two lasers come from the same wafer, this parameter should be very similar (because in order to change it an involved engineering of the band gap is needed).

III.5. Control of localized structures position by means of external gradients

We have seen that the control of the motion and/or of the position of the localized structures depends mainly on the practical ability in manipulating the phase and amplitude of the injected beam. In the previous section we could not generate an arbitrary gradient profile in the holding beam, nor we could separate the contribution of the two gradients. Here we describe the experimental system that successfully gave us the possibility of an arbitrary injection profile. Then the separation of phase from amplitude modulations is possible and we can arrange a set of localized structures in a predefined configuration.

In the following we will describe the substantial changes in the experimental setup necessary in order to control the phase and amplitude profile of the holding beam. Then we will show results obtained with a controlled modulation of the injection phase and amplitude. In the last part we will show that a modulation of phase alone is able to fix the position of the solitons.

III.5.1. Experimental Setup

We use as a spatial modulator for the holding beam a liquid crystal light valve (LCLV) in conjunction with a twisted nematic liquid crystal display (LCD). Unfortunately we are obliged to use both of them together because the LCD (which normally can be used alone as a spatial modulator) is not efficient at the wavelength of the VCSEL (980 nm).

The idea is to use the LCLV ability to change locally its index of refraction, in order to modulate the transverse phase and/or intensity distribution of the incident beam that will be used for injection into the VCSEL. A modification of the index of refraction of the valve can be coupled with a rotation of the polarization of the incident beam. In this case an amplitude modulation can be achieved putting a polarizer at the output of the valve. Otherwise only the phase will be affected. The arbitrary index modulation is brought to the LCLV by a beam (at $\lambda = 658$ nm) passing by the LCD. This works as a normal computer display once it is positioned between two crossed polarizers. Then the image created on a computer is converted by the system in a phase and/or amplitude modulation of the holding beam.

III.5.1.1. The liquid crystal light valve

Liquid crystals are anisotropic media whose molecules have an elongated shape. Large cells (cm^2) of liquid crystals can be created and the orientation of molecules can be

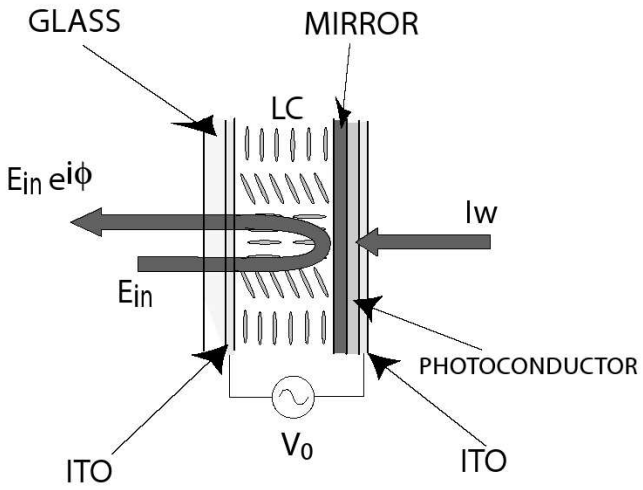

Figure III.24.: Scheme of the Liquid Crystal Light Valve (LCLV).

partially ordered. In the nematic phase, at the base of our device, molecules are in average aligned along one direction which defines the vector $\hat{n}$, called director of the liquid crystal. The ratio between the length and width of a molecule is quite large. Indeed, the typical dimensions of a liquid crystal are 20-40 Å in length and 4-5 Å in width. Birefringence of the medium is given by the difference in index of refraction between the direction parallel to $\hat{n}$ (the extraordinary index is $n_e = n_{//} \simeq 1.7$) with respect to the direction perpendicular to $\hat{n}$ (the ordinary index is $n_o = n_{\perp} \simeq 1.5$).

The Liquid Crystal Light Valve, as shown in fig.III.24 [95], is formed by a liquid crystal layer in between a glass and a photo-conductive plate over which a dielectric mirror is deposed. The liquid crystal is planar aligned, and the cell thickness is usually few tens of μm. Transparent electrodes (ITO) covering the glass plates permit the application of an external voltage V_o across the LCLV (chosen alternate in order to avoid a net drift of the molecules). The photo conductor behaves like a variable impedance, its resistance decreasing when increasing the intensity of the light I_w impinging on the rear side of the LCLV. Thus, the total root mean square voltage V_{LC} that effectively drops across the liquid crystals is directly proportional to the applied electric voltage V_o and to the optical intensity I_w arriving to the rear of the valve.

Under application of the effective voltage V_{LC}, the liquid crystal molecules reorient towards the direction of the electric field [96]. This happens at the Fréedericksz transition [97][96], when the torque due to the electric field is higher than the effective internal forces. For high values of V_{LC} the liquid crystals reorient perpendicularly to the glass windows (homeotropic alignment) and the response saturates when all the molecules are parallel to the applied electric field. In absence of voltage the elastic

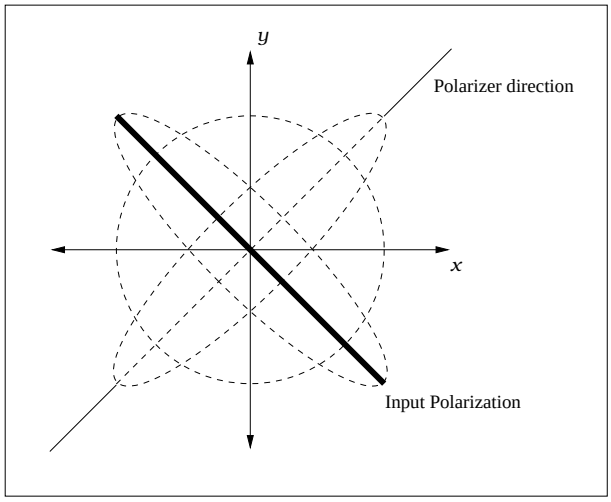

Figure III.25.: Scheme of the output polarization states (dashed lines) as a function of the phase shift between the vertical and horizontal component, when the input linearly polarized field (thick line) enters in the valve at an angle of 45^o with respect to $\widehat{n} = n\widehat{y}$. If a polarizer is used perpendicular to the input polarization, the amplitude modulation is possible.

forces internal to the liquid crystal reorient again the molecules parallel to the glass windows. The molecular orientation is then reversible.

The input beam, which passes through the liquid crystal layer and is reflected by the dielectric mirror of the LCLV, undergoes to a phase shift that depends on the applied voltage V_{LC}. It is useful to decompose the incoming electric field in the directions parallel and perpendicular to the crystal director. Under the effect of V_{LC} the molecules rotate in average on the plane defined by $\widehat{n}$ and $\widehat{z}$ (the propagation axis), so this reorientation induces a refractive index change only for the component of the input field parallel to $\widehat{n}$, depending on the voltage V_{LC}. In other words the extraordinary index n_e is a function of the effective voltage V_{LC}. On the contrary, the component perpendicular to $\widehat{n}$ does not see any change of the index, because the reorientation of the molecules is on a plane perpendicular to it. As a result, the component of the input beam parallel to $\widehat{n}$ undergoes a phase shift with respect to the component perpendicular to $\widehat{n}$. This phase shift ultimately depends on the light intensity impinging on the photoconductor, I_w, and on the electric voltage applied to the valve V_o.

If the input (TE) beam is now linearly polarized, as in fig.III.25, at an angle of 45^o with respect to $\widehat{n}$ (that we fix to be vertical with respect to the table), then the output polarization state depends on the effective voltage V_{LC}. In fact a phase shift of the vertical component with respect to the horizontal one, gives rise to a different output

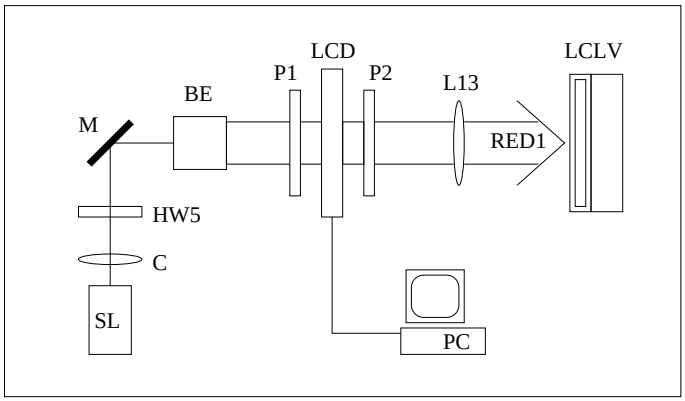

Figure III.26.: Experimental setup: spatial modulation $I_w(x, y)$ (RED1) of the beam at $\lambda = 658$ nm for the rear side of the LCLV.

polarization (from circular to linear $\pi/2$-rotated). Using at the output a polarizer perpendicular to the input polarization, the phase shift is converted in amplitude modulation.

If instead the polarization of the input beam is parallel to the molecules, then only its phase is varied, spatially (along x and y) modulated according to the distribution in the transverse plane of the voltage V_{LC}. This effective voltage in fact depends on V_o, which is constant on the plane of the valve, and on $I_w(x, y)$ which on the contrary can have any spatial profile. Therefore, modifying the spatial profile of the intensity $I_w(x, y)$ impinging on the rear side of the LCLV, is then possible to modulate with an arbitrary profile the phase or intensity of the input beam E_{in}. For our system, we find that intensities I_w of the order of 0.1 mW/cm^2 saturate the response of the valve which allows for maximum phase differences of the order of 2.5 rad ($\simeq 0.8\pi$) when $V_o \simeq 2.2\, V_{pp}$ (9 KHz).

III.5.1.2. The twisted nematic liquid crystal display

As shown in fig.III.26, we use the light coming from a semiconductor laser (SL) emitting in the visible red region ($\lambda = 658$ nm) to create the modulation $I_w(x, y)$ for the rear side of the LCLV, that will be converted in phase modulation for the holding beam. The collimated beam of SL is expanded by a beam expander (BE) and it is sent through the liquid crystal display (LCD) between two crossed polarizers (P1, P2). The polarization is turned (by the half waveplate HW5) in order to be parallel to P1. Every pixel of this device is driven by the voltage coming from a standard computer as for a normal display (1024x768 pixels). In absence of voltage across the pixel, the anchorage to the glass walls makes the molecules to form one or more spirals (twisted nematic anchorage), as in fig.III.27 (left). As the thickness of the device is

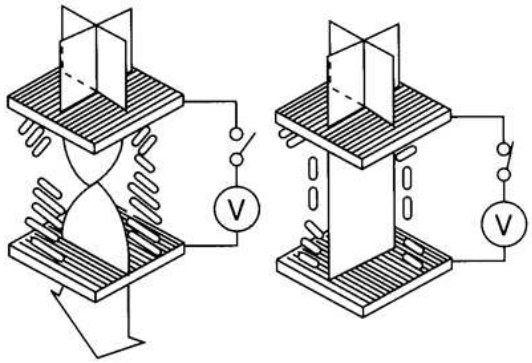

Figure III.27.: Scheme of the twisted nematic liquid crystal display, in absence of the external voltage (left) light can cross the device, with applied voltage (right) light is absorbed.

much longer than the wavelength (Mauguin condition [96]: $\lambda \ll (n_e - n_o)P_{hx}$, where P_{hx} is the length of the spiral), the spiral of liquid crystals acts as a waveguide for the incoming field. In this way the output polarization is turned by 90^o with respect to the input, and the use of the two crossed polarizers (parallel to the input and output anchorage respectively) allows in this situation the passage of the light.

When a voltage is applied across the pixel (above the Fréedericksz transition), the spirals are destroyed (but the process is reversible because of elastic forces) by the reorientation of the molecules as in fig.III.27 (right), and the polarization is no more turned. The output polarizer then prevents the passage of the light. As a function of the applied voltage (which has 255 levels) the intensity of the output light can be varied accordingly. In this way we can generate the spatial modulation for the LCLV simply generating on a computer the suitable image. Finally the lens L13 makes the image of the display LCD onto the rear side of the LCLV, supplying the intensity distribution $I_w(x, y)$.

III.5.1.3. Injection of the modulated holding beam

We can describe now the modifications of the injection system once the LCLV is inserted as a spatial modulator of the holding beam. The differences can be evidenced with respect to fig.III.4. The setup used in the following is shown in fig.III.28.

The holding beam HB2 is spatially filtered by the Fourier filter L7-PH30-L8 and is sent to the LCLV that is placed in one arm of a Michelson interferometer. The rear side of the LCLV is enlightened by the beam RED1 described in fig.III.26, changing the effective voltage profile on the plane of the valve. The beam splitter CBS preserves the polarization, and the director $\hat{n}$ of the liquid crystals is fixed vertically. The polarization of the beam arriving on to the LCLV (which is linear and vertical with

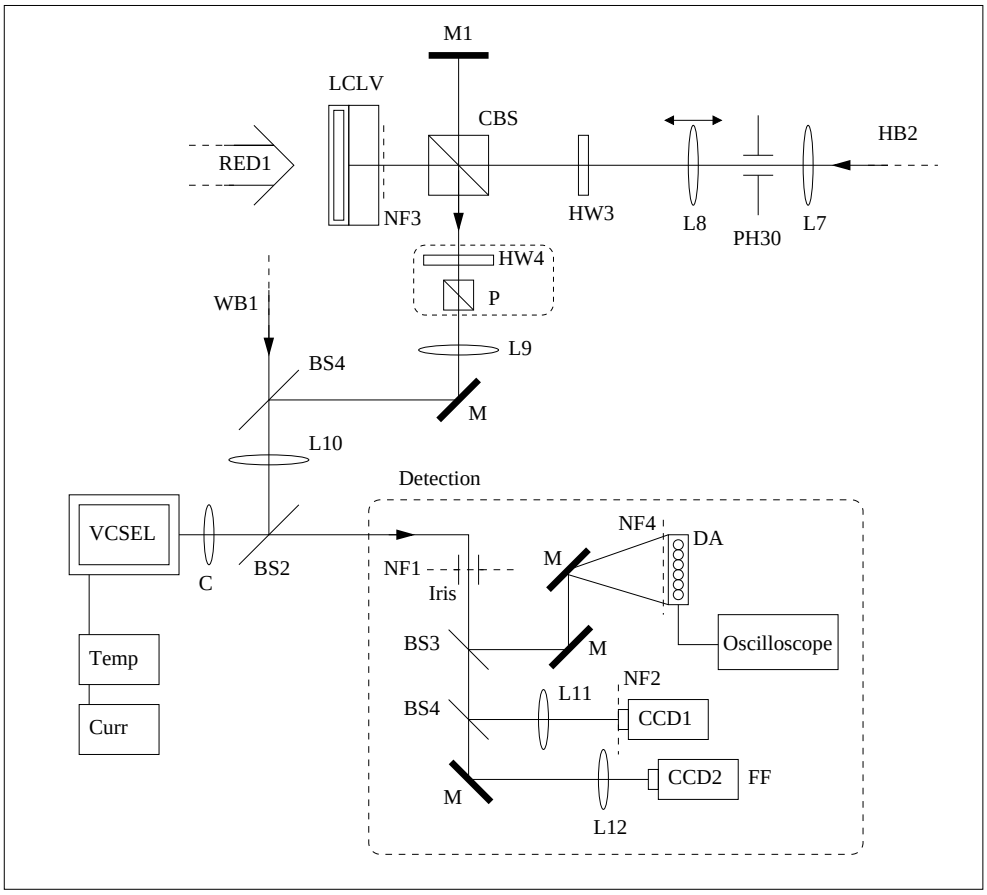

Figure III.28.: Experimental setup modified from fig.III.6 by the insertion of the LCLV.

respect to the table plane after the Fourier filter) is controlled by the half wave plate HW3. The polarizer P at the output of the LCLV is oriented at $+45^o$ with respect to the vertical. Fixing the angles of the two half wave-plate HW3 and HW4 is then possible to produce phase or intensity modulations separately.

A pure phase modulation is produced injecting on the LCLV the beam with vertical polarization (parallel to $\widehat{n}$), as discussed in sec.III.5.1.1. In this case the output polarization from the LCLV remains vertical and is turned by the half wave-plate HW4 (fixed at $+22.5^o$) in oder to match the angle of the output polarizer P. An amplitude modulation is generated by the injection on the LCLV of the beam with polarization turned (by HW3) at -45^o. The output polarization state then depends on the effective voltage across the the valve, as in fig.III.25. Then the half wave-plate HW4 is turned parallel to the output polarizer P, which converts the phase in amplitude modulations.

The positions of the lens L9 and L10, together with the collimator C, are chosen in

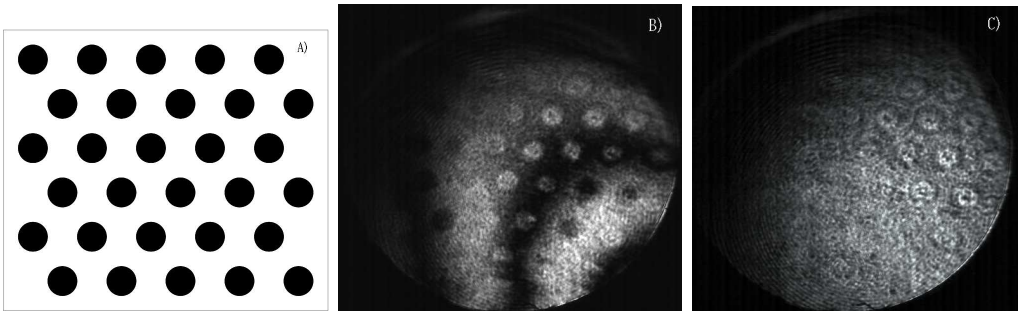

Figure III.29.: *A)* computer created image, sent to the rear side of the LCLV. *B)* phase modulation made visible by interference on the plane of the VCSEL. *C)* residual (normalized) amplitude modulation, found by background substraction. This can be eliminated by reducing the high frequency components of the image sent to the LCD and arriving to the LCLV.

order to form the image of the plane of the valve over the VCSEL. The magnification of this imaging system is of the order of 0.04, so we can use a region of 0.5 cm on the valve to cover the VCSEL diameter of 200 μm. Equivalently, the near field image of the VCSEL (NF3) is formed on the plane of the valve. Other near field images are found as before in the detection system (see Detection in sec.III.2), NF4 in the plane of the array of detectors DA, NF2 on the CCD camera and NF1 in the plane of the iris. The insertion of the writing beam can be done trough the beam splitter BS4.

In this configuration the phase profile of the holding beam injected in the VCSEL is very close to that arriving on the valve, because of the imaging system between them. We need, before creating any modulation, that the field arriving on to the VCSEL could be well approximated by a plane wave. This means that the amplitude and phase profile should be the as flat as possible in order to better control and understand the effect of a modulation. Then as a compromise between power and profile flatness, the amplitude waist of the beam arriving on the VCSEL is chosen of the same order of the laser diameter. In terms of gaussian beams, in order to have a flat phase profile on the VCSEL we would have to fix the position of the waist of the beam on the plane of the valve. This would be transfered without diffraction to the VCSEL surface by the imaging system. However the waist should have transverse dimension of about half a centimeter on the valve, and we have found difficult to locate a waist so large exactly along the axis. Therefore we use as an alternative method for having confidence that the phase profile is flat, the minimization of the far field size of the beam reflected on the VCSEL, placing lens L8 at almost its focal length from the pin hole PH30. In these conditions the transverse wavevectors of the injected field should be minimized on the valve and on the VCSEL plane.

In the measurements described in the following, we were mainly interested in modulating the phase of the holding beam more than its amplitude. This is because the latter is a control parameter for the solutions of the system, so it may change their stability or even change the solutions themselves. The phase on the contrary should not change the nature of the solutions of the system, in principle producing only a drift of the existent solutions which are controlled by other parameters. It is then interesting to see if the control of localized structures with fixed parameters along the transverse plane is possible with the phase alone.

The empty arm of the interferometer (CBS-M1) is then opened to visualize on the VCSEL the phase modulations, otherwise not visible, created by the valve as a shift of the interference fringes, and during the experiment will be always closed. A typical example of the phase modulation created by the LCLV, visualized by the use of the interferometer is shown in fig.III.29.b . This is the image of the VCSEL plane NF2 on camera CCD1, with no current injection in the laser (so the VCSEL acts simply as a mirror) and modulated phase of the holding beam. The image sent from the computer, shown in fig.III.29.a , is an hexagonal matrix of black circles on a white background. The phase modulation, given by the modulation of the index of the liquid crystal, is then visible as an amplitude modulation by the interference of the two arm of the interferometer.

Experimentally we have found quite difficult to produce pure phase modulations of the holding beam. With the profile of fig.III.29.a applied to the LCLV, we obtain the spurious intensity modulation shown in fig.III.29.c, which has (once it is averaged on a cavity soliton size) an amplitude of 15% of the mean injected value. The origin of this effect is not clear, but it seems related to the presence of high spatial frequencies in the image sent to the LCLV. In fact when we use a high contrasted image (like the one in fig.III.29.a) with high frequencies components (steep gradients from white to black), the corresponding regions become visible as an amplitude modulation. Indeed the visible intensity modulation consists in black rings corresponding to the borders of each circle of the image sent by the computer. However we have indications that the small intensity modulation plays a minor role in pinning the localized structures, as it is discussed in the next section.

III.5.2. Results

As a first result we show in fig.III.30 the spatial arrangement of the localized structures with the injection shown in fig.III.29. We fix the current of the VCSEL at 560 mA, the total injected power is around 15 mW and the modulation on the LCLV consists in a hexagonal matrix of highly contrasted circles. Then the phase step between the background and the flat top of each circle of the injected image is about 0.8π rad.

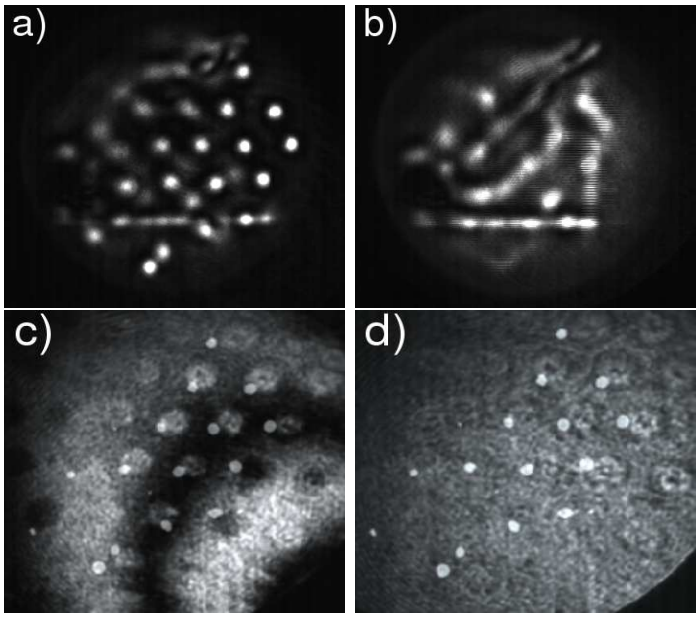

Figure III.30.: *a)* VCSEL electrically driven at 560 mA, under modulated holding beam injection. The hexagonal phase and amplitude modulations are shown in fig.III.29. *b)* same as before but the modulation in the holding beam is removed. *c)* The positions of the pinned structures (with modulation in the holding beam) are superimposed to the injected phase modulation and *d)* to the amplitude modulation (see fig.III.29).

Together with it, a small amplitude modulation is present at the edges of each circle, as discussed above. Every black circle of the injected profile defines a small circular region where a localized structure could be confined by the strong phase gradient present at the border. It results that the spatial organization of the structures in the near field (fig.III.30.a) well follows the injected profile, as they are pinned at the positions defined by the external hexagonal modulation when it is present. When the modulation is removed, just blocking the rear side of the LCLV from the RED1 beam (fig.III.30.b), a complicated dynamical state is found where the hexagonal organization is absent. This demonstrates that the imposed modulation of the holding beam is necessary for the spatial distribution of the localized structures.

In fig.III.30.c and .d we show the relative positions of the structures over the corresponding phase (.c) and residual amplitude (.d) modulation (of fig.III.29). It results that the position of each localized structure is pinned laterally with respect to the center of each black circle forming the injected modulation image. More importantly, these stable positions correspond to local minima of the spurious intensity modulation, as shown in fig.III.30.d . This indicates that the phase gradient is the responsible

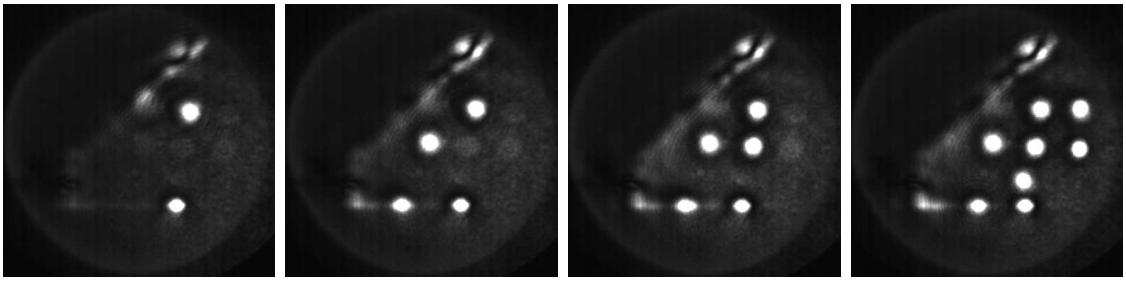

Figure III.31.: Near field of the injected VCSEL for increasing current (from left to right: 557, 563, 565, 567 mA) with a square grid phase (and spurious amplitude) profile of the holding beam.

for the pinning, because the intensity gradient tends to destabilize the structures at their positions. Their positions, blocked along the edges of the circles with a similar orientation, could be explained by the presence of a residual gradient along a direction close to 45^o in the images, due to a light misalignment of the holding beam or to a small long-scale variation of the cavity length along the device. This residual gradient would "push" the structures inside the circular confining region of phase (where they are in principle free to move) until they are blocked by the effect of the border, where the phase gradient is maximum.

Solitons can spontaneously arrange their positions, in absence of any external modulation, in order to form hexagonal arrays [98] [99]. So we have to show that the configuration chosen in fig.III.30 is not special and that solitons can follow a different modulation. This is done in fig.III.31 where the imposed modulation is a square array of contrasted circles of the same size of fig.III.30. Here we increase the pumping current of the VCSEL from 557 mA (left) to 567 mA (right). This induces the formation of localized structures at the position of the phase maxima. The intensity modulation visible here is mostly a result of (eventually non linear) amplification of the injected beam in the VCSEL cavity. Finally, we notice that while each structure switches on in a subcritical way (i.e. there is a bias current region for which each structure is bistable), the structures could not be made all bistable for the same current value, and this was true also for the result of fig.III.30. This phenomenon can be attributed again to residual long range inhomogeneities, mainly in the local resonance frequency of the VCSEL structure [100][101].

In order to further verify the possibility to control the positions of the solitons by the phase of the holding beam alone, we reduce the remaining intensity modulations using a smoothed image sent to the LCD, where high spatial frequencies are absent. In the set of measurements shown in fig.III.32 we have found that a smoother profile

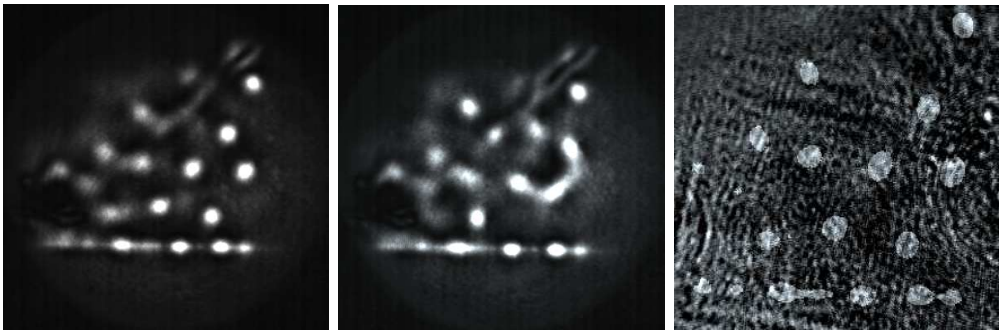

Figure III.32.: *Left:* Near field of the injected VCSEL with holding beam phase-modulated by an almost sinusoidal hexagonal spatial profile. *Center:* same as before but the phase modulation is blocked. *Right:* difference between the modulated and non-modulated holding beam. The positions of the pinned structures is marked with bright spots. The visible remaining amplitude modulation of the holding beam is small compared to the spatial noise of the injection.

on the LCLV has the effect to reduce the intensity variations of the holding beam at the plane of the VCSEL, which are present in correspondence of steep variations of the index of the valve. In this way we obtain a spurious intensity modulation completely negligible at the soliton scale (see fig.III.32(right)). Therefore we can be confident that in these measurements the phase modulation (whose amplitude remains as before of the order of 0.8 π) is more effective than the amplitude over the positions of the structures. On the other hand the phase gradient is reduced by the use of such smoother modulation.

However, the spatial organization of the localized structures, shown in fig.III.32 (left), well follows the imposed hexagonal phase modulation. When the modulation is blocked (center), the same arrangement is not preserved. At right the remaining amplitude modulation is shown together with the position of the structures. This small amplitude modulation is completely hidden by the noise in the spatial profile, it does not have a clear hexagonal profile and should not be able to pin the solitons. This fact builds confidence that phase modulations alone can stabilize the localized structures in predefined positions of the transverse plane.

III.6. Conclusions

This part of the thesis is devoted to spatial localized structures, which are found in the transverse plane of injected semiconductor VCSELs. Thanks to the improvement of the growth processes (by Ulm Photonics), we can now take advantage of more homogeneous devices, where long scale spurious cavity gradient, main limiting factor in the past, are greatly reduced. In these new devices we could demonstrate some important features of cavity solitons, related to the effects of external perturbations over the system.

Firstly, we could elucidate the role of small-scale imperfections in the cavity. Due to the random distribution of impurities on the plane of the VCSEL, the probability to host a soliton is not evenly distributed on the transverse plane of the laser. Attracting defects are defined by the stable positions spontaneously chosen by solitons when phase and intensity gradients are absent. Using the combined action of intensity and phase gradients, we could demonstrate that the effect of these impurities can be overcome, and a soliton can be moved from its original position defined by an imperfection. This shows that the presence of defects, even if somehow useful in order to observe stable structures in presence of spurious gradients, is not strictly necessary for the existence of cavity solitons.

Analyzing the equilibrium positions of solitons in presence of intensity and phase gradients, we have shown that it is possible to interpret the observations in terms of the predictions of the theory, but taking into account the effect of defects is also necessary. In fact the most probable interpretation is that solitons drift along the phase and intensity gradients, accordingly to theory, but a third force due to attracting defects is needed to explain in detail their behavior when the controlled gradients are changed. Using the interplay between the effect of externally controlled gradients and that of internal defects over the stable positions of solitons, we have then proposed a method that, within some limitations for our systems, allows to visualize the cavity imperfections of the device.

We have then focused the attention on the motion of localized structures in the transverse plane. In order to make easier the detection of moving structures, we have confined them along linear intensity channels formed by interference fringes on the VCSEL plane. We have strong indications that motion of localized structures inside the intensity fringe occurs, and that an optical shift register based on localized structures is in principle feasible, increasing the interest of this system for real applications. We have also described and characterized the phenomenology experimentally found around the region of parameters where motion is observed. The observed displacement of a localized structure over many tens of μm indicates again that imperfections only have a stabilizing role, and are not required for cavity solitons to exist.

We have on the contrary weak indications about the dependence of the speed of the structures with the external gradients. In order to better connect the experimental observations with the theoretical predictions, and also from the point of view of possible applications, it will be important in the future to better quantify how the magnitude of the velocity of the drifting structures depends on the strength of the applied gradients. This could be done, with a fine control of the double holding beam injection (that was not possible at present), relating the information about the phase gradient along the intensity fringes, extracted from the far field, with the measured speed.

Finally we made efforts in building an experimental system that could provide a separate control of the phase and intensity of the injection. In this way we could generate an arbitrary profile for the injected phase, with a small spurious amplitude component that however can be reduced giving similar results. Applying this spatial modulation to the injection beam, we could fix the positions of many solitons in different configurations (hexagonal and square). This demonstrates in principle the pinning effect of a transverse parametric modulation (mainly phase) in semiconductors, as predicted by the theoretical results.

All these experimental results encourage further research on the properties of cavity solitons in VCSELs, showing that applications, that ultimately need their positioning or drifting, are in principle possible. As now the long-scale defects have been eliminated from the semiconductors growth process, the main limiting factors seem to be the small-scale imperfections of the cavity that narrow the effective transverse plane hosting solitons. In order to experimentally overcome the effects of imperfections it could be useful in the future to develop the spatial modulator in order to achieve higher phase variations. Hopefully this system will make possible to better control the applied gradients and to better understand the properties of the system.

Bibliography

[1] A.Einstein. Zur quantentheorie der strahlung. *Physik.Zeitschr.*, 18:121–128, 1917.

[2] J. P. Gordon, H. J. Zeiger, and C. H. Townes. Molecular microwave oscillator and new hyperfine structure in the microwave spectrum of NH_3. *Phys. Rev.*, 95(1):282–284, Jul 1954.

[3] T.H.Maiman. Stimulated optical radiation in ruby. *Nature*, 187:493–494, 1960.

[4] A. Javan, W. R. Bennett, and D. R. Herriott. Population inversion and continuous optical maser oscillation in a gas discharge containing a He-Ne mixture. *Phys. Rev. Lett.*, 6(3):106–110, Feb 1961.

[5] 'They would say, 'You don't know how many lives you've saved."- Dr. Robert Wiseman, former head of Night Vision Laboratories, http://www.nvl.army.mil/about/index.php .

[6] Guy Van der Sande. *Simple models for complex photonic structures*. PhD thesis, Brussel, Vrije Universiteit, May 2005.

[7] Jr. Holonyak, N. The semiconductor laser: a thirty-five-year perspective. *Proceedings of the IEEE*, 85(11):1678–1693, Nov 1997.

[8] R. Dupuis. An introduction to the development of the semiconductor laser. *Quantum Electronics, IEEE Journal of*, 23(6):651– 657, Jun 1987.

[9] Many informations about laser origins can be found in: http://en.wikipedia.org/wiki/Laser and http://www.ieee.org/organizations/-pubs/newsletters/leos/feb03/diode.html.

[10] See the reproduction of his unpublished 1953 paper in J. von Neumann, IEEE J. Quant. Electron. QE-23, 659 (1987).

[11] M.G.A.Bernard and G.Douraffourg. Laser conditions in semiconductors. *Phys.Status Solidi*, (1):669–703, 1961.

[12] D. N. Nasledov, A. A. Rogachev, S. M. Rivkin, and B. V. Tsarenkov. *Sov. Phys. Sol. State.*, (4):782, 1962.

[13] from www.star.le.ac.uk.

[14] W.Chow, S.Koch, and M.Sargent. *Semiconductor-Laser Physics*. Springer, 1997.

[15] R. N. Hall, G. E. Fenner, J. D. Kingsley, T. J. Soltys, and R. O. Carlson. Coherent light emission from GaAs junctions. *Phys. Rev. Lett.*, 9(9):366–368, Nov 1962.

[16] H. Kroemer. A proposed class of heterojunction injection lasers. *Proc.IEEE*, (51):1782–1783, 1963.

[17] Hayashi I., Panish M., and Foy P. A low threshold room-temperature injection laser. *IEEE J.Q.Elec.*, (5):211–212, 1969.

[18] F.T.Arecchi. *Instabilities and chaos in single mode homogeneous line lasers, in Instabilities and chaos in quantum optics*, volume 34. Springer Series Synergetics, 1987.

[19] J. R. Tredicce, F. T. Arecchi, G. P. Puccioni, A. Poggi, and W. Gadomski. Dynamic behavior and onset of low-dimensional chaos in a modulated homogeneously broadened single-mode laser: Experiments and theory. *Phys. Rev. A*, 34(3):2073–2081, Sep 1986.

[20] F.T.Arecchi, R.Meucci, G.P.Puccioni, and J.R.Tredicce. Deterministic chaos in lasers with injection signal. *Opt.Comm.*, 51:308–314, 1984.

[21] J.R.Tredicce, F.T.Arecchi, G.L.Lippi, and G.P.Puccioni. Instabilities in lasers with an injected signal. *J.Opt.Soc.Am.B*, 2(1):173, Jan. 1985.

[22] H. Haken. Analogy between higher instabilities in fluids and lasers. *Phys.Lett.*, 53A:77, 1975.

[23] M.Ohtsu, Y.Teramachi, Y.Otsuka, and A.Osaki. Analyses of mode-hopping phenomena in an AlGaAs laser. *IEEE J.Quantum Electronics*, 22:535, 1986.

[24] G. R. Gray and R. Roy. Bistability and mode hopping in a semiconductor laser. *J. Opt. Soc. Am. B*, (8):632, 1991.

[25] Luca Gammaitoni, Peter Hänggi, Peter Jung, and Fabio Marchesoni. Stochastic resonance. *Rev. Mod. Phys.*, 70(1):223–287, Jan 1998.

[26] Bob Nagler, Michael Peeters, Jan Albert, Guy Verschaffelt, Krassimir Panajotov, Hugo Thienpont, Irina Veretennicoff, Jan Danckaert, Sylvain Barbay, Giovanni Giacomelli, and Francesco Marin. Polarization-mode hopping in single-mode vertical-cavity surface-emitting lasers: Theory and experiment. *Physical Review A*, 68(1):013813, 2003.

[27] Michael Peeters. *Polarization switching in Vertical Cavity Surface-Emitting Lasers*. PhD thesis, Vrije Universiteit, Brussel, April 2003.

[28] M. P. van Exter, M. B. Willemsen, and J. P. Woerdman. Polarization fluctuations in vertical-cavity semiconductor lasers. *Phys. Rev. A*, 58(5):4191–4205, Nov 1998.

[29] J. Talghader and J. S. Smith. Thermal dependence of the refractive index of GaAs and AlAs measured using semiconductor multilayer optical cavities. *Applied Physics Letters*, 66(3):335–337, January 1995.

[30] K.Petermann. *Laser Diode Modulation and Noise*. ADOP-Kluwer Academic, Dordrecht, 1988.

[31] G.Hasnhain, K.Thai, L.Yang, Y.H.Wang, R.J.Fisher, J.Wynn, B.Weir, N.K.Dutta, and A.Y.Cho. Performance of gain-guided surface emitting lasers with semiconductor distributed bragg reflectors. *IEEE Journal of Quantum Electronics*, 27(6):1377–1385, 1991.

[32] Giovanni Giacomelli, Francesco Marin, and Ivan Rabbiosi. Stochastic and bona fide resonance: An experimental investigation. *Phys. Rev. Lett.*, 82(4):675–678, Jan 1999.

[33] S.Arrenious. *Z.Phys.Chem.*, 4:226, 1889.

[34] J. van't Hoff. Etude de dynamique chimiques. *Muller, Amsterdam*, 1884.

[35] C.W.Gardiner. *Handbook of stochastic methods, 2nd ed.* 1985.

[36] N.C.Wax. *Selected papers on noise and stochastic processes*. Dover, New York, 1954.

[37] R. Toral M.San Miguel. Stochastic effects in physical systems. *Departamento de Fisica Interdisciplinar, IMEDEA*, http://www.imedea.uib.es/PhysDept/.

[38] H.Kramers. *Physica (Utrecht)*, 7:284, 1940.

[39] M.Borkovec P.Hanggi, P.Talkner. Reaction-rate theory: fifty years after kramers. *Rev.Mod.Phys.*, 62:251, 1990.

[40] M. R. Young and Surendra Singh. Effects of multiplicative white noise on laser light fluctuations. *Phys. Rev. A*, 38(1):238–244, Jul 1988.

[41] J. M. Sancho, M. San Miguel, S. L. Katz, and J. D. Gunton. Analytical and numerical studies of multiplicative noise. *Phys. Rev. A*, 26(3):1589–1609, Sep 1982.

[42] C. Van den Broeck, J. M. R. Parrondo, R. Toral, and R. Kawai. Nonequilibrium phase transitions induced by multiplicative noise. *Phys. Rev. E*, 55(4):4084–4094, Apr 1997.

[43] R.Benzi, A.Sutera, and A.Vulpiani. *J.Phys.A*, 14:453, 1981.

[44] Bruce J. Gluckman, Theoden I. Netoff, Emily J. Neel, William L. Ditto, Mark L. Spano, and Steven J. Schiff. Stochastic resonance in a neuronal network from mammalian brain. *Phys. Rev. Lett.*, 77(19):4098–4101, Nov 1996.

[45] Enrico Simonotto, Massimo Riani, Charles Seife, Mark Roberts, Jennifer Twitty, and Frank Moss. Visual perception of stochastic resonance. *Phys. Rev. Lett.*, 78(6):1186–1189, Feb 1997.

[46] G.P. Harmer, B.R. Davis, and D. Abbott. A review of stochastic resonance: circuits and measurement. *Instrumentation and Measurement, IEEE Transactions on*, 51(2):299–309, April 2002.

[47] Bruce McNamara, Kurt Wiesenfeld, and Rajarshi Roy. Observation of stochastic resonance in a ring laser. *Phys. Rev. Lett.*, 60(25):2626–2629, Jun 1988.

[48] Rajarshi Roy, R. Short, J. Durnin, and L. Mandel. First-passage-time distributions under the influence of quantum fluctuations in a laser. *Phys. Rev. Lett.*, 45(18):1486–1490, Nov 1980.

[49] Sylvain Barbay, Giovanni Giacomelli, and Francesco Marin. Stochastic resonance in vertical cavity surface emitting lasers. *Phys. Rev. E*, 61(1):157–166, Jan 2000.

[50] Francesco Marino, Massimo Giudici, Stéphane Barland, and Salvador Balle. Experimental evidence of stochastic resonance in an excitable optical system. *Phys. Rev. Lett.*, 88(4):040601, Jan 2002.

[51] Sylvain Barbay, Giovanni Giacomelli, and Francesco Marin. Experimental evidence of binary aperiodic stochastic resonance. *Phys. Rev. Lett.*, 85(22):4652–4655, Nov 2000.

[52] L. Gammaitoni, F. Marchesoni, and S. Santucci. Stochastic resonance as a bona fide resonance. *Phys. Rev. Lett.*, 74(7):1052–1055, Feb 1995.

[53] Zaikin A., Kurths J., and L. Schimansky-Geier. Doubly stochastic resonance. *Phys. Rev. Lett.*, 85(2):227–231, Jul 2000.

[54] A. Zaikin, J. Garca-Ojalvo, R. Bscones, E. Ullner, and J. Kurths. Doubly stochastic coherence via noise-induced symmetry in bistable neural models. *Phys. Rev. Lett.*, 90(3):030601, 2003.

[55] M.Sargent, M.O.Scully, and W.E.Lamb. *Laser Physics*. Addison-Welsey Publ. Comp., 1974.

[56] C.H.Henry. Theory of linewidth of semiconductor laser. *IEEE J.Quantum Electronics*, QE-18:259–264, 1982.

[57] J.Danckaert, B.Nagler, J.Albert, K.Panajotov, Veretennicoff I, and T.Erneux. Minimal rate equations describing polarization switching in vcsels. *Optics Communications*, (201):129–137, 2002.

[58] M. San Miguel, Q. Feng, and J. V. Moloney. Light-polarization dynamics in surface-emitting semiconductor lasers. *Phys. Rev. A*, 52(2):1728–1739, Aug 1995.

[59] Stephane Barland. *Etude expérimentale de microcavités à semiconducteur: Structures spatiales étendues et localisées*. PhD thesis, Université de Nice Sophia Antipolis, Institut Non Linéaire de Nice, december 2001.

[60] Barland S., Tredicce J.R., Brambilla M., Lugiato L.A., Balle S., Giudici M., Maggipinto T., Spinelli L., Tissoni G., Knodl T., Miller M., and Jager R. Cavity solitons as pixels in semiconductor microcavities. *Nature*, 419(6908):699–702, Oct. 2002.

[61] Xavier Hachair. *Les solitons de cavité: Etude expérimentale*. PhD thesis, Université de Nice Sophia Antipolis, Institut Non Linéaire de Nice, december 2003.

[62] X. Hachair, L. Furfaro, J. Javaloyes, M. Giudici, S. Balle, J. Tredicce, G. Tissoni, L. A. Lugiato, M. Brambilla, and T. Maggipinto. Cavity-solitons switching in semiconductor microcavities. *Physical Review A (Atomic, Molecular, and Optical Physics)*, 72(1):013815, 2005.

[63] A. M. Turing. *Philos. Trans. R. Soc. London*, (37):237, 1952.

[64] Lord Rayleigh. *Phil. Mag.*, (32):592, 1916.

[65] M. C. Cross and P. C. Hohenberg. Pattern formation outside of equilibrium. *Rev. Mod. Phys.*, 65(3):851, Jul 1993.

[66] F.T.Arecchi, S.Boccaletti, and P.L.Ramazza. Pattern fomation and competion in nonlinear optics. *Physics Report*, (318):1–83, 1999.

[67] T.Ackemann and W.J.Firth. Dissipative solitons in pattern-forming nonlinear optical systems: cavity solitons and feedback solitons. *Lect. Notes Phys.*, (661):55–100, 2004.

[68] D. W. Mc Laughlin, J. V. Moloney, and A. C. Newell. Solitary waves as fixed points of infinite-dimensional maps in an optical bistable ring cavity. *Phys. Rev. Lett.*, 51(2):75–78, Jul 1983.

[69] N. N. Rosanov and G. V. Khodova. Autosolitons in bistable interferometers. *Opt. Spectrosc.*, (65):449, 1988.

[70] M. Brambilla, L. Lugiato, and M. Stefani. Injection and control of localized structures. *Europhys. Lett.*, 34:109–114, 1996.

[71] M. Saffman, D. Montgomery, and D. Z. Anderson. *Opt. Lett.*, (19):518, 1994.

[72] C. O. Weiss, M. Vaupel, K. Staliunas, G. Slekys, and V. B: Taranenko. *Appl. Phys. B*, (68):152, 1999.

[73] S. Residori, A. Petrossian, T. Nagaya, and M. Clerc. Review article.Localized structures and their dynamics in a liquid crystal light valve with optical feedback. *Journal Of Optics B: Quantum and semiclassical optics*, (6):169–176, 2004.

[74] U. Bortolozzo and S. Residori. Storage of localized structure matrices in nematic liquid crystal. *Phys.Rev.Lett.*, (96):037801, 2006.

[75] B. Schapers, T. Ackemann, and W. Lange. Characteristics and possible applications of localized structures in an optical pattern-forming system. *Proc. SPIE*, (4271):130–137, 2001.

[76] L. Spinelli, G. Tissoni, M. Brambilla, F. Prati, and L. A. Lugiato. Spatial solitons in semiconductor microcavities. *Phys. Rev. A*, 58(3):2542–2559, Sep 1998.

[77] L.A.Lugiato. Introduction to the feature section on cavity solitons: an overview. *IEEE Journal of Quantum Elec.*, 39(2), Feb. 2003.

[78] Nikolay N. Rosanov, Sergey V. Fedorov, and Anatoly N. Shatsev. Curvilinear motion of multivortex laser-soliton complexes with strong and weak coupling. *Phys. Rev. Lett.*, 95(5):053903, Jul 2005.

[79] W. Firth and I. Galbraith. Diffusive transverse coupling of bistable elements–switching waves and crosstalk. *IEEE journal of Quantum Electronics*, 21(9):1399– 1403, Sep 1985.

[80] M. Tlidi, Paul Mandel, and R. Lefever. Localized structures and localized patterns in optical bistability. *Phys. Rev. Lett.*, 73(5):640–643, Aug 1994.

[81] L.Lugiato, L.Spinelli, G.Tissoni, and M.Brambilla. Modulational instability and cavity solitons in semiconductors microcavities. *J.Opt.B: Quantum Semiclassical Opt.*, (1):43–51, 1999.

[82] S. Fauve and O. Thual. Solitary waves generated by subcritical instabilities in dissipative systems. *Phys. Rev. Lett.*, 64(3):282–284, Jan 1990.

[83] O. Thual and S. Fauve. Localized structures generated by subcritical instabilities. *J.Physique*, 1(49):1829, 1988.

[84] P. Coullet, C. Riera, and C. Tresser. Stable static localized structures in one dimension. *Phys. Rev. Lett.*, 84(14):3069–3072, Apr 2000.

[85] J.M.McSloy, W.J.Firth, G.L.Oppo, and G.K.Harkness. Computationally determined existence and stability of transverse structures: Ii multi-peaked cavity solitons. *PRE*, (66):046606, 2002.

[86] S.Fedorov, D.Michaelis, U.Peshel, C.Etrich D.Skryabin, N.Rosanov, and F.Lederer. Effects of spatial inhomogeneities on the dynamics of cavity solitons in quadratically nonlinear media. *PRE*, (64):036610, 2001.

[87] W. J. Firth and A. J. Scroggie. Optical bullet holes: Robust controllable localized states of a nonlinear cavity. *Phys. Rev. Lett.*, 76(10):1623–1626, Mar 1996.

[88] L. A. Lugiato and R. Lefever. Spatial dissipative structures in passive optical systems. *Phys. Rev. Lett.*, 58(21):2209–2211, May 1987.

[89] T. Maggiopinto, M. Brambilla, G. K. Harkness, and W. J. Firth. Cavity solitons in semiconductor microresonators: existence, stability and dynamical properties. *PRE*, 62(6):8726, 2000.

[90] A. J. Scroggie, J. Jeffers, G. McCartney, and G. L. Oppo. Reversible soliton motion. *PRE*, (71):046602, 2005.

[91] L.Spinelli, G.Tissoni, L.Lugiato, and M.Brambilla. Thermal effects and transverse structures in semiconductor microcavities with population inversion. *Phys.Rev.A*, 66:023817–12, 2002.

[92] A. J. Scroggie, J. M. McSloy, and W. J. Firth. Self-propelled cavity solitons in semiconductor microcavities. *PRE*, (66):036607, 2002.

[93] from www.wikipedia.org, under GNU license.

[94] G.Tissoni, L.Spinelli, M.Brambilla, T.Maggipinto, I.M.Perrini, and L.Lugiato. Cavity solitons in passive bulk semiconductor microcavities. ii. dynamical properties and control. *J. Opt. Soc. Am. B*, 16(11):2095, Nov 1999.

[95] Umberto Bortolozzo. *Control of Optical Structures in a Liquid Crystal Light Valve experiment*. PhD thesis, Université de Nice Sophia Antipolis, Institut Non Linéaire de Nice, Dec 2005.

[96] P.G. de Gennes and J.Prost. *The Physics of Liquid Crystals*. Oxford Science Publications, Clarendon Press, second edition, 1993.

[97] V.Fréedericksz and V.Zolina. *Trans.Faraday Soc.*, 29:919, 1933.

[98] B. Schäpers, M. Feldmann, T. Ackemann, and W. Lange. Interaction of localized structures in an optical pattern-forming system. *Phys. Rev. Lett.*, 85(4):748–751, Jul 2000.

[99] Yu. A. Astrov and Yu. A. Logvin. Formation of clusters of localized states in a gas discharge system via a self-completion scenario. *Phys. Rev. Lett.*, 79(16):2983–2986, Oct 1997.

[100] Xavier Hachair, Stéphane Barland, Luca Furfaro, Massimo Giudici, Salvador Balle, Jorge R. Tredicce, Massimo Brambilla, Tommaso Maggipinto, Ida M. Perrini, Giovanna Tissoni, and Luigi Lugiato. Cavity solitons in broad-area vertical-cavity surface-emitting lasers below threshold. *Phys. Rev. A*, 69(4):043817, Apr 2004.

[101] S. Barland, F. Marino, M. Giudici, and S. Balle. In situ measurement of cavity length variation across the transverse section of broad area vertical cavity surface emitting lasers. *Applied Physics Letters*, (83):2303, 2003.